การสังเคราะห์ปริซึมระดับนาโนเมตรของโลหะเงินด้วยปฏิกิริยาการเปลี่ยนแปลงรูปร่างของ
อนุภาคทรงกลมระดับนาโนเมตรของโลหะเงินโดยการกระตุ้นด้วยไฮโดรเจนเพอร์ออกไซด์

นายเทวารักษ์ ปานกลาง

SILVER NANOPRISM SYNTHESIS BY H_2O_2-TRIGGERED SHAPE TRANSFORMATION OF SILVER NANOSPHERES

Mr. Tewarak Parnklang

A Dissertation Submitted in Partial Fulfillment of the Requirements

for the Degree of Doctor of Philosophy Program in Chemistry

Department of Chemistry

Faculty of Science

Chulalongkorn University

Academic Year 2012

Thesis Title   SILVER NANOPRISM SYNTHESIS BY H_2O_2-TRIGGERED
                    SHAPE TRANSFORMATION OF SILVER NANOSPHERES

By   Mr. Tewarak Parnklang

Field of Study   Chemistry

Thesis Advisor   Associate Professor Sanong Ekgasit, Ph.D.

Thesis Co-advisor   Associate Professor Chuchaat Thammacharoen

---

Accepted by the Faculty of Science, Chulalongkorn University in Partial Fulfillment of the Requirements for the Doctoral Degree

…….…………………………………………Dean of the Faculty of Science

(Professor Supot Hannongbua, Dr. rer. nat.)

THESIS COMMITTEE

………………………………………………Chairman

(Associate Professor Sirirat Kokpol, Ph.D.)

………………………………………………Thesis Advisor

(Associate Professor Sanong Ekgasit, Ph.D.)

………………………………………………Thesis Co-advisor

(Associate Professor Chuchaat Thammacharoen)

………………………………………………Examiner

(Associate Professor Chai Hok Eab, Ph.D.)

………………………………………………External Examiner

(Professor Sukit Limpijumnong, Ph.D.)

………………………………………………External Examiner

(Lecturer Boonsong Sutapun, Ph.D.)

เทวารักษ์ ปานกลาง: การสังเคราะห์ปริซึมระดับนาโนเมตรของโลหะเงินด้วยปฏิกิริยาการ เปลี่ยนแปลงรูปร่างของอนุภาคทรงกลมระดับนาโนเมตรของโลหะเงินโดยการกระตุ้นด้วย ไฮโดรเจนเพอร์ออกไซด์ (SILVER NANOPRISM SYNTHESIS BY H$_2$O$_2$-TRIGGERED SHAPE TRANSFORMATION OF SILVER NANOSPHERES) อ. ที่ปรึกษาวิทยานิพนธ์ หลัก: รศ. ดร. สนอง เอกสิทธิ์, อ. ที่ปรึกษาวิทยานิพนธ์ร่วม: รศ. ชูชาติ ธรรมเจริญ, 118 หน้า.

วิทยานิพนธ์นี้นำเสนอวิธีการแบบใหม่ในการสังเคราะห์คอลลอยด์น้ำของปริซึมระดับ นาโนเมตรของโลหะเงินที่สามารถควบคุมสมบัติโลคัลไลซ์เซอร์เฟซพลาสมอนเรโซแนนซ์ได้ ด้วยวิธีการเปลี่ยนแปลงรูปร่างของอนุภาคทรงกลมระดับนาโนเมตรของโลหะเงินโดยสารละลาย ไฮโดรเจนเพอร์ออกไซด์ กระบวนการเปลี่ยนแปลงรูปร่างสามารถทำได้โดยการฉีดสารละลาย ไฮโดรเจนเพอร์ออกไซด์เข้าไปในคอลลอยด์น้ำของอนุภาคทรงกลมระดับนาโนเมตรของโลหะเงิน ที่มีแป้งเป็นสารช่วยเสถียร การกัดกร่อนผิวผลึกด้วยปฏิกิริยาออกซิเดชันและปฏิกิริยารีดักชันอย่าง อ่อนของไฮโดรเจนเพอร์ออกไซด์ในสภาวะสารละลายที่เป็นด่างเป็นสองปฏิกิริยาเคมีหลักที่ใช้ใน การควบคุมการโตของผลึกในระดับนาโนเมตร ความเข้มข้นเริ่มต้นของอนุภาคทรงกลมระดับนา โนเมตรของโลหะเงิน อัตราส่วนโดยโมลระหว่างไฮโดรเจนเพอร์ออกไซด์และอนุภาคทรงกลม ระดับนาโนเมตรของโลหะเงิน อัตราเร็วในการฉีดสารละลายไฮโดรเจนเพอร์ออกไซด์ และ ประสิทธิภาพของการผสมสาร เป็นตัวแปรการทดลองสำคัญที่ควบคุมค่าความยาวคลื่นคัลไลซ์ เซอร์เฟซพลาสมอนเรโซแนนซ์ในช่วงวิซิเบิลจนถึงเนียร์อินฟราเรด (460-850 นาโนเมตร) ของ ปริซึมระดับนาโนเมตรของโลหะเงินที่สังเคราะห์ได้ ปริซึมระดับนาโนเมตรของโลหะเงินมีรูปร่าง เป็นแบบแผ่นกลมแบน หกเหลี่ยม สามเหลี่ยมยอดตัด หรือ สามเหลี่ยมปลายมน โดยมีความยาว ด้านข้างอยู่ในช่วง 30 ถึง 120 นาโนเมตร และมีความหนาในช่วง 10 ถึง 20 นาโนเมตร ปริซึมระดับ นาโนเมตรของโลหะเงินแสดงสมบัติต่อต้านเชื้อแบคทีเรียหลายชนิดโดยมีค่าความเข้มข้นที่ต่ำที่สุด สำหรับการยับยั้งการเจริญของเชื้ออยู่ที่ 5 ส่วนในล้านส่วน สามารถนำไปประยุกต์ใช้ในการพัฒนา ผ้าปิดแผลปลอดเชื้อประสิทธิภาพสูงที่มีส่วนประกอบหลักเป็นเส้นใยนาโนไบโอเซลลูโลสได้

ภาควิชา.........................เคมี.........................ลายมือชื่อนิสิต...

สาขาวิชา........................เคมี.........................ลายมือชื่ออ. ที่ปรึกษาวิทยานิพนธ์หลัก.................................

ปีการศึกษา.....2555.................ลายมือชื่ออ.ที่ปรึกษาวิทยานิพนธ์ร่วม....................................

4873819623 : MAJOR   CHEMISTRY

KEYWORDS: SILVER NANOPRISMS / SHAPE TRANSFORMATION / HYDROGEN PEROXIDE / LOCALIZED SURFACE PLASMON RESONANCE / WOUND DRESSING / ANTIBACTERIAL ACTIVITIES

TEWARAK PARNKLANG: SILVER NANOPRISM SYNTHESIS BY H_2O_2-TRIGGERED SHAPE TRANSFORMATION OF SILVER NANOSPHERES. ADVISOR: ASSOC. PROF. SANONG EKGASIT, Ph.D., CO-ADVISOR: ASSOC. PROF. CHUCHAAT THAMMACHAROEN. 118 pp.

This dissertation presents a novel approach for synthesizing colloidal silver nanoprisms (AgNPrs) with controllable localized surface plasmon resonance (LSPR) via a chemical shape transformation of silver nanospheres (AgNSs) induced by hydrogen peroxide (H_2O_2). The shape conversion was carried out by feeding H_2O_2 solution into a starch-stabilized AgNSs colloid under an ambient condition. Oxidative dissolution and mild reducing action of H_2O_2 under an alkaline condition serve as principal reactions for the conversion process. Initial concentration of AgNSs, mole ratio of H_2O_2:AgNSs, H_2O_2 feed rate, and mixing efficiency are the key parameters for controlling the LSPR wavelengths of AgNPrs as the in-plane dipole plasmon resonance (IPDPR) can be selectively tuned across visible and near infrared regions (i.e., 460–850 nm). AgNPrs exhibited mixed geometries e.g. hexagonal, truncated triangular, and rounded-tip triangular prisms, and circular disk with the average bisector lengths in the range of 30 to 120 nm and the thickness of 10 to 20 nm. Concentrated AgNPrs with a final concentration up to 11 mM can be produced. "Blue" AgNPrs with edge length in the range of 80–120 nm exhibited the antibacterial activities against various tested bacteria with minimum inhibition concentration (MIC) of 5 ppm. They can also be incorporated in moist wound dressing composed of nanobiocellulose fibers. The efficiency of the developed antiseptic wound dressing was clinically approved for the cavity wounds.

Department……………Chemistry…………Student's Signature…………………………

Field of Study..………Chemistry…………Advisor's Signature…………………………

Academic Year…………2012……………Co-advisor's Signature……………………..

ACKNOWLEDGEMENTS

I would like to express my sincere gratitude to Associate Professor Dr. Sirirat Kokpol, Associate Professor Dr. Chai-Hok Eab, Dr. Boonsong Sutapun, and Professor Dr. Sukit Limpijumnong for the insightful questions and suggestions and contribution as thesis committee.

In essence, the research would never be successfully completed without the excellent advice and pioneering spirit from my thesis advisor and co-advisor, Associate Professor Dr. Sanong Ekgasit and Associate Professor Chuchaat Thammacharoen. I have greatly enjoyed the innovative and challenging atmosphere in his laboratory. His translation of cares into action, guidance, and understanding are deeply thankful.

The extraordinary perseverance of Mr. Adisorn Apasuthirat (Novatec Healthcare Co., Ltd.) and Mr. Sombat Rungsilp (Thainanocellulose, Co., Ltd.) for bridging the gap of fundamental nanotechnology researches and establishing the new milestone in nanomedicine in Thailand are gratefully acknowledged.

Warmest thanks to my friends and colleagues at the Sensor Research Unit (SRU) for the everlasting friendship and technical supports throughout the time of study.

Above all, I am profoundly grateful to my wonderful parents for their patient love, perpetual encouragement, and overwhelming support.

CONTENTS

LIST OF TABLES

LIST OF FIGURES

Figure   Page

Figure   Page

Figure

Page

LIST OF SYMBOLS

$[AgNO_3]$	: molar concentration of $AgNO_3$
$[AgNSs]$	: molar concentration of AgNSs
α_i	: polarizability tensor at point i
a_n	: Mie's coefficient
b_n	: Mie's coefficient
C_{AgNSs}	: concentration of AgNSs in mg/L
$C_{H_2O_2}$	: molar concentration of H_2O_2
C_{Abs}	: absorption cross section
C_{Ext}	: extinction cross section
C_{Scat}	: scattering cross section
Ds	: disperser speed in revolutions (rounds) per minute (rpm)
E	: local electric field
E_o	: amplitude of external electric field
$E_{cell}(Ox)$	: oxidation cell potential
$E_{cell}(Red)$	: reduction cell potential
$F(H_2O_2)$	: flow rate of hydrogen peroxide in mL/min
λ	: incident wavelength
n	: number of moles of electron
N	: the refractive index of medium
N1	: the refractive index of particle
P_i	: induced polarization at point i
Q_{Abs}	: absorption efficiency
Q_{Ext}	: extinction efficiency
Q_{Scat}	: scattering efficiency
R	: molar ratio of H_2O_2:AgNSs or gas constant
r	: radius of spherical particle
V_{AgNSs}	: volume of AgNSs in mL
$V_{H_2O_2}$	: volume of H_2O_2 in mL

ω : electromagnetic wave frequency

ψ_n and ξ_n : Riccati-Bessel functions

$X_{Control}$: amount of bacteria in the control set in CFU/mL

$X_{24\,h}$: amount of bacteria in the test set after 24 hours in CFU/mL

LIST OF ABBREVIATIONS

AgNPrs   : silver nanoprisms

AgNSs   : silver nanospheres

BB   : Brendel-Bormann model for generating optical constant of metal

BEM   : boundary element method

BSPP   : bis(p-sulfonatophenyl) phenylphosphine dihydrate dipotassium salt

CFU   : colony forming units

DDA   : discrete dipole approximation

DMF   : dimethylformamide

DPR   : dipole plasmon resonance

EV   : eigenvalue

EVR   : Ratio of the ith eigenvalue

FDTD   : finite difference time domain

FEM   : finite element method

IPDPR   : in-plane dipole plasmon resonance

LED   : light emitting diode

LSPR   : localized surface plasmon resonance

MCR-ALS   : multivariate curve resolution-alternating least-squares method

MHA   : mercaptohexadecanoic acid

NIR   : near infrared

OPQPR   : out-of-plane quadruple plasmon resonance

P1–P5   : first–fifth pure component

PEG   : poly(ethylene glycol)

PSSS   : poly(sodium styrene sulphonate)

PVA   : poly(vinyl alcohol)

PVP   : poly(vinylpyrrolidone)

rpm   : revolutions or rounds per minute

RPV   : residual percent variance

RSD   : residual standard deviation

RSS   : residual sum of square

SEM   : scanning electron microscopy

SERS   : surface-enhanced Raman scattering

SIMPLSMA   : simple-to-use interactive self-modeling mixture analysis
                  approach

TEM   : transmission electron microscopy

TSC   : trisodium citrate

UV-vis   : ultraviolet-visible

XRD   : X-ray diffraction

CHAPTER I

INTRODUCTION

1.1 Silver Nanoprisms

Silver nanoprisms (also designated as silver nanodisks, silver nanoplates, or flat silver nanocrystals; abbreviated as AgNPrs) have attracted considerable attention due to their extreme degrees of anisotropy, morphologically dependent plasmonic properties, and tailored optical properties from visible to near infrared regions [1–8]. Tremendous local electric field enhancements around AgNPrs when illuminated with appropriate wavelength of electromagnetic wave enable them to be employed as surface-enhanced Raman scattering (SERS) substrates for chemical sensing applications with the enhancement factor up to 10^5–10^8 [9–15]. The high sensitivity toward the variation in local dielectric environment and capability of surface functionalization of AgNPrs permit their use in biological sensing utilizing localized surface plasmon resonance (LSPR) spectroscopy [16–19]. Theoretical simulations based on discrete dipole approximation (DDA) method [20–23] and boundary element method (BEM) [2] provide fundamental understanding on the plasmon oscillation modes of LSPR phenomena and elucidate the influence of shape (e.g. circular disks vs. triangular prisms), aspect ratio (lateral length/thickness), tip sharpness (or degree of truncation), dielectric environment, and elemental composition on plasmonic properties of AgNPrs. The monumental scientific discovery galvanizing many researchers worldwide on morphological-controlled colloidal chemical synthesis of anisotropic plasmonic structures is attributed the work by Mirkin et al [24]. Various techniques for AgNPrs synthesis including photoinduced conversion [3, 24–29], seed mediation [5, 8, 30–35], post modification of preformed AgNPrs [4, 36–39], chiral ligand assisted self-assembling [14], reflux-assisted reduction in dimethylformamide (DMF) [40–41], soft-template method [42–43], thermal process [44–46], polyol method [47–48], and chelation-mediated kinetic controlled synthesis [49], are now well-documented. Solution-based chemical synthesis is flexible, versatile, and robust

for controlling the shape of metallic nanostructures due to facile experimental setup, notably high yield, and feasibility for mass scale production [1, 50]. Controlling the morphology and plasmonic properties of AgNPrs by colloidal chemical synthesis is straightforward provided that the chemical role of each reagent and experimental conditions are comprehensively analyzed.

Recently, a rapid thermochemical synthesis of AgNPrs with high yield at ambient condition employing hydrogen peroxide (H_2O_2) as an oxidative etchant have been reported [8, 14, 34, 51–54]. The idea on employing H_2O_2 for AgNPrs synthesis might be traced back to the work of Métraux in 2005 [51]. The shape transformation reaction was accomplished by direct chemical reduction of silver ion (Ag^+) with sodium borohydride ($NaBH_4$) in the presence of H_2O_2, along with citrate as the capping agent and/or PVP as the polymeric stabilizer. H_2O_2 was utilized as the powerful oxidative etching agent that singled out the seeds with highest stability. The molar concentration of H_2O_2 should be 200 times higher than that of Ag^+ in order to constrain the growth in the oxidative environment. Since H_2O_2 and $NaBH_4$ were simultaneously presented in the growth solution, the molar concentration of $NaBH_4$ should be at least 5 times higher than that of Ag^+ in order to ensure the complete reduction of Ag^+ while $NaBH_4$ was consumed overtime. Etching capability of H_2O_2 was also utilized in seed-mediation approach in the seed preparation step for promoting the formation of planar twinned seeds [8, 34, 54]. Despite the much lower H_2O_2:Ag^+ molar ratio (less than 30) were employed in the procedure, the purification of preformed seeds and a subsequent growth in a solution containing a mild reducing agent, additional Ag^+, and a capping agent were required in order to initiate the nanoprism growth. For both direct chemical reduction and seed mediation approaches, citrate was proven to be an essential part of the synthesis. It strongly coordinated with {111} facet of AgNPrs and facilitated expansion of that facet [55]. Facet specific coordinating capabilities of citrate were also employed for AgNPrs synthesis in many reports [3–5, 8, 24–29, 30–39, 42–43, 45, 49, 51–54]. The total removal of capping ligand in AgNPrs synthesis at room temperature has not been reported, although AgNPrs could be successfully synthesized at elevated temperatures without employing capping molecules [40–41, 44, 46].

1.2 Investigation of Morphological Evolution of Metal Nanoparticles

In order to investigate the particle evolution, scanning electron microscopy (SEM), transmission electron microscopy (TEM), and X-ray diffraction (XRD) techniques are widely employed. However, the fast kinetics and complex particle evolution as well as time-consuming measurements according to sample preparation protocol, the precise and accurate determination of the structural evolution could not be perfectly performed by these imaging techniques under a conventional measurement. Moreover, the morphologies obtained by these methods represent only a partial fraction of particles in the systems. The partial observation may cause the prejudice or misleading of the investigated phenomena due to the bias sample selection. Due to the strong correlation between plasmonic extinction spectra and particle morphologies (especially, in the case of gold and silver nanoparticles) [1–2, 20, 23–24, 91–94], spectroscopic data are more useful to overview the majority of particle structures in the system. One spectral line represents collective information of LSPR from all particles in the colloidal sample. Spectroscopic data can also reveal an *in situ* structural change in samples while SEM or TEM measurements require the sample preparation and show only the *ex situ* information. Sample preparation may cause the structural transformation and the real structure may be misconstrued. However, the obtained spectra might be overlapped and complicated according to the mixing of nanoparticles with several sizes and shapes. The problems can be overcome by utilizing different chemometric methods. Chemometrics, generally known as multivariate statistical analysis, is a powerful technique to analyze complex datasets. These methods provide an alternative way to solve such problems by seeking the number of components and transforming the spectra into profiles which are simple to interpret such as principal components, concentration profiles, and pure spectra profiles [95–96].

Chemometric methods such as Multivariate Curve Resolution-Alternating Least-Squares method (MCR-ALS) [97] can describe reaction process without any prior information using the underlying chemical model and variation to which they are correlated. The concentration profiles of each major component involved in the

reaction and the corresponding pure spectrum can be revealed by using MCR-ALS employed to the obtained spectroscopic data. The obtained concentration profiles can be used to design a suitable reaction, including intermediate species to support the model chosen for a reaction under investigation. The characteristic of major components can be expressed by the obtained pure spectra. This approach has been used in various applications such as biological systems, process monitoring, kinetic investigation etc. [97–99]. There was a few reports on the application of chemometric in nanoscience, e.g. to reveal the growth mechanism of quantum dots (CdSe nanocrystals) [100], to analyse the interaction between nitrogen and nano-titanium dioxide using TEM images [101]. However, there is no report applying chemometrics (MCR-ALS) on the structural evolution of Ag nanostructures.

1.3 Scope of the Research

In the present study, we further explore the potential of H_2O_2 in the shape transformation reaction. The transformation is carried out by injection of H_2O_2 into the preformed starch-stabilized silver nanosphere (AgNSs) colloid under an alkaline condition (pH 8–10). In contrast to the conventional seed mediated approach, separation and purification of the preformed seed solution, and subsequent combination with the growth solution are not required in the proposed procedures. The noticeable feature of our procedures is that the powerful shape selective/facet selective etching of H_2O_2 in combination with its mild reducing capability in alkaline condition are coordinately utilized for anisotropic nanostructure fabrications. The shape transformation process can be initiated and advanced by H_2O_2 without the aid of additional reducing agents or capping molecules for facilitating AgNPrs formation. Although the etching role of H_2O_2 [8, 14, 34, 51–54, 56] and its reducing competency [57–61] for isotropic metal nanostructure fabrication were previously investigated, those functions were harnessed individually. The exploitation both reducing and oxidizing capabilities for anisotropic shape-controlling of noble metal nanostructures have never been reported. Low molar ratio R of H_2O_2:AgNSs (R < 100) is deliberately utilized in order to enhance the coordination of facet selective etching and mild reducing capabilities of H_2O_2 in the construction of AgNPrs while partially

suppress the non-selective solubilization of metallic Ag by H_2O_2. AgNSs play two important roles as the planar twinned seed supplier and internal Ag^+ source. The oxidatively modified AgNSs seeds with planar twinned defects act as the new nucleation sites for the heterogeneous overgrowth. The monomeric Ag atoms are regenerated from the H_2O_2 reduction of oxidatively solubilized Ag^+. We may therefore regard the proposed method as the *in situ* seed-mediated approach. AgNPrs are formed right after the addition of H_2O_2 as can be observed via color change of the colloid. Naked surface of small starch-stabilized AgNSs with high surface area permits H_2O_2 to fully and effectively interact with silver surface. The formation of AgNPrs at high yield could be realized. The highly concentrated AgNPrs (up to 11 mM) with desired in-plane dipole plasmon resonance (IPDPR) wavelengths from visible to near infrared (NIR) spectrum (i.e., 450–850 nm) can be selectively prepared through the optimized experimental parameters. The ability to exclude capping agents from the surface of AgNPrs opens the possibilities for tailoring the surface properties of AgNPrs by subsequent surface modification and functionalization, and makes them suitable for the desired applications. Stabilization of AgNPrs with natural polymer i.e., soluble starch makes AgNPrs suitable for finding opportunities in biological and biomedical applications. The capability to selectively control the LSPR properties of AgNPrs provides unlimited options for selecting appropriate AgNPrs to be employed as colorful antibacterial agents, far-field colorimetric sensors, and near-field surface-enhanced Raman scattering (SERS) substrates.

The growth mechanisms of the chemical shape transformation of AgNSs to AgNPrs were also investigated in details via LSPR spectroscopy and transmission electron microscopy. We also proposed an alternative approach to use MCR-ALS method in processing the overlapping spectroscopic signals in metal nanosynthesis systems. UV-visible extinction spectra of all intermediate structures in the shape evolution process from AgNSs to AgNPrs induced by H_2O_2 were analyzed in order to obtain the mechanism of particle evolution. The morphologies of all determined structures were confirmed by TEM technique, and the shape conversion mechanism based on the calculated results was proposed. The advantages of this MCR-ALS technique in metal nano-synthesis are the more reliably proposed structural evolution,

the reduction of hundreds TEM images to be measured, and the reduction of experimental time and cost.

In order to demonstrate the potential applications of AgNPrs in antiseptic medical devices, the antibacterial activities of "blue" AgNPrs i.e. the AgNPrs with extinction maximum around 800 nm with edge length in the range of 80–120 nm were evaluated. AgNPrs can be incorporated into the moist wound dressing consisted of nanobiocellulose fibers in the post-modification manner. The AgNPrs integrated wound dressing exhibited light blue color representing the sense of cleanness, antisepsis, and safety. The developed antiseptic wound dressing prototype exhibited the high efficiency in wound odor removing, anti-inflammation and accelerated wound recovery.

1.4 Objectives of the Research

1. To develop a novel method for colloidal AgNPrs synthesis utilizing the chemical shape transformation of AgNSs induced by H_2O_2.

2. To elucidate the role of each chemical reagent employed in the shape transformation experiment.

3. To investigate the morphological evolution of AgNSs to AgNPrs and proposed the plausible growth mechanism.

4. To demonstrate the potential applications of AgNPrs in antiseptic medical devices.

CHAPTER II

THEORETICAL BACKGROUND

2.1 Localized Surface Plasmon Resonance (LSPR)

A branch of nanoscience and nanotechnology dealing with the localization, guiding, and manipulation of electromagnetic waves beyond the diffraction limit and down to the nanometer-length scale is regarded as plasmonics [107]. Metal play a key role in plasmonics since it supports surface plasmon polariton modes. Surface plasmon polariton is the coupling of electromagnetic waves and the collective oscillations of free electrons in the metal. Collective oscillation of the gas of negatively charged electrons in the conduction band of the metal as excited by the time-varying electric field is called localized surface plasmon resonance (LSPR). This oscillation will be in resonance with the incident light at a certain excitation frequency (ω), resulting in a strong oscillation of the surface electrons. This phenomenon is illustrated in Figure 2.1. Structures that support LSPR experience a uniform E_o when excited by light as their dimensions are much smaller than the wavelength of the light.
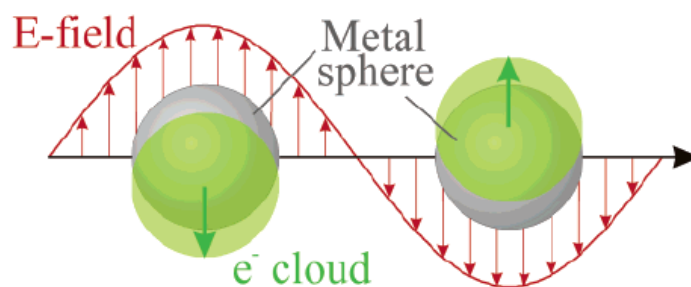
Figure 2.1   Schematic diagram illustrating LSPR phenomena for a sphere. Electron cloud in the conduction band collectively oscillates in coherent with electromagnetic wave. It is displaced relative to the nuclei [20].

In particular, for a spherical nanoparticle in homogeneous medium, its interaction with external electromagnetic wave can be fully described by Maxwell equations. The exact analytical solutions are called "Mie theory". Extinction, absorption, and scattering cross sections (C_{Ext}, C_{Abs}, C_{Scat}, respectively) were calculated using standard Mie's coefficients as follows [3]:

$$C_{Ext} = \frac{2\pi}{k^2} \sum_{n=1}^{\infty} (2n+1) \operatorname{Re}(a_n + b_n) \qquad (2.1)$$

$$C_{Scat} = \frac{2\pi}{k^2} \sum_{n=1}^{\infty} (2n+1) \left(|a_n|^2 + |b_n|^2 \right) \qquad (2.2)$$

$$C_{Abs} = C_{Ext} - C_{Scat} \qquad (2.3)$$

a_n and b_n can be calculated by

$$a_n = \frac{m\psi_n(mx)\psi_n'(x) - \psi_n(x)\psi_n'(mx)}{m\psi_n(mx)\xi_n'(x) - \xi_n(x)\psi_n'(mx)} \qquad (2.4)$$

$$b_n = \frac{\psi_n(mx)\psi_n'(x) - m\psi_n(x)\psi_n'(mx)}{\psi_n(mx)\xi_n'(x) - m\xi_n(x)\psi_n'(mx)} \qquad (2.5)$$

where ψ_n and ξ_n are Riccati-Bessel functions, $m = N_1 / N$, $x = kr = 2\pi Nr / \lambda$, N_1 is the refractive index of particle, N is the refractive index of medium, λ is the incident wavelength, and r is the particle radius. The extinction, absorption, and scattering efficiencies (Q_{Ext}, Q_{Abs}, and Q_{Scat}, respectively) can be calculated by normalizing their corresponding cross sections with particle cross section, πR^2 (e.g. $Q_{Ext} = C_{Ext} / \pi R^2$). In order for calculating the optical property of metal nanoparticles, the dielectric constants of that metal have to be included. Particularly, Brendel-Bormann (BB) model [121] for generating optical constants of metals were employed. In addition, the free path effect of the electron clouds was also included in the calculation as the size-dependent dielectric constant. The simulated size-dependent dielectric constants of gold and silver metals are shown in Figure 2.2.
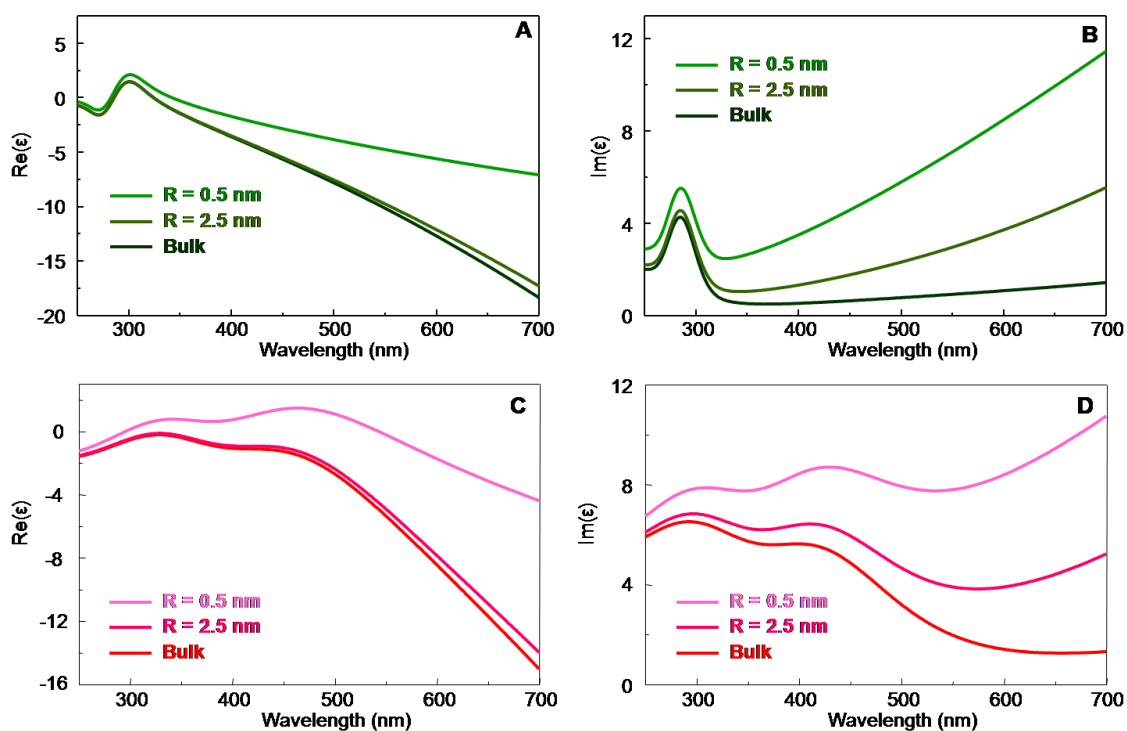
Figure 2.2   Size-dependent dielectric constants of silver (A and B) and gold (C and D) generated from BB model.

Simulated extinction efficiency of spherical silver nanoparticles (AgNSs) dispersed in water (N = 1.333) at various particle sizes is shown in Figure 2.3. The intense peak centered at 400 nm is the dipole plasmon resonance (DPR) of AgNSs (Figure 2.3 A). In addition, when AgNSs were illuminated with electromagnetic waves in the UV region, they also exhibited the extinction band from 200–320 nm. This band is assigned to interband transition of silver metal [91]. The interband transition is inherently associated with metal and is independent of size and shape of nanoparticle. When the particle size increases, the DPR peak of AgNSs redshifts to longer wavelength (Figure 2.3 D). The quadrupole plasmon resonance peak associating with inhomogeneous electron oscillation at 380–400 nm is observed for large particle size (80–100 nm). Optical property of silver spherical nanoparticles is strongly dependent on particle sizes. The measured extinction of silver nanoparticles is directly associated with the genuine particle characteristic dispersed in colloidal suspension.
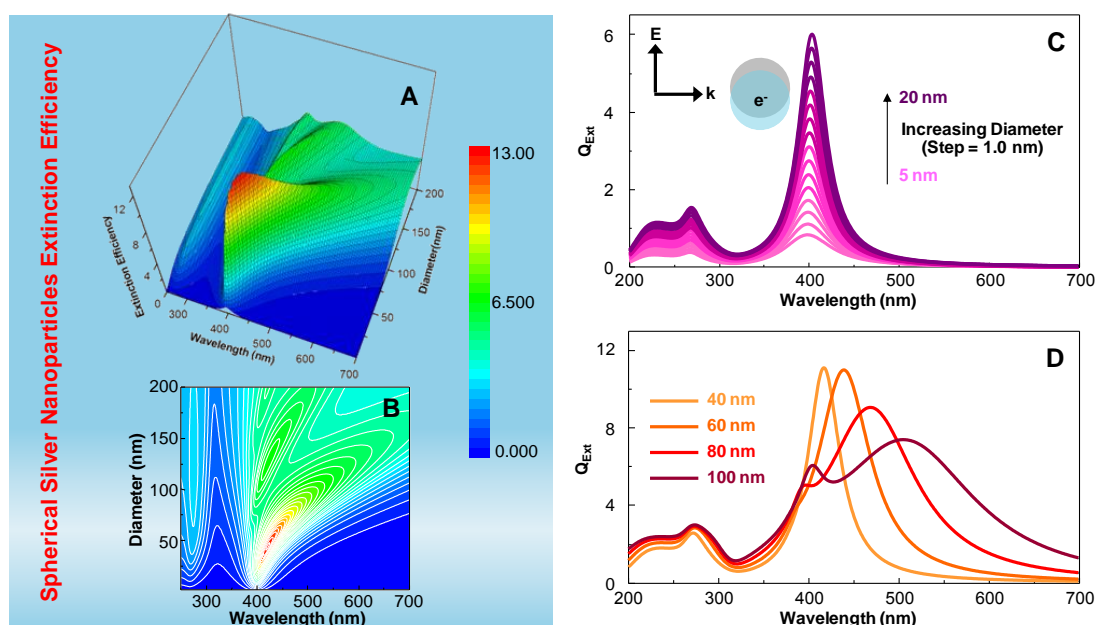
Figure 2.3 Size-dependent extinction efficiency in UV-visible region of a AgNS dispersed in water. Overview of the size-dependent extinction efficiency is shown as 3D color map surface (A) and contour plot (B). The extinction efficiency for particle with diameter from 5–20 nm, and 40–100 nm is shown in C and D, respectively.

We can approximately predict the ensemble-average particle information (e.g., size, shape, and distribution) by measuring extinction spectra by UV-visible spectroscopy. An example of utilizing LSPR in coupled with the real measurement for particle size and shape prediction is shown in Figure 2.4. AgNSs were prepared by reducing aqueous $AgNO_3$ with aqueous $NaBH_4$ with the presence of 2% (w/v) soluble starch. For the case of spherical nanoparticles, the theoretical prediction and real extinction measurement for predicting the particle sizes are in good agreement.

For more complex shapes with lower symmetry, such as triangular nanoprisms or cubes, an exact solution of Maxwell equations cannot be reached. Therefore, numerical methods for determining the plasmonic properties of these shapes have been developed, and notable examples include the discrete dipole approximation (DDA), finite difference time domain (FDTD) method and the finite element method (FEM) [107]. In DDA, the particle is divided into an array of N dipoles with

polarizability. The first step toward calculating the extinction cross section of the nanoparticle is to calculate the induced polarization at each point, P_i, due to an incident plane wave, $P_i = \alpha_i E$, where E is the local electric field defined as the sum of the incident field and the contributions from the surrounding dipoles. Next, the incident field and induced polarizations are used to calculate C_{Ext}. Finally, the equations are solved using full interaction matrices, which take into account the impact of every dipole in the structure. Although DDA yields accurate results with errors < 10% (as determined by comparisons with exact solutions from Mie theory), it is a very slow computational process. However, with recent developments in new algorithms and other methods that dramatically increase the computation speed DDA provides a powerful approach to model both the near- and far-field properties of nanostructures.
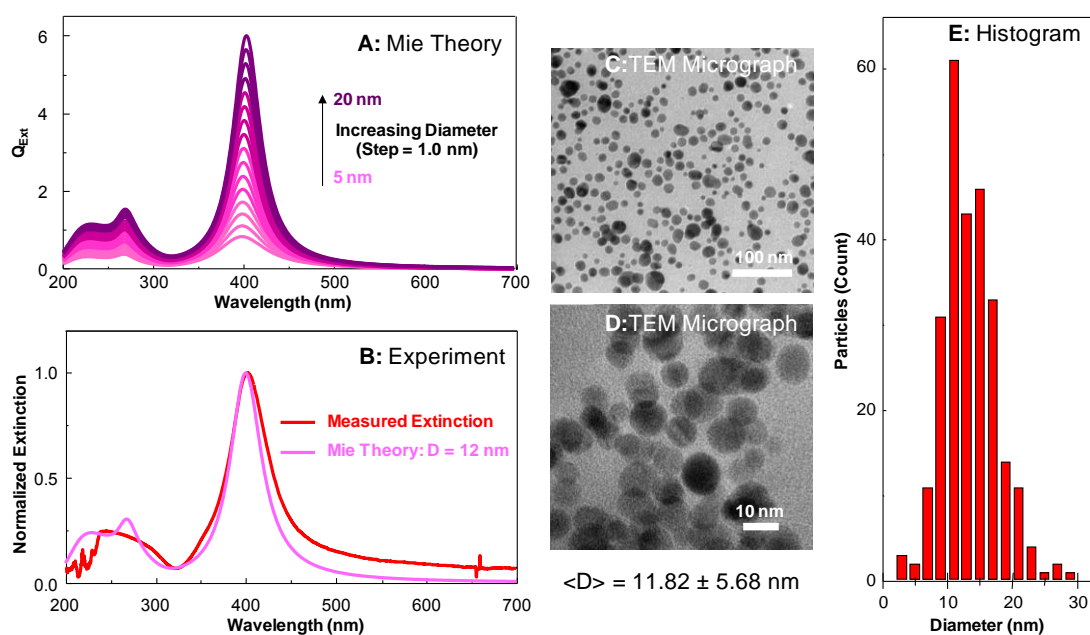
Figure 2.4 Calculated extinction spectra (A) and theoretical prediction of particle size with the extinction measured from experiment of spherical nanoparticles (B). TEM micrographs (C and D) and size distribution histogram (E) are also shown.

An example of DDA calculations on optical property in visible to near infrared region of triangular and circular Ag nanoprisms (AgNPrs) dispersed in water is shown in Figure 2.5. It clearly illustrates the shape-dependent optical property of metal nanoparticles. The extinction is contributed mainly from the absorption process. In addition, circular nanoprism exhibit higher extinction efficiency compared to triangular nanoprisms.
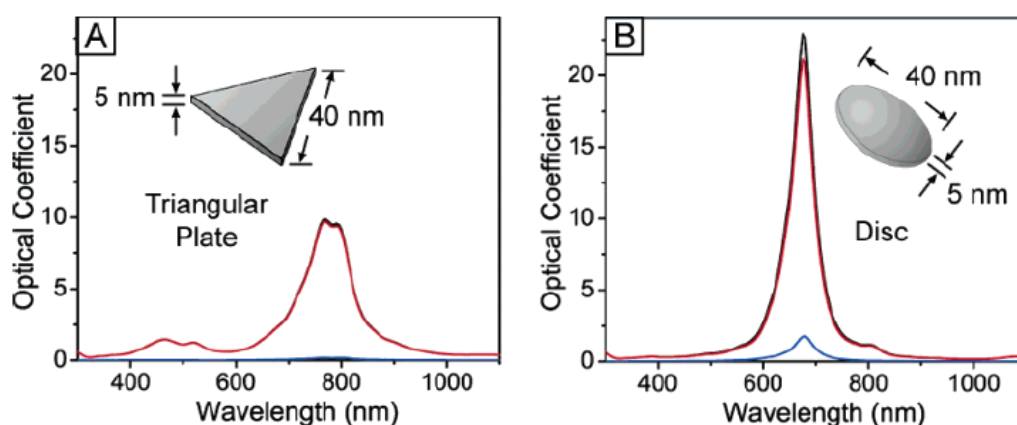
Figure 2.5　　Calculated extinction (black line), absorption (red line), and scattering (blue line) of triangular (A) and circular (B) Ag nanoprisms by DDA method [23].

Figure 2.6 shows polarization dependent extinction spectra of triangular AgNPrs with edge length of 100 nm, thickness = 16 nm, and tip snipping of 10 nm. We can see that the intense peak at 680 nm is contributed mainly from the polarization of collective electron oscillation along the plane of triangular nanostructure. Therefore, it is assigned to in-plane dipole plasmon resonance (IPDPR) of AgNPrs. When AgNPrs are polarized along its thickness, only the peak around 320 and 425 nm emerged. They are attributed to out-of-plane quadrupole plasmon resonance (OPQPR) and in-plane quadrupole plasmon resonance (IPQPR) of AgNPrs, respectively. IPQPR of AgNPrs is sensitive to the change of shape. As the shape is changed from circular to triangular nanoprisms, IPDPR redshifts from 700 nm to 800 nm. In addition, IPDPR is also sensitive to the tip-sharpness. As the triangular AgNPrs is snipped at various degree from 0 to 10 nm, IPDPR peak blueshifts from 780 nm to 600 nm, respectively

(Figure 2.7). For OPQPR mode, it does not sensitive to the change of lateral length. However, IPQPR is disappeared when nanoprisms take the circular cross section (Figure 2.5 B). As the change in shape and size of AgNPrs are directly associated with their optical property, ensemble average shape- and size of AgNPrs can be roughly predicted from UV-visible spectroscopy.
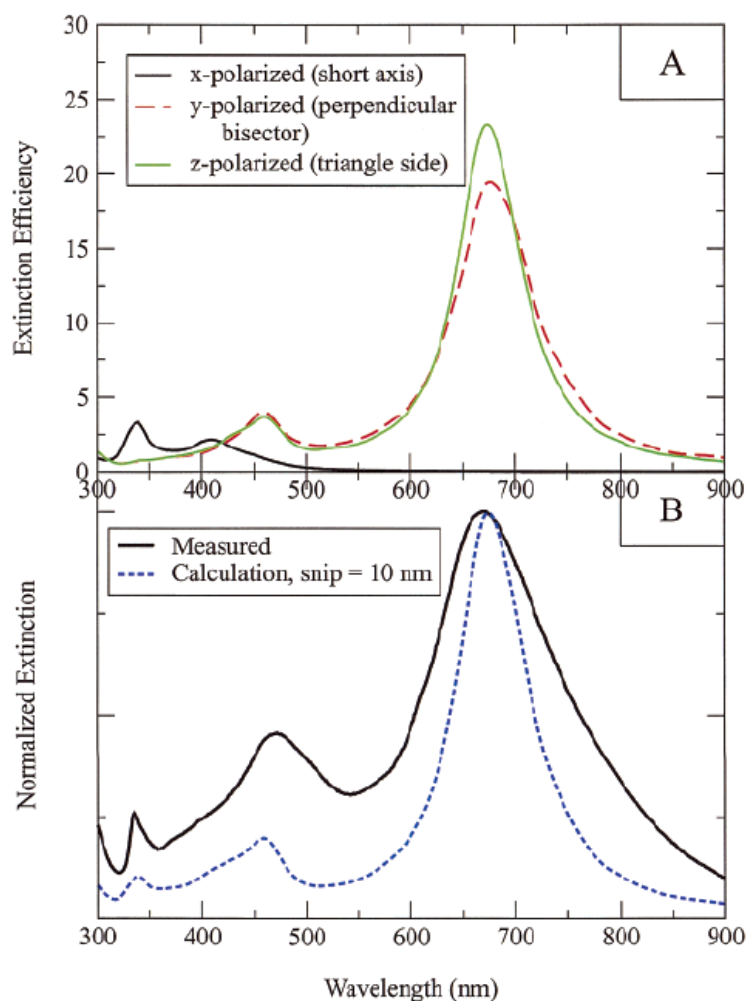
Figure 2.6   Polarization-dependent extinction of triangular AgNPrs with side length = 100 nm, snip = 10 nm, and thickness = 16 nm. (A) and comparison of calculated extinction spectra (orientation-average) with real measurement (B) [20, 24].
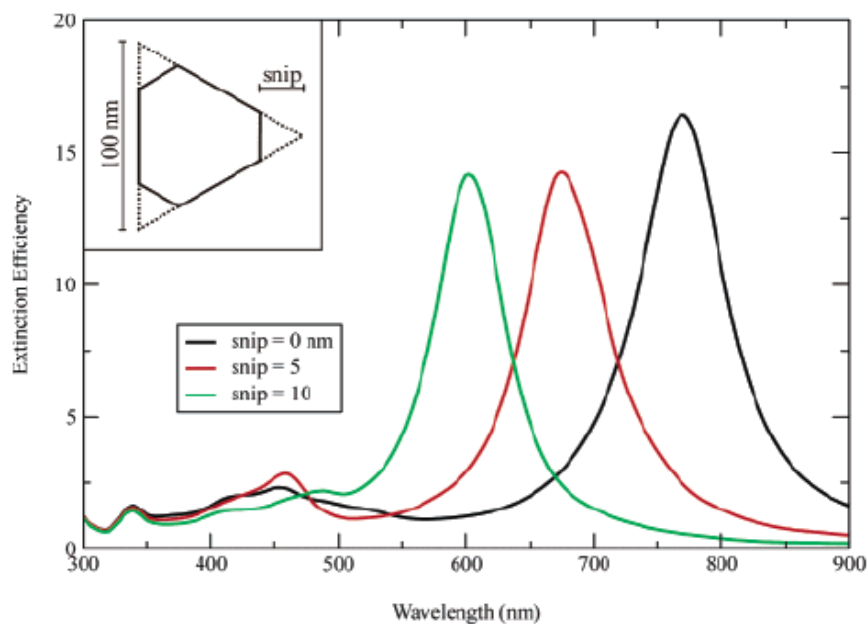
Figure 2.7   Effect of tip sharpness (snipping) on the extinction spectra of triangular AgNPrs. AgNPrs possess the edge length of 100 nm (snip = 0), thickness of 16 nm, with various degree of snipping [20].

2.2 Chemical Methods for AgNPrs Fabrication

2.2.1 Photochemical or Photoinduced Conversion

Spherical Ag nanoparticle seeds can be transformed into planar nanostructures simply by illuminating the seed colloids with appropriate wavelength of light. Illumination wavelength precisely determines the final lateral length of AgNPrs. Spherical Ag nanoparticles undergo photolysis to Ag^+, re-reduced to Ag atom, and resorp back to available nucleation sites. Trisodium citrate (TSC) play an important role as a reducing agent and capping agent promoting the expansion of {111} facets. In addition, aggregation of formed AgNPrs can be prevented by illuminating with secondary beam [25] or adjusting the solution pH [3]. However, this method requires long illumination period (more than 24 hours) and small volume of AgNPrs are obtained. Some of the reported works are summarized in Table 2.1.

2.2.2 Soft Template Method

This method utilize a monolayer of CTAB (cetyl trimethylammonium bromide), a quaternary ammonium salt, for protecting the flat top {111} facet of AgNPrs. CTAB monolayer plays a role as a template for directing the atomic addition. The protected AgNPrs can be further post-modified by thermal treatment yielding rounded nanodisks or truncated triangular AgNPrs (Table 2.2).
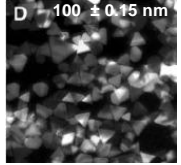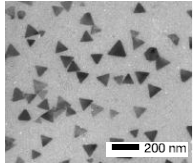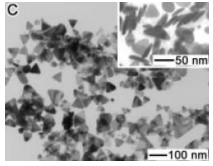
2.2.3 Thermal Reduction Method

Some of organic solvents e.g., DMF and ethylene glycol (PEG) can play a role of reducing agent. In particular, ethylene glycol is the famous solvent for colloidal metal nanoparticle fabrications due to its ability for dissolving various metal salts and reagents and controllability of reduction rate simply by adjusting reduction temperature. Ag, Au, Pd, and Pt nanoparticles with the shape of cubes, bipyramids, octahedrons, and bars can be synthesized by this method [75, 107]. Micrometer-sized AgNPrs can be synthesized by this method via oriented attachment growth pathway [119] (Table 2.3).

2.2.4 Rapid Thermal Reduction Utilizing H_2O_2

The idea on employing H_2O_2 for AgNPrs was first formally reported by Mirkin in 2005 [51]. H_2O_2 assists the formation of planar twinned seeds by selectively removing the relatively unstable facets of preformed seeds. Due to the powerful oxidizing ability of H_2O_2, it can totally disintegrate metallic Ag nanostructures e.g. nanocubes or bipyramids and exploit them as Ag^+ source for transforming into AgNPrs. The nanoprisms growth can be initiated by injecting $NaBH_4$ into the solution containing Ag^+, H_2O_2, and TSC. The AgNPrs aspect ratio is strongly dependent on $NaBH_4$ concentration. Chiral ligand can be incorporated into AgNPrs fabrication. The chirality can be transferred to the AgNPrs and induced the formation of chiral self assembly of AgNPrs [14]. Some of the methods employed H_2O_2 for AgNPrs fabrication are summarized in Table 2.4.

Table 2.1   Summary of the experimental parameters for AgNPrs fabrication utilizing photochemical or photoinduced conversion.

	Reagents and Conditions			Products
	Reducing Agent	Ag^+ Source	Shape Controller	
R. Jin *et al.* (2001) [24, 26]	$NaBH_4$	$AgNO_3$	1. BSSP 2.TSC 3. 40 W Fluorescent Light (350–400 nm) (over 70 hrs)	 Triangular Ag nanoprisms with lateral length 100 ± 0.15 nm and thickness of 15 nm
R. Jin *et al.* (2003) [25]	$NaBH_4$	$AgNO_3$ (or Ag_2SO_4 CH_3CO_2Ag $AgClO_4$)	*Step 1 (Spheres)* 1. BSPP 2.TSC *Step 2 (Prisms)* 1. Double Beam Excitation (1°: 450 – 700 nm; 2°: 340 nm) 20–50 h	 Triangular Ag nanoprisms with lateral length 30–120 nm and thickness ~ 10 nm
Y. Sun and Y. Xia (2003) [27]	$NaBH_4$	$AgNO_3$	1. TSC 2. PVP (Mw ~ 55k g mol^{-1}) 3. 20 W Halogen Lamp with a UV Cut-Off Filter (40 h)	 Triangular Ag nanoprisms with lateral length ~30–90 nm and thickness of 8.4 ± 1.3 nm
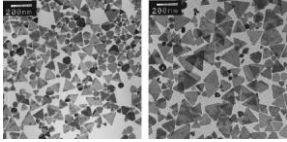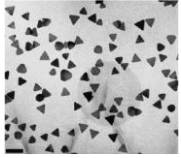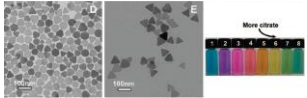
	Reagents and Conditions			Products
	Reducing Agent	Ag+ Source	Shape Controller	
V. Bastys *et al.* (2006) [29]	NaBH$_4$	AgNO$_3$	1.TSC 2. PVP (M$_w$ ~ 10k) 3. Green LEDs (518 nm) 4. Green Filter (546 nm) 5. Red Filter (610 nm) 6. Red LEDs (641 and 653 nm)	 AgNPrs with lateral length 110 ±16.6 – 242 ± 52.4 nm ; average thickness of 10.5 ± 1.8 nm; controllable plasmon extinction maxima in the range of 1037–1491 nm
C. Xue and Chad A. Mirkin (2007) [3, 26]	NaBH$_4$	AgNO$_3$	1. BSPP 2. TSC 3. NaOH or HNO$_3$ 4. 150 W Halogen Lamp (500 – 650 nm with Bandpass Filter) (over 3 hrs)	 Triangular AgNPrs with lateral length 60 ± 7 nm; coltrollable plasmon band in visible to NIR by adjusting pH and utilizng bandpass filter
B. Tang *et al.* (2009) [28]	NaBH$_4$	AgNO$_3$	1. TSC 2. Sodium Lamp (80.6 mW/cm^2) (Irradiation Time)	 AgNPrs with controllable LSPR wavelength from 740–440 nm (Conversion) or 620–690 nm (reconstruction)

Table 2.2   CTAB monolayer soft template method for AgNPrs fabrication.
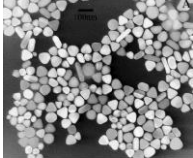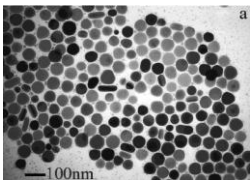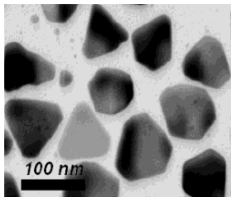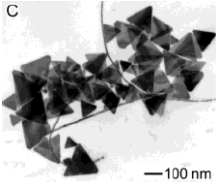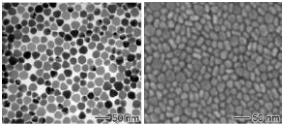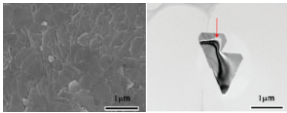
	Reagents and Conditions			Products
	Reducing Agent	Ag⁺ Source	Shape Controller	
S. Chen and D. L. Carroll (2002) [42]	*1.Seeding* NaBH$_4$ *2.Growth* Ascorbic Acid	AgNO$_3$	*1.Seeding* TSC *2.Growth* 1. CTAB 2. NaOH *3. Aging* Thermal Treatment (21 ^{o}C for 12 h; 35 ^{o}C for 5 min; 21 ^{o}C for 24 h)	Truncated triangular Ag nanoprisms with edge size = 68 ± 11 nm; thickness = 24 ± 3.5 nm; degree of truncation = 0.35 ± 0.056 nm
S. Chen, Z. Fan and D. L. Carroll (2002) [43]	*1.Seeding* NaBH$_4$ *2.Growth* Ascorbic Acid	AgNO$_3$	*1.Seeding* TSC *2.Growth* 1. CTAB 2. NaOH *3. Aging* Thermal Treatment (40 ^{o}C from 5 min to 57 h;	Ag nanodisks with diameter = 59 ± 10 nm; thickness = 26 ± 3.4 nm

Table 2.3   Thermal reduction method for AgNPrs synthesis.

	Reagents and Conditions			Products
	Reducing Agent	**Ag$^+$ Source**	**Shape Controller**	
I. Pastoriza-Santos and L. M. Liz-Marzán (2002) [40, 41]	DMF	AgNO$_3$	1. [Ag$^+$] 2. DMF Reflux 3. PVP	 Ag nanoprisms with triangle as dominant shape with average edge length of 80 nm
Y. Sun, B. Mayers, and Y. Xia (2003) [45]	NaBH$_4$	AgNO$_3$	1.TSC 2. PVP (Mw ~ 55k g mol-1) 3. Refluxing in Oil Bath at 105 ^{o}C	 Triangular Ag nanoprisms (95%) and wire – like nanostructures (5%)
Y. Xiong *et al.* (2007) [47]	Ethylene Glycol	AgNO$_3$	1.Polyacrylamide 2. Reaction Temperature (135 ^{o}C) 3. Reaction Time (3h)	 Triangular Ag nanoprisms with lateral length of 25 nm, thickness of 10 nm, and various degree of truncation

	Reagents and Conditions			Products
	Reducing Agent	Ag⁺ Source	Shape Controller	
Z. Liu *et al.* (2012) [119]	PEG400 – Water Mixture Solution	AgNO$_3$	1. PVP (Mw ~ 10k) Concentration 2. Reaction Temperature (98 ^{o}C at 10 ^{o}C/min for 2 h and 108 ^{o}C) 3. PEG400 – Water Mixing Ratio	Planar nanostructures with edge length in the range of 300 – 1000 nm and average thickness ~ 25 nm

2.2.5 Kinetically-Controlled Growth Pathway
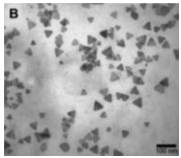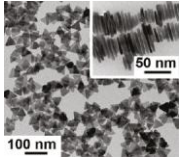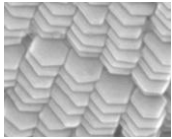
In terms of surface energy, the formation of thin nanoplates is unfavorable. Even though the nanoplate structures have a large {111} surface coverage, the total surface energy of a thin nanoplate is much higher, because of a larger surface area and the lattice strain caused by stacking faults. When the growth of metal nanoparticles is deviated from the thermodynamic controlled pathway, the formation of nanoprisms is possible. Slow reduction rate and limited number of atoms available is the two important criteria for confining the kinetically-controlled condition of nanoprism growth. This can be carried out by utilizing mild reducing agent or chelating agent (Table 2.5)

2.2.6 Seed-Mediated Approach

Seed mediated approach (Table 2.6) is an efficient method for completely separating the nucleation and growth from each other. Lateral length of AgNPrs can be systematically controlled through the number of growth cycle. Nowadays, AgNPrs

with tailoring thickness and edge length from nanometer to micrometer scales can be fabricated by this approach [35]. The formation of planar twinned seeds can also be promoted during the seed preparation step by utilizing H_2O_2.

Table 2.4 Rapid thermal reduction utilizing H_2O_2 for AgNPrs synthesis.

	Reagents and Conditions			Products
	Reducing Agent	Ag$^+$ Source	Shape Controller	
G. S. Métraux and Chad A. Mirkin (2005) [51]	NaBH$_4$	AgNO$_3$	1.H$_2$O$_2$ 2. PVP 3.TSC	Triangular AgNPrs with Lateral Length 24–50 nm and tailorable thickness
Q. Zhang *et al.* (2011) [52]	NaBH$_4$	AgNO$_3$ or Metallic Silver	1. H$_2$O$_2$ 2.TSC or Other Carboxylate Compounds 3.PVP, PVA, Ethanol, EG, DEG, TEG, or Glycerol	Triangular AgNPrs with thickness 6 – 3.5 nm and aspect ratio of 11 – 3 (depending on [NaBH$_4$])
N. Cathcart and V. Kitaev (2011) [14]	1. NaBH$_4$ 2. Citric Acid	AgNO$_3$	1. Captopril 2. H$_2$O$_2$ 3. KCl 4. KOH	Monodisperse hexagonal AgNPrs with lateral length of 20–110 nm and thickness of 5–20 nm
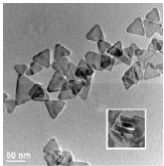
	Reagents and Conditions			Products
	Reducing Agent	Ag$^+$ Source	Shape Controller	
M. Tsuji *et al.* (2012) [28]	NaBH$_4$	AgNO$_3$ or Metallic Silver (e.g. Cube, and Rod)	1.TSC or Other Carboxylate Compounds 2. PVP 3. H$_2$O$_2$	Triangular AgNPrs with lateral length of 44 ± 8 nm and average thickness of 10 nm

Table 2.5　　　Kinetically-controlled growth of AgNPrs.
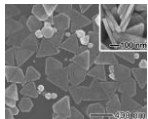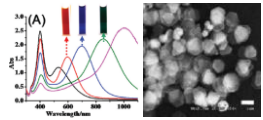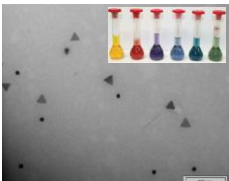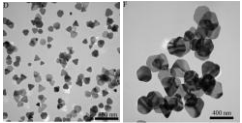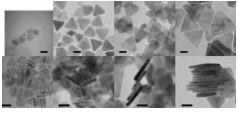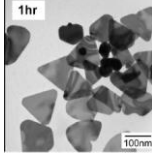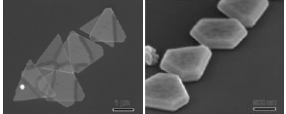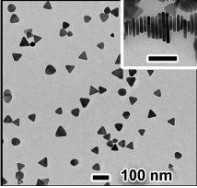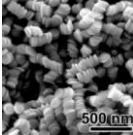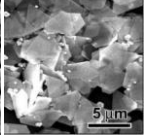
	Reagents and Conditions			Products
	Reducing Agent	Ag$^+$ Source	Shape Controller	
I. Washio *et al.* (2006) [44,122]	PVP Mw ~ 29k g mol^{-1}	AgNO$_3$	1.PVP:Ag$^+$ = 30 2. T = 60 ^{o}C 3. Reaction Time	Triangular AgNPrs with edge length of 90–350 nm
Z. Cao *et al.* (2008) [49]	Saturated Solution of Ag$_2$O	Hydrazi-ne (N$_2$H$_4$)	1. Ag$_2$O:TSC = 1:9 2. Ag$_2$O:N$_2$H$_4$ = 1:3 3. 0.1 M EDTA Volume	Triangular or Hexagonal AgNPrs with lateral lengths of 30–170 nm and thickness of 8.5–15 nm and controllable plasmon maxima in the range of 500–1100 nm

Table 2.6   Seed-Mediated Approach for AgNPrs fabrication.

	Reagents and Conditions			Products
	Reducing Agent	Ag⁺ Source	Shape Controller	
D. M. Ledwith *et al.* (2007) [33]	*Step 1* NaBH$_4$ *Step 2* Ascorbic Acid	AgNO$_3$	*Step 1* 1.TSC (Ice Cooled) *Step 2* 1.Concentration of TSC 2. PVP (M$_w$ ~ 10k) 3. Reaction Temperature	Triangular Ag nanoprisms with lateral length of 64 ± 10 nm – 81 ± 15 nm depending on the reaction temperature; Plasmon band can be controlled in visible range by adjusting an amount of TSC
X. Zou *et al.* (2007) [31]	*Step 1* NaBH$_4$ *Step 2* Hydrated Hydrazine	AgNO$_3$	1. TSC 2. PVP 3. Seed Sizes 4. [Ag⁺]	AgNPrs with controllable lateral length in the range of 25–1073 nm and dipole SPR from visible to NIR (458–2400 nm)

	Reagents and Conditions			Products
	Reducing Agent	Ag$^+$ Source	Shape Controller	
D. Aherne *et al.* (2008) [5]	*Step 1* NaBH$_4$ *Step 2* Ascorbic Acid	AgNO$_3$	1. TSC 2. PSSS 3. Seed Volume 4. [Ag$^+$] Feed Rate	Triangular AgNPrs with lateral length in the range of 20–100 nm and thickness of 5–6 nm
S. T. Gentry and S. D. Levit (2009) [30, 32]	NaBH$_4$	AgNO$_3$	1. Hydroquinone 2.TSC, PVP, or PVA 3. pH	Mixed geometries of AgNPrs with lateral length of 80–150 nm and thickness of 8 nm
J. Zeng *et al.* (2011) [35]	*Seeding* 1. NaBH$_4$ 2. L – Ascorbic Acid *Growth* 1. L – Ascorbic Acid	AgNO$_3$	*Seeding* 1. TSC 2. PVP (M$_w$ ~ 29k) *Lateral Growth* TSC *Vertical Growth* PVP (M$_w$ ~ 29k)	Triangular AgNPrs with lateral length 45 ± 15 – 5.0 ± 0.5 μm and thickness of 5 ± 0.5 nm – 25 ± 4 nm (Lateral Growth) or triangular AgNPrs with lateral length of 45 – 600 nm and thickness of 5–200 nm (Vertical Growth)
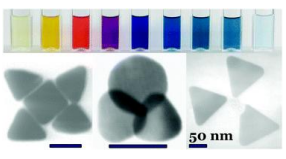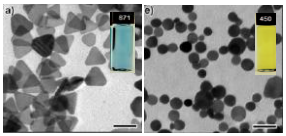
	Reagents and Conditions			Products
	Reducing Agent	Ag$^+$ Source	Shape Controller	
N. Li *et al.* (2012) [54]	NaBH$_4$	AgNO$_3$	1. H$_2$O$_2$ 2.TSC or Other Carboxylate Compounds 3. Ascorbic Acid	Triangular Ag nanoprisms with lateral length of 30–70 nm and thickness of 5 nm
Q. Zhang *et al.* (2010) [8, 34]	*Step 1* NaBH$_4$ *Step 2* L – Ascorbic Acid	*Step 1* AgNO$_3$ *Step 2* AgNO$_3$ + Citrate (Ag – Cit. Complex)	*Step 1* 1.TSC 2. PVP (M$_w$ ~ 29k) 3. H$_2$O$_2$ *Step 2* 1.Citric Acid 2.TSC 3. Ag – Cit. Complex Injection Rate	Ag nanoprisms with lateral length in the range of 25–4000 nm and thickness of 6–10 nm; controllable in-plane dipole SPR in the range of 400–2800 nm
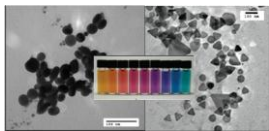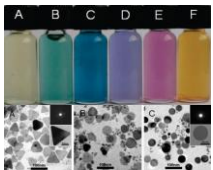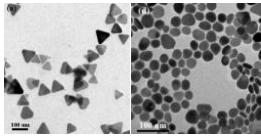
2.2.7 Post Modification Approach

AgNPrs is highly active toward the oxidative etching by the presence of halide or organic anion e.g. Br$^-$, Cl$^-$ and SCN$^-$, UV photolysis, or thermal energy. Therefore, it is possible for sculpturing the preformed AgNPrs and yielding the smaller AgNPrs. The extent of sculpturing is controlled by limiting the anion concentration, irradiation time, or adding protecting agent (organic acid with thiol functionality). The final

sculptured AgNPrs take the form of circular nanodisks. In some cases, after the post-modification, AgNPrs exhibit more stability toward the chemical or surrounding changes.

Table 2.7 Post-modification or sculpturing method of the preformed AgNPrs.

	Reagents and Conditions			Products
	Reducing Agent	Ag⁺ Source	Shape Controller	
N. Cathcart *et al.* (2009) [38]	NaBH$_4$	AgNO$_3$	1.TSC 2. H$_2$O$_2$ 3. Br⁻ or Cl⁻ Concentration (formation and modification) 4. Aging Time	 Triangular, hexagonal or rounded Ag nanoprisms with lateral lengths of 20−100 nm and thickness of 12–6 nm; controllable plasmon resonance in the range of 400–900 nm
Q. Zhang *et al.* (2009) [39]	NaBH$_4$	AgNO$_3$	*Step 1* 1.TSC 2. PVP (M$_w$ ~ 29k) 3. H$_2$O$_2$ *Step 2* UV Light Source (365 nm, 120 V, 1.05 amp)	 Triangular and circular Ag nanoplates with edge length of 48.52 ± 6.27 − 26.07 ± 5.87 nm and thickness of 3.08 ± 0.57 − 8.6 ± 1.08 nm

	Reagents and Conditions			Products
	Reducing Agent	Ag⁺ Source	Shape Controller	
Bo-Hong Lee *et al.* (2010) [4]	NaBH$_4$	AgNO$_3$	*Step 1* 1.TSC 2. Sodium Lamp (100 W, 589 nm) *Step 2* 1.PVP 2. Bromide Ion 3. MHA	Ag nanoprisms with controllable in-plane dipole SPR in the range of 465–675 nm
B. Tang *et al.* (2008) [36] (Heat)	NaBH$_4$	AgNO$_3$	1. TSC 2. Time of Heating at 95 ^{o}C	Ag nanodisks with controllable diameter in the range of 39–57 nm and tunable LSPR in the range of 472–655 nm
Chin-Ming Tsai et al. (2012) [37]	NaBH$_4$	AgNO$_3$	*Step 1* 1.TSC 2. Sodium Lamp (400 W, 589 nm) *Step 2* 2 – 5 x 10^{-4} M KSCN	Ag nanoprisms or Ag nanodisks with controllable in-plane dipole SPR in the range of 465–670 nm

CHAPTER III

EXPERIMENTAL SECTION

3.1 AgNPrs Synthesis and Characterization

3.1.1 Materials and Chemicals

1. Silver nitrate ($AgNO_3$) (Analytical Reagent (AR) Grade, Merck)
2. Sodium borohydride ($NaBH_4$) (Analytical Reagent (AR) Grade, Merck)
3. Soluble starch (Analytical Reagent (AR) Grade, Merck)
4. Trisodium citrate dihydrate (Analytical Reagent (AR) Grade, Merck)
5. 30% (w/w) hydrogen peroxide (H_2O_2) (Analytical Reagent (AR) Grade, Merck)
6. 65% (w/w) Concentrated Nitric Acid (HNO_3) (Analytical Reagent (AR) Grade, Merck)
7. De-ionized (DI) water

All purchased chemicals were used as received without any additional purification. All glassware and magnetic stir bars were rinsed with 6 M nitric acid, cleaned with washing detergent, and then thoroughly rinsed with de-ionized (DI) water prior to use.

3.1.2 Instruments & Equipments

1. Hotplate stirrer (IKA$^{®}$ C-MAG H27)
2. High Performance Disperser (IKA$^{®}$ T25 ULTRA – TURRAX$^{®}$)
3. Syringe Pump (NE-1000 Programmable Single Syringe Pump, New Era Pump System, Inc.)
4. Rectangular quartz cuvette 10 mm path length, 3.5 mL volume

5. Ocean Optics USB4000 Fiber Optic Spectrometer

6. DH-2000 deuterium/halogen light source

7. Cuvette holder, 1-cm path, 200–2000 nm

8. Hitachi Model H-7650 transmission electron microscope

9. JEOL JSM-6510 Scanning electron microscope coupled with energy-dispersive X-Ray (EDX) detector

10. Double-sided carbon tape (Electron Microscopy Sciences)

11. Nicolet 6700 FT-IR spectrometer (Thermo Electron Corporation, Madison, WI, USA) equipped with a mercury-cadmium-telluride (MCT) detector

12. Continuμm^{TM} infrared microscope with a built-in 15X Schwarzschild-Cassegrain infrared objective and a 10X glass objective.

13. Homemade slide-on Ge μATR accessory with a cone-shaped Ge as IRE.

14. 200 mesh Formvar-coated copper grid (Electron Microscopy Sciences)

15. JEOL Aluminum mounts (Standard: 10 mm (diameter) × 10 mm (height)) (Electron Microscopy Sciences)

16. BRAND Starter – Kit Standard Transferpette$^{®}$ S

3.1.3 Stabilizer Solution Preparation

In a typical experiment, the stabilizer solution was prepared by slowly added 20 g of soluble starch into 1000 mL of boiling DI water. After completing the addition, the solution was continuously boiled for another 30 minutes before cooling down to room temperature. The final volume of the solution was adjusted to 1000 mL with DI water. Unless stated otherwise, the 2% (w/v) starch solution was employed as the solvent.

3.1.4 Silver Nanospheres (AgNSs) Seeds Preparation

The AgNSs preparation procedure is depicted in Figure 3.1. Typically, 0.63 g of $AgNO_3$ was dissolved in 500 mL of the stabilizer solution. The aqueous solution of reducing agent was prepared by dissolving of 0.21 g $NaBH_4$ in 500 mL of the

stabilizer solution. The prepared $AgNO_3$ solution was injected into the reducing solution at a rate of 2 mL/s under a vigorous stir. The total volume of the colloid was adjusted to 1300 mL with DI water, and the stirring was continued for additional 30 minutes. The synthesized AgNSs colloid was boiled for 2 hours. Then, the colloid was cooled down to room temperature and aged for 12 hours to ensure an elimination of residual $NaBH_4$ [38, 53–54, 62]. The final volume of the synthesized AgNSs colloid was adjusted to 1000 mL with DI water. The final concentration in term of total silver content in the synthesized AgNSs colloid was 400 mg/L (ppm) or 3.7 mM. For preparation of AgNSs with initial concentrations ranging from 100 ppm – 1200 ppm, the required weights of $AgNO_3$ and $NaBH_4$ are summarized in Table 3.1. The diameter of the synthesized AgNSs colloid was 6.03 ± 2.60 nm (Figure 3.2). The synthesized AgNSs colloid was used within 24 hours after the preparation.
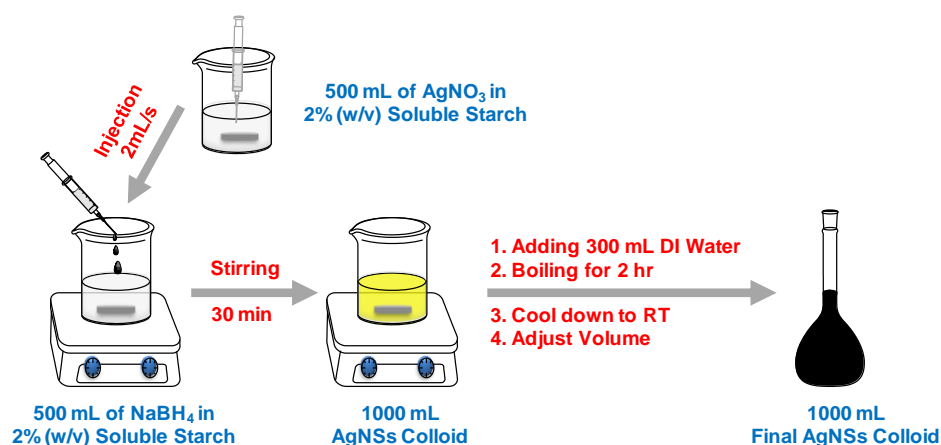
Figure 3.1   Preparation of AgNSs seed colloid.
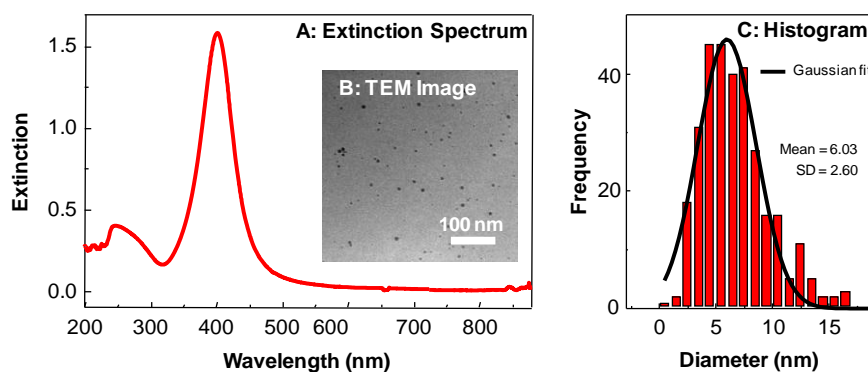
Figure 3.2   Typical extinction spectrum (A), TEM micrograph (B), and size distribution histogram of AgNSs seed colloid (C).

Table 3.1   Calculated weights of $AgNO_3$ and $NaBH_4$ for preparation of AgNSs with specified concentration in ppm (or mM) at total volume of 1000 mL.

Concentration of AgNSs (ppm/mM with respect to total Ag^+)	Weight of $AgNO_3$ (g)	Weight of $NaBH_4$ (g)
100/0.927	0.157 ± 0.005	0.059 ± 0.001
200/1.854	0.315 ± 0.005	0.109 ± 0.001
300/2.781	0.472 ± 0.005	0.159 ± 0.001
400/3.708	0.630 ± 0.005	0.209 ± 0.001
500/4.635	0.787 ± 0.005	0.259 ± 0.001
600/5.562	0.945 ± 0.005	0.309 ± 0.001
700/6.489	1.102 ± 0.005	0.359 ± 0.001
800/7.416	1.260 ± 0.005	0.409 ± 0.001
900/8.344	1.417 ± 0.005	0.459 ± 0.001
1,000/9.270	1.575 ± 0.005	0.509 ± 0.001
1,100/10.198	1.732 ± 0.005	0.559 ± 0.001
1,200/11.125	1.890 ± 0.005	0.609 ± 0.001

3.1.5 Shape Transformation of AgNSs to AgNPrs

The instrumental setup for shape transformation experiment is displayed in Figure 3.3. In a typical experiment, 2.65 mL of 30% H_2O_2 solution was injected to 200 mL of 400 ppm colloidal AgNSs in a 500 mL Teflon beaker at the rate of 13.45 mL/min under a vigorous stir. The mole ratio R of H_2O_2: AgNSs was 35. H_2O_2 was employed for the particle growth instead of $NaBH_4$ [51–53]. The volume and injection rate of H_2O_2 addition were controlled by a syringe pump. A high performance disperser was employed as the mechanical stirrer. The homogenizing speed was set at 15k rpm. The H_2O_2 solution was dispensed into the AgNSs seed colloid via a tygon tube with an inner diameter of 1.35 mm. After the complete

addition of H_2O_2 solution (approximately 15 seconds), the mixed solution was further stirred for additional 10 minutes to ensure the complete reaction.
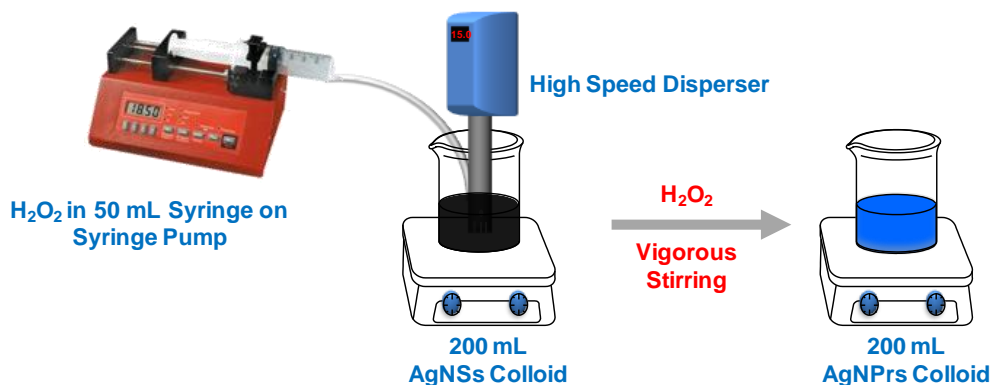
Figure 3.3   Experimental setup for shape transformation experiment.

For other initial AgNSs concentrations and volumes, the injected volume of 30% (w/w) H_2O_2 can be calculated by the following equation:

$$V_{H_2O_2} = \frac{1}{107.8682 \times 1000} \times \frac{C_{AgNSs} \times V_{AgNSs} \times R}{C_{H_2O_2}} \tag{3.1}$$

where $V_{H_2O_2}$ is volume of H_2O_2 in mL, C_{AgNSs} is concentration of AgNSs in mg/L, V_{AgNSs} is volume of AgNSs in mL, $C_{H_2O_2}$ is concentration of H_2O_2 in molar, and R is the molar ratio of H_2O_2:AgNSs.

3.1.6 Characterizations

Plasmon extinction spectra of Ag nanoparticles were recorded by an Ocean Optics USB4000 Fiber Optic Spectrometer coupled with a DH-2000 deuterium/halogen light source. All samples were diluted with DI water to the same concentration (10 mg/L) before each measurement. The spectral artifacts centered at 650 nm for each measured spectrum are inevitably come from the light source and are not correlated with the resulted spectra. TEM micrographs of Ag nanoparticles were

recorded with Hitachi Model H-7650 transmission electron microscope operated at 100 kV. The as-synthesized colloids were purified by washing with DI water through the ultracentrifugation and re-dispersed in DI water. The purified colloid was drop-coated on Formvar-coated copper grids (200 mesh) and dried at room temperature in a desiccator for 24 hours before TEM measurements. Dimensions of the silver nanoparticles were measured directly from the micrographs using ImageJ [63]. The molecular characteristics of the soluble starch and its related products were acquired by ATR FT-IR microspectroscopy via a Nicolet 6700 FT-IR spectrometer coupled with the Continuμm infrared microscope equipped with a mercury-cadmium-telluride (MCT) detector. A built-in 15X Schwarzschild-Cassegrain infrared objective was employed for all spectral acquisitions. A slide-on cone-shaped Ge μIRE (Figure 3.4) was employed as the sampling probe [109].
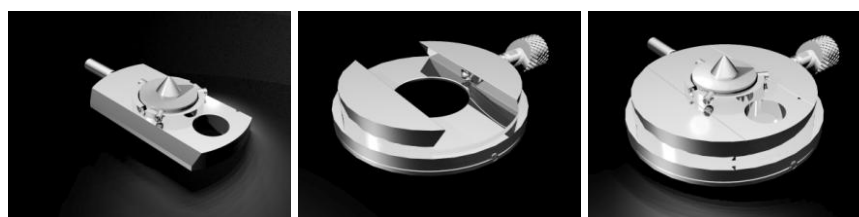
Figure 3.4   A slide-on cone-shaped Ge μIRE and its housing [109].

Virgin starch solution, starch-stabilized AgNSs colloid, and starch-stabilized AgNPrs colloid were dropped onto a glass slide and dried under an ambient condition before subjected an infrared spectral acquisition [110–111]. The dried film on the glass slide was mounted onto the sample stage beneath the infrared objective (Figure 3.5).
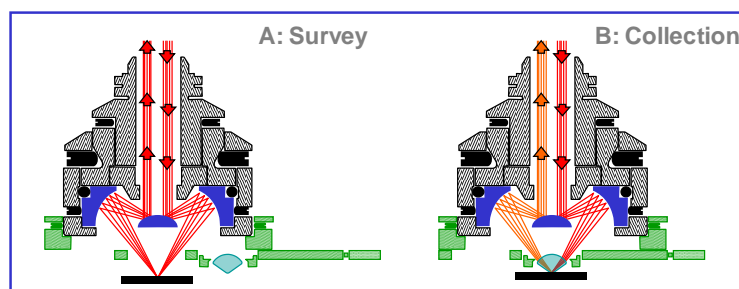
Figure 3.5   Normal operation for ATR FT-IR spectral acquisition utilizing slide-on cone-shaped Ge μIRE [109].

The spectral acquisition at a defined position was conducted by raising the sample stage until the film on the glass slide comes in contact with the tip of Ge μIRE. The degree of contact was monitored and controlled by a built-in pressure sensor. All ATR spectra were collected at 4 cm^{-1} with 128 co-addition scans.

3.1.7 Chemometric Data Analysis

This part of the works was contributed by Dr. Kanet Wongravee. Statistical and chemometric analyses of the spectroscopic data were performed in MATLAB (Mathwork, Inc. Version R2011b). The software to determine the number of main components and initial estimation was developed by our group. We recommend that the reader should consult the master degree thesis by Dr. Kanet Wongravee [102] for comprehensive details of software development, validation, and implementation. The MCR-ALS analysis was achieved using the MCR-ALS program with graphical user interface (GUI) facility developed by Tauler et al. [103].

3.2 Antibacterial Activity Evaluation of AgNPrs

This part of the works was contributed by Mr. Kamol Rodyou and Associate Professor Sirirat Rengpipat of Department of Microbiology, Faculty of Science, Chulalongkorn University.

3.2.1 Tested Bacteria
1. *Escherichia coli* ATCC 25922
2. *Staphylococcus aureus* ATCC 25923
3. Methicillin-resistant *Staphylococcus aureus* (MRSA)
4. *Acinetobacter baumannii*
5. *Pseudomonas aeruginosa* ATCC 27853

3.2.2 Test Method

The antibacterial activity of AgNPrs was evaluated via the total plate count method.

3.2.3 Test Procedure

3.2.3.1 Preparation of Inoculums

The bacteria subjected to the test were cultivated in the Tryptic Soy Broth (Difco^{TM}) culture medium. Then, they were incubated in incubator shaker at 37 ^{O}C for 9 hours at the rotor speed of 200 rounds per minutes (rpm). The cultured bacteria were separated from the cultured media by centrifugation at 8,000g for 10 minutes. After washing with normal saline by ultracentrifugation, the bacteria were resuspended in Peptone water (Difco^{TM}) for employing as inoculums.

3.2.3.2 Preparation of AgNPrs

1,000 ppm blue AgNPrs (Figure 3.6) were measured in 12x100 mm test tube containing with 3 mL DI water as solvent at the dose of 1, 2.5, 5, 10, and 20 ppm for the test.

3.2.3.3 Inoculation of the Test Tube

0.1 mL of inoculum was transferred to the solution obtained in 3.2.3.2, whilst another 0.1 mL of inoculum was transferred to the control medium (normal saline solution). The initial amount of tested bacteria were selectively controlled in the range of $1x10^5$–$1x10^6$ CFU/mL.

3.2.3.4 Incubation

Two test tubes from 3.2.3.3 were incubated at 25 ^{O}C for 24 hours at rotor speed of 200 rpm in incubator shaker.

3.2.3.5 Bacteria Counting

There were three set of sample of bacterial counted for comparison i.e. the initial bacteria (after the preparation of inoculum), the control set, and the AgNPrs + bacteria test set. The bacterial colony forming units (CFU) were evaluated through the total plate count method on Nutrient agar (Difco^{TM}) culture medium. The percent reduction of microorganism was evaluated by Eq. 3.2:

$$\% \text{ Reduction} = \frac{X_{Control} - X_{24\,h}}{X_{Control}} \times 100 \qquad (3.2)$$

where $X_{Control}$ is the amount of bacteria in the control set, $X_{24\,h}$ is the amount of bacteria survived after 24 hours in the test set, and %Reduction is the antibacterial activity.
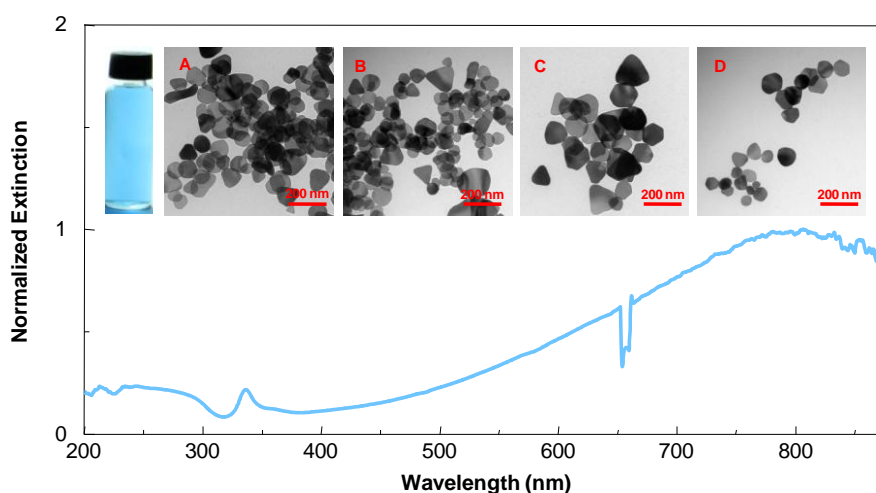
Figure 3.6   Photograph, plasmon extinction spectrum, and TEM micrographs of 1000 ppm "blue" AgNPrs.

3.3 Antiseptic Wound Dressing Prototyping and Clinical Tests

This part of the works was contributed by Novatec Healthcare, Co., Ltd. and Thai Nanocellulose, Co., Ltd. The fabrication procedures are trade secret. Surface morphology characterization of the wound dressing was performed on scanning electron microscope. The sample was prepared by drying a thin-specimen of wound dressing on an aluminum stub at ambient condition.

CHAPTER IV

RESULTS AND DISCUSSION

4.1 Preliminary Observations

The idea on employing H_2O_2 for AgNPrs synthesis was firstly reported in the publication by Métraux in 2005 [51]. The shape transformation reaction was accomplished by direct chemical reduction of silver ion (Ag^+) with sodium borohydride ($NaBH_4$) in the presence of H_2O_2, along with citrate as the capping agent and/or PVP as the polymeric stabilizer. H_2O_2 was utilized as the powerful oxidative etching agent that singled out the seeds with highest stability. Here, we primarily carried out the shape transformation experiment with some modifications from the previous reports [51–53] by replacing citrate and PVP with soluble starch in order to explore the feasibility in removing surface capping agents for colloidal anisotropic nanostructure fabrication. The experimental procedure is outlined in Figure 4.1.
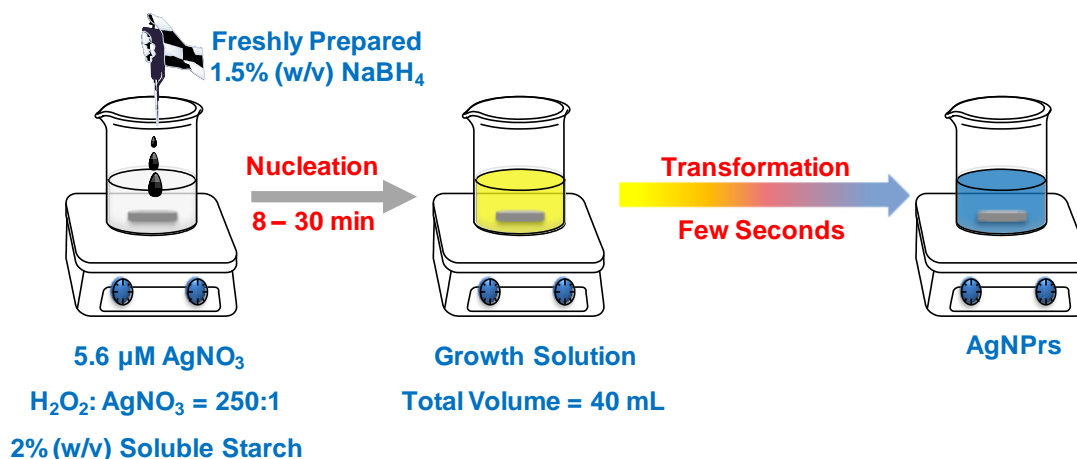
Figure 4.1   The experimental setup for the preliminary observations on the chemical shape transformation without surface capping agents.

First of all, 0.139 mM $AgNO_3$ was mixed with H_2O_2 at the molar ratio of H_2O_2:$AgNO_3$ = 250 in 40 mL of 2% (w/v) soluble starch solution. The shape

transformation was initiated by rapidly injecting 1.5% (w/v) $NaBH_4$ solution at the molar ratio of $NaBH_4:AgNO_3 = 7.14$ into the premixed solution. Immediately after $NaBH_4$, the transparent premixed solution became very light pale yellow indicating the formation of spherical silver nanoparticles. The solution color remained unchanged for 459 s before the initial burst of intense yellow color (Figure 4.2 D–F). The solution color progressively changed from yellow to orange, pink, purple, violet, and blue within 36 s (Figure 4.2 E–O). These change indicated the rapid shape transformation of Ag nanoparticle since the optical property is directly associated with the shape and size of the nanoparticles [1, 20, 24–25]. After the initial burst for 67 seconds, the solution color was unchanged indicating the termination of the shape transformation.

A	B	C	D	E	F	G	H
Pre-Mixed Solution	$NaBH_4$ Injection	436 s After $NaBH_4$	459 s Initial Burst	459 s Fast Transition	467 s (8 s) Initiation	472 s (13 s) Prism Growth	474 s (15 s)

I	J	K	L	M	N	O	P
476 s (17 s)	481 s (22 s)	484 s (25 s)	486 s (27 s)	488 s (29 s)	491 s (32 s)	495 s (36 s)	526 s (67 s) Termination
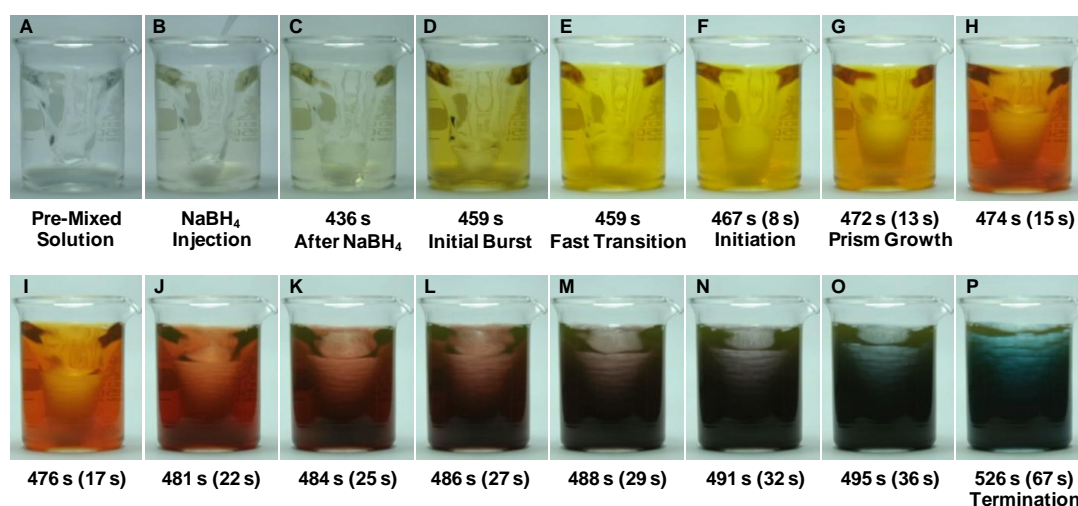
Figure 4.2   The shape transformation progress as observed from the change in solution color recorded from the VDO recorder. The number in the parentheses indicates the relative time interval with respect to the initial burst of the solution color (D).

The time-resolved extinction spectra of the shape transformation experiment are shown in Figure 4.3. The initial solution (after the injection of $NaBH_4$) showed the peak at 250 nm in UV region. The peak is associated with H_2O_2 (Figure 4.5). H_2O_2 was consumed overtime in the transformation progress since the intensity of the peak was gradually reduced. The tailing peak from 280–500 nm corresponds with the pale

yellow color observed in Figure 4.2 B and D. This tailing peak occurred after $NaBH_4$ was injected into the premixed solution of $AgNO_3$+$NaBH_4$+starch. It associated with the extremely small (diameter < 5 nm) spherical AgNPs primarily formed since broad extinction spectra of such species were predicted by the theory and observed experimentally [104]. At the initial burst (1.2 s), there was an extinction peak at 415 nm. This peak rapidly redshifted to 425 nm within 1.2 s with the development of shoulder peak around 375 nm and 350 nm. These observations were different from the earlier reports [52] that the peak initially observed after the nucleation burst was around 400 nm corresponding to the spherical AgNPs. From the spectroscopic evidence, we anticipated that the initial shape of the nanoparticles developed in our system partially possessed the nanoplate-like structures with spherical profiles [105]. As the shape transformation progressed, the peaks at 425 nm redshifted to 608 nm in corresponding with the solution color change indicating the lateral enlargement of the AgNPrs. The peak at 608 nm corresponds to the in-plane dipole plasmon resonance (IPDPR) of the AgNPrs. The time-dependent extinction intensity at 608 nm (Figure 4.4) clearly exhibit the AgNPrs evolution profile from initiation at first 20 s to rapid growth during 20–60 s, and growth termination after 70s. There were other two extinction peaks evolved during the shape transformation, namely, the peak at 458 nm and 339 nm, corresponding to the in-plane and out-of-plane quadrupole plasmon resonances (IPQPR and OPQPR). These spectroscopic evidences confirmed that our obtained final nanostructures were nanoprisms. These observations clearly told us that we can fabricate the anisotropic nanostructures without employing the surface specific capping agents. In the next step, we will identify the chemical reagents and factors that play the key role in the chemical shape transformation.

In the standard experimental condition, $AgNO_3$, H_2O_2, and starch were premixed in the solution before the injection of $NaBH_4$. When H_2O_2 was excluded from the premixed solution, the resulted yellow colloid exhibited only the dipole plasmon resonance (DPR) peak at 401 nm corresponding to the spherical AgNPs with diameter 4.12 ± 0.75 nm (Figure 4.6 A). The spherical AgNPs with larger diameter and broader size distribution of 10.92 ± 3.14 nm were obtained when starch and H_2O_2 were excluded from the synthesis (Figure 4.6 B). When H_2O_2 was included in the synthesis

without utilizing starch as a stabilizer, still there were no AgNPrs formed since the resulted colloid exhibited only the DPR peak at 402 nm (Figure 4.6 C). However, the diameter of the spherical nanoparticles was smaller than that of Figure 4.6 B. The AgNPrs were formed only when all the reagents in the standard experimental conditions were included (Figure 4.6 D). The plasmon extinction peaks at 608, 458, and 399 nm corresponding to IPDPR, IPQPR, and OPQPR of AgNPrs. The colloidal solution exhibited the blue color. Triangular AgNPrs with average edge length of 87 nm were observed in TEM micrographs. These results indicated that the presence of H_2O_2 and starch in the premixed solution and their complemental functions were essential for the shape transformation to be possible. $AgNO_3$ and $NaBH_4$ were the Ag^+ source and reducing agent, respectively. As shown in TEM micrographs of Figure 4.6 A and B, soluble starch play the role of the stabilizer facilitating the formation of extremely small nanoparticles with narrow size distribution. H_2O_2 was the powerful oxidative etching agent that can disintegrate the AgNPs as observed from Figure 4.6 B and C that smaller AgNPs were formed when H_2O_2 was employed. The distinct point to be emphasized here is that when H_2O_2 and soluble starch were separately employed, shape transformation did not occur.
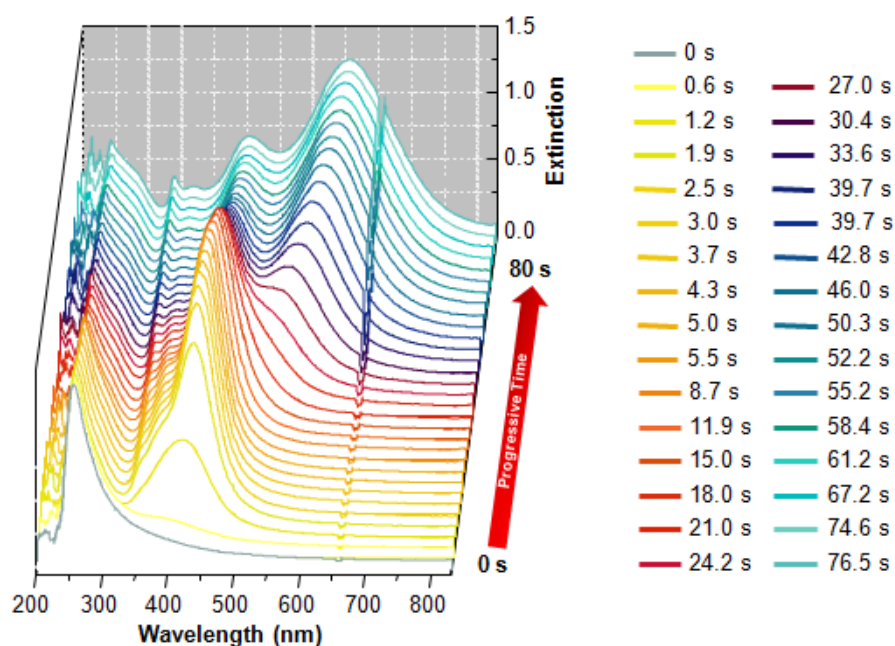
Figure 4.3   Time-resolved spectra of the shape transformation process. The spectra were recorded shortly before the nucleation burst.
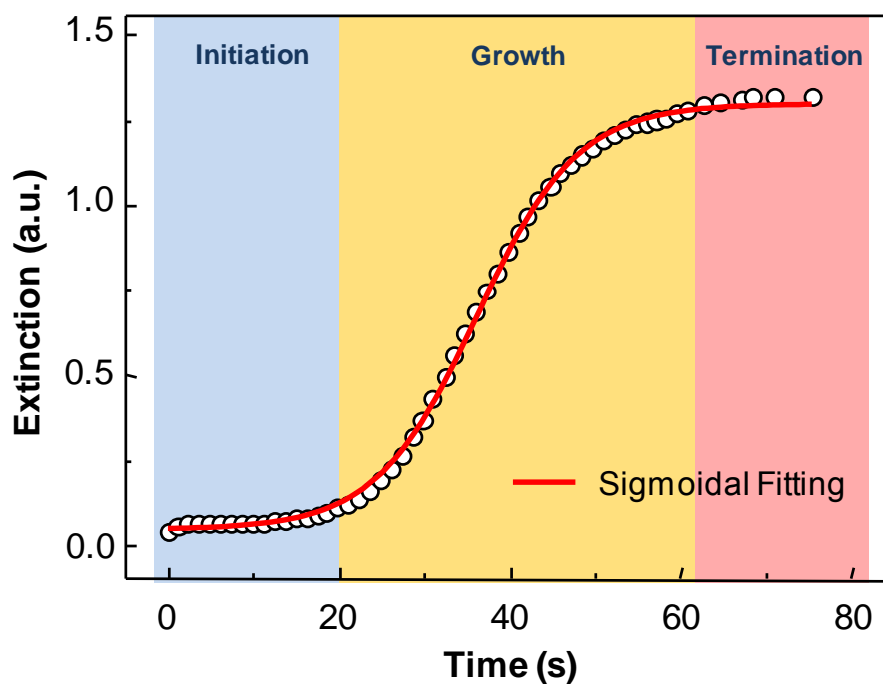
Figure 4.4   Time-dependent extinction intensity at 608 nm derived from the extinction spectra in Figure 4.3.
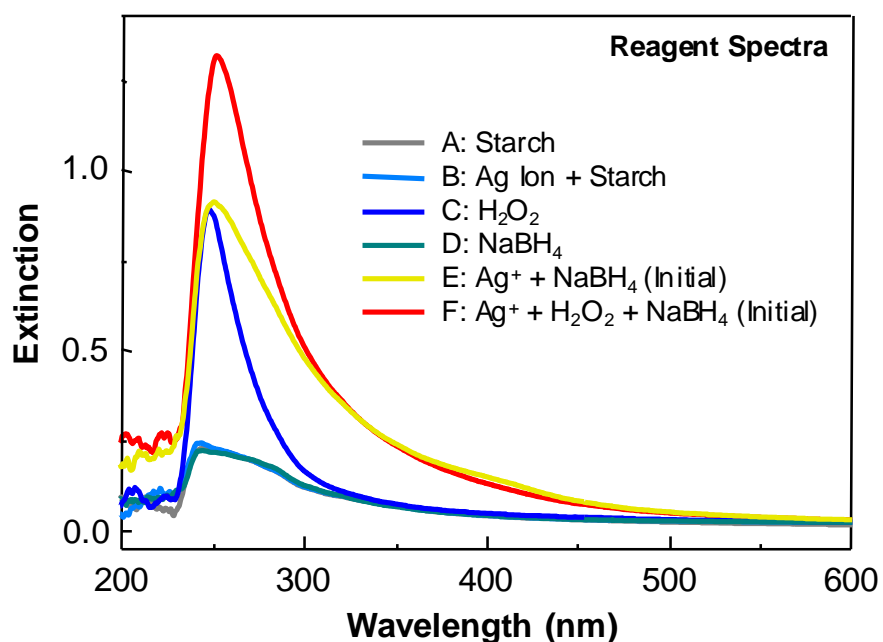
Figure 4.5   UV-visible spectra of chemical reagents employed in the shape transformation experiment.
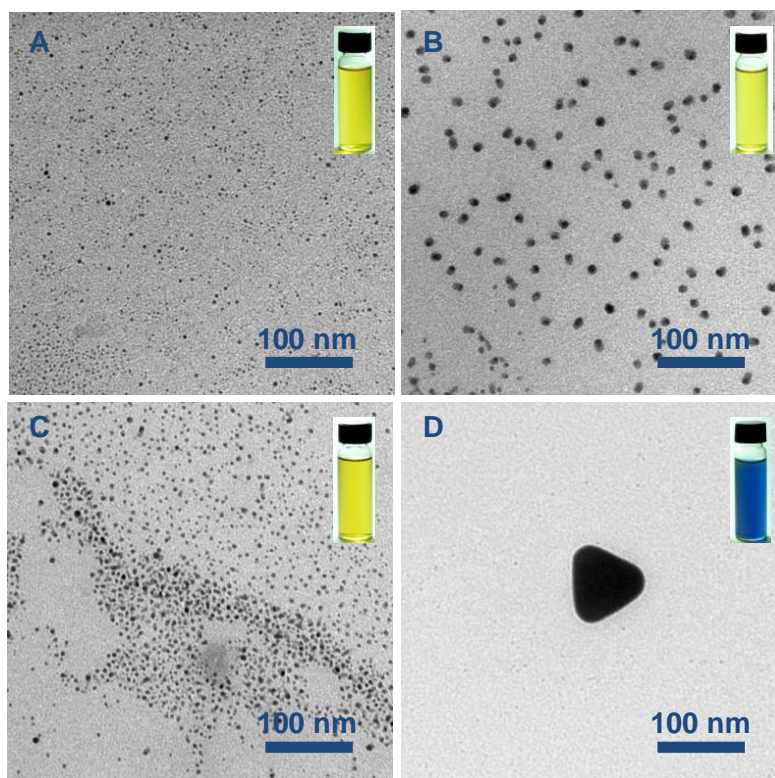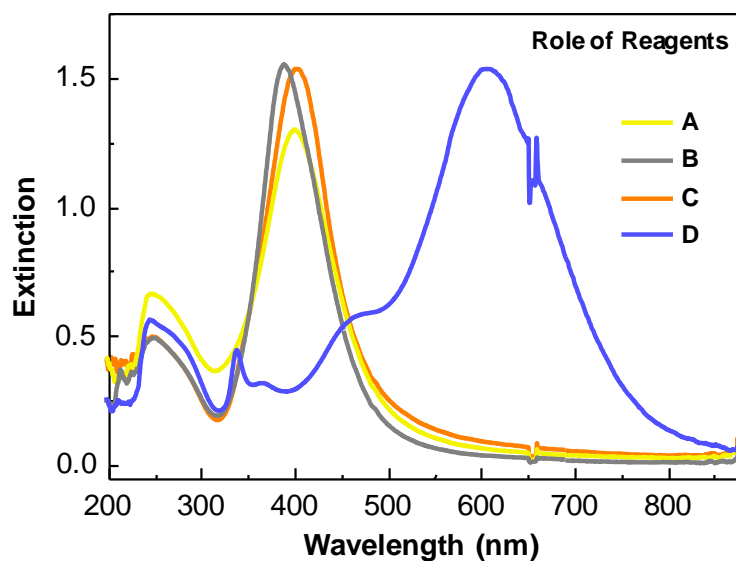
Figure 4.6   Plasmon extinction spectra, TEM micrographs, and digital photograph of the nanoparticle products from the shape transformation experiment when H_2O_2 was excluded (A), starch and H_2O_2 were excluded (B), and starch was excluded (C) from the standard condition, and when all reagents ($Ag^+ + H_2O_2 + Starch + NaBH_4$) were presented (D).

In order for gaining more insights to the shape transformation mechanism, the role of $NaBH_4$ was also investigated. Various molar ratio of $NaBH_4:AgNO_3$ from 4 to 25 were employed in the transformation experiments, while $AgNO_3$, the molar ratio of $H_2O_2:AgNO_3$, soluble starch concentration, and total volume of the synthesis were constrained at 0.139 mM, 250, 2 % (w/v), and 40 mL, respectively. The results are shown in Figure 4.7. When $NaBH_4:AgNO_3$ was less than 5, there were no observable shape transformation occurred. In addition, the final solution remained transparent. The formation of nanoparticles species were initially observed when $NaBH_4:AgNO_3$ were equal to 5.0. At $NaBH_4:AgNO_3$ of 5.56, there were the extinction peak at 434 nm and shoulder peak at 377 and 348 nm displayed in the extinction spectra, indicating the initial formation of AgNPrs species. The formation of planar anisotropic nanostructures became dominant when $NaBH_4:AgNO_3$ increased from 6.25 to 7.14. The solution color changed from yellow to green and blue, respectively, in concomitant with the increasing in IPDPR intensity of AgNPrs at 608 nm. The IPQPR and OPQPR peaks of AgNPrs also gradually developed. However, excess $NaBH_4$ seemed to suppress the AgNPrs formation. The extinction intensity at 608 nm was gradually reduced and the final solution colors were "stepped back" to the yellow brown color when $NaBH_4:AgNO_3$ increased from 7.14 to 25. In addition, IPDPR, IPQPR, and OPQPR peaks of AgNPrs were totally disappeared when $NaBH_4:AgNO_3$ was equal to 25. Only broad extinction spectrum with peak maximum at 432 nm characteristics to large spherical AgNPrs was observed. These observations suggested that $NaBH_4$ played the role more than a simple electron source. Its optimal concentration also determined the successful and completeness of the shape transformation from AgNSs to AgNPrs. One thing to be noted here is that the shape transformation experiments were performed when both the oxidizing species as H_2O_2 and reducing species as $NaBH_4$ were simultaneously presented. Therefore, both species might be consumed overtime by reacting with each other. We confirmed this by mixing $NaBH_4$ and H_2O_2 in the soluble starch solution before addition of $AgNO_3$ to see that whether there were residual $NaBH_4$ presented in the growth solution or not. When $AgNO_3$ was injected after 30 min of incubation, there were no observable LSPR peaks in the UV-visible spectra indicating the formation of Ag nanoparticle species (Figure 4.8 H). Only the intense peak of H_2O_2 at 250 nm remained.
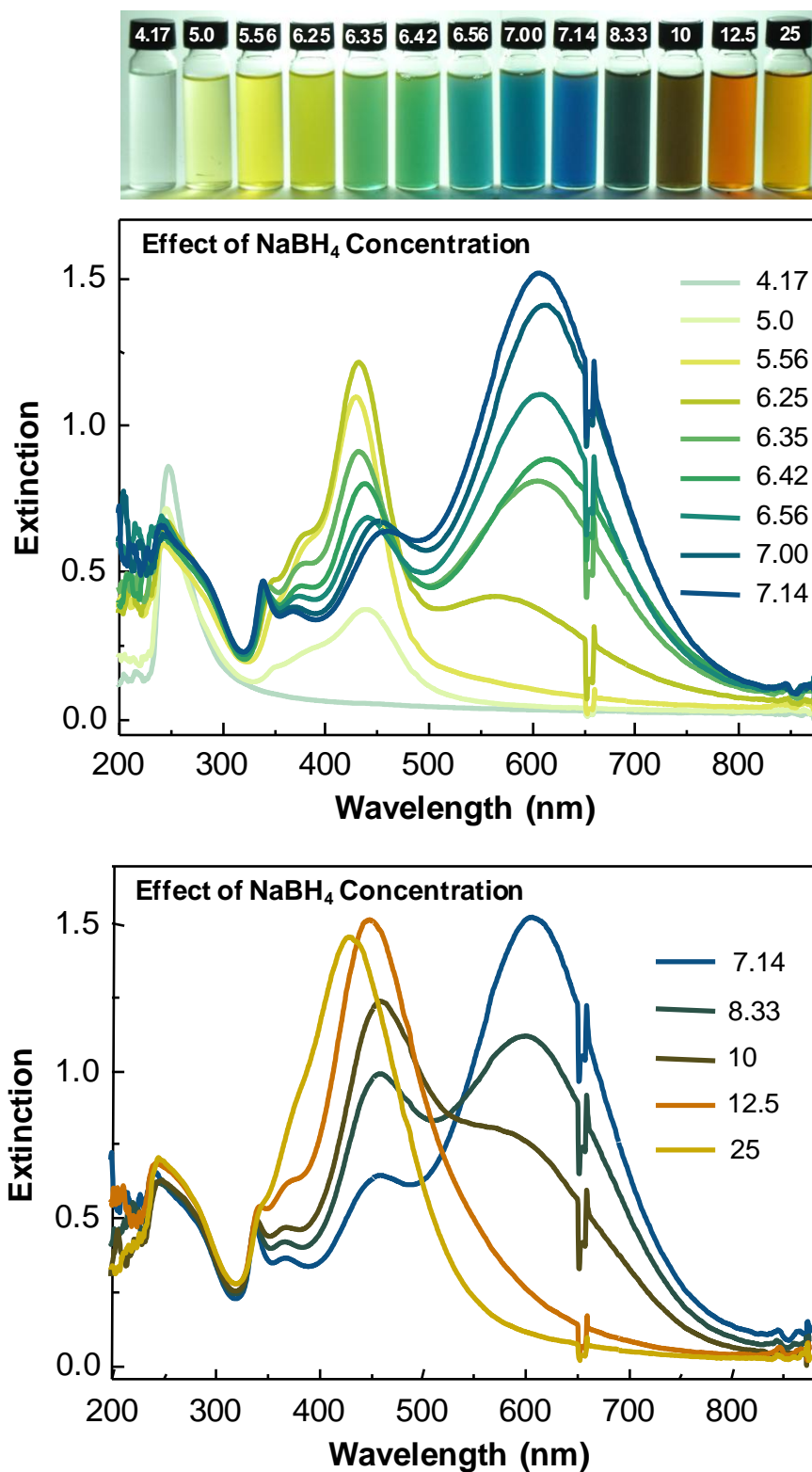
Figure 4.7   Effect of NaBH$_4$ on the shape transformation reaction. digital images and plasmon extinction spectra are corresponded to the molar ratio of NaBH$_4$:AgNO$_3$ employed in the experiment.
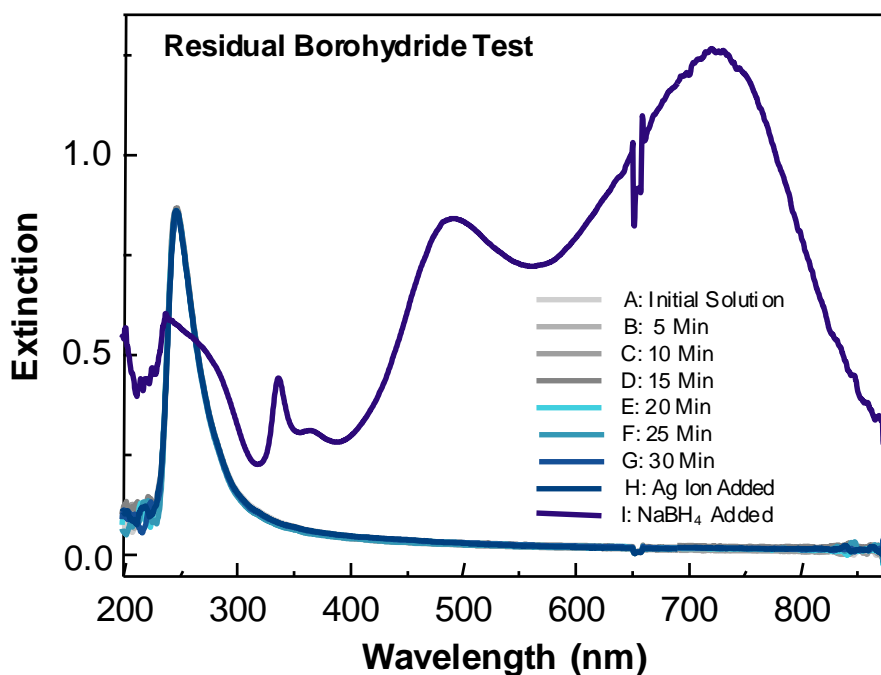
Figure 4.8   Experimental verification for the presence of NaBH$_4$ in the growth solution.

These results suggested that NaBH$_4$ was consumed overtime by H$_2$O$_2$. However, when additional NaBH$_4$ was added to the test solution, the LSPR peaks of AgNPrs i.e. 729 nm (IPDPR), 493 nm (IPQPR), and 338 nm (OPQPR) were again observed. The reduction in peak intensity at 250 nm also indicated that H$_2$O$_2$ was consumed in the transformation process. The persistent presence of H$_2$O$_2$ after the complete consumption of NaBH$_4$ suggested that the shape transformation occurred in the oxidizing environment. The atomic dissolution and resorption process occur during the growth of nanoprisms [107]. When insufficient amount of NaBH$_4$ was employed, incomplete or no shape transformation was observed. The atomic dissolution of metallic Ag species i.e. monomeric Ag atom or Ag nanoparticles species to Ag$^+$ by oxidative etching of H$_2$O$_2$ was prevailed, while the resorption process was suppressed. Therefore, we only observed the collapse of the nanostructures as reflected in the resulted transparent solution, or the incomplete shape transformation due to the lack of electron source for the atomic resorption process. These suggested that in addition to conventional reducing function, NaBH$_4$ also acted as the "protecting agent" preserving the formed metallic Ag species required for the prism growth. However,

when excess $NaBH_4$ was presented, the shape transformation was also suppressed. Here, the atomic resorption process was enhanced due to the excess electrons available in the system. The structures of metallic Ag species cannot be modified through the oxidative etching process by H_2O_2 since the etched Ag^+ was immediately reduced to Ag and resorped back to its original structures. In an extreme case, only isotropic characteristics of AgNSs were exhibited in the extinction spectra when excess $NaBH_4$ was employed (Figure 4.7 at $NaBH_4$:$AgNO_3$ = 25). These implied that the structural modification of initially formed metallic Ag by H_2O_2 through the oxidative etching was also required in order for preparing the appropriate nanostructures for the further growth into AgNPrs. Therefore, the key for successful chemical shape transformation is to modulate the oxidizing power of H_2O_2 and reducing power $NaBH_4$ so that they are cooperated well in constructions of AgNPrs without interfering each other.

From the above discussion, we can now summarize the key factors for performing the successful shape transformation experiment as follows:

☑ Extremely small nanoparticles (diameter < 5 nm) should be presented initially in the transformation process since they exhibited the relatively higher size-dependent instability compared to larger nanoparticles [25, 51]. Therefore, they will be more susceptible to be structurally modified by oxidative etching of H_2O_2. Utilizing soluble starch as stabilizer in the growth solution can facilitate the formation of these extremely small nanoparticles.

☑ Atomic dissolution of metallic Ag by the oxidative etching of H_2O_2 had to be preferentially occurred before the reducing action of $NaBH_4$ in order for modifying the metallic Ag species to the appropriate crystal structures before subsequent growth into AgNPrs. This can be accomplished by using much higher amount of H_2O_2 in comparison to $NaBH_4$. Specifically, for our shape transformation experiment, the mole ratio of H_2O_2:$AgNO_3$, $NaBH_4$:$AgNO_3$, and H_2O_2:$NaBH_4$, were 250, 7.14, and 35, respectively.

☑ The reducing function of $NaBH_4$ should be cooperated with the oxidizing action of H_2O_2. Sufficient amount of $NaBH_4$ had to be employed for complete reduction of Ag^+ presented in the growth solution. Meanwhile, it should not

suppress the oxidizing role of H_2O_2 so that atomic dissolution-desorption can be continued during the prism growth process.

The proposed shape transformation mechanism is depicted in Figure 4.9. When $NaBH_4$ was injected into the premixed solution, Ag^+ was preferentially reduced as described by chemical equation 4.1 [108].

$$2AgNO_3 + 2NaBH_4 + 6H_2O \rightarrow 2Ag + 2NaNO_3 + 2H_3BO_3 + 7H_2 \qquad (4.1)$$
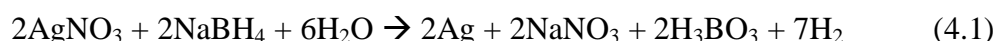
The formed metallic Ag can be oxidatively etched by H_2O_2:

$$2Ag + H_2O_2 + 2H^+ \rightarrow 2Ag^+ + 2H_2O \ (\Delta E^0 = + 0.964 \text{ V}) \qquad (4.2)$$
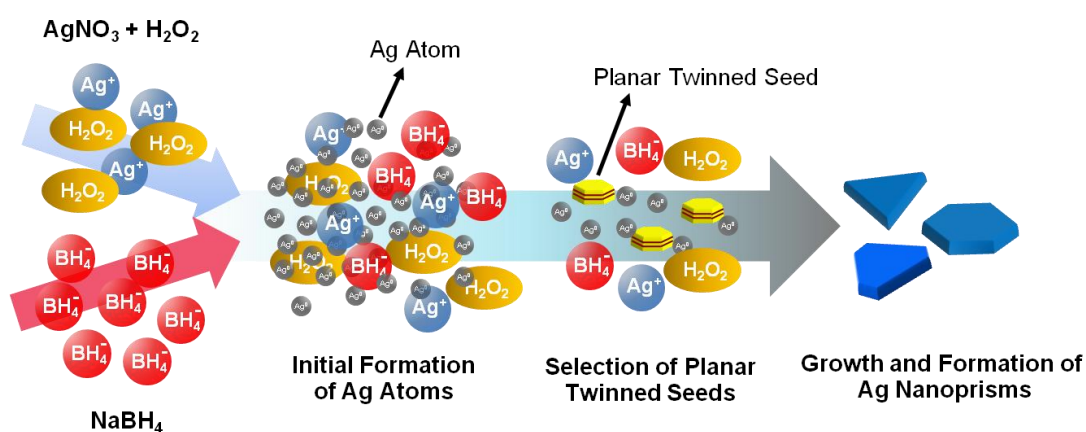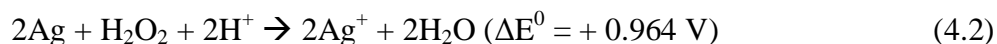
Figure 4.9   The proposed shape transformation mechanism.

The atomic dissolution (Eq. 4.2), re-reduction of etched Ag+ (Eq. 4.1) and atomic resorption onto metallic Ag species were repeatedly occurred before the initial nucleation burst. The result from this cyclic process was the seeds with the highest relative stability. From the previous reports, only seeds with planar twinned structure were survived during the seed selection process [52–53]. The planar twinned seeds subsequently acted as the nucleation sites for the Ag atom addition of during the nanoprism growth process. In the nanoprism growth process, the oxidative etching action of H_2O_2 still played the role by solubilizing the nanostructures with relatively low stability. Spherical nanostructures were relatively more labile than the plate-like

nanostructures in oxidizing environment [53]. The etched Ag^+ was re-reduced by $NaBH_4$ and underwent anisotropic atomic resorption on the planar twinned nanostructures until the exhaustion of $NaBH_4$, yielding the final AgNPrs.

We also explore the feasibility for utilizing the developed shape conversion system in tuning the optical properties of AgNPrs. The IPDPR of AgNPrs can be selectively tuned in the range from 425–750 nm by optimizing the molar ratio of H_2O_2:$AgNO_3$ (Figure 4.10 and Table 4.1). In contrast to the previous observations [52–53], we also had to optimize the concentration of $NaBH_4$ in corresponding to each molar ratio of H_2O_2:$AgNO_3$ for obtaining the desired IPDPR positions of AgNPrs. IPDPR position and experimental conditions for each experiment is summarized in Table 4.1.
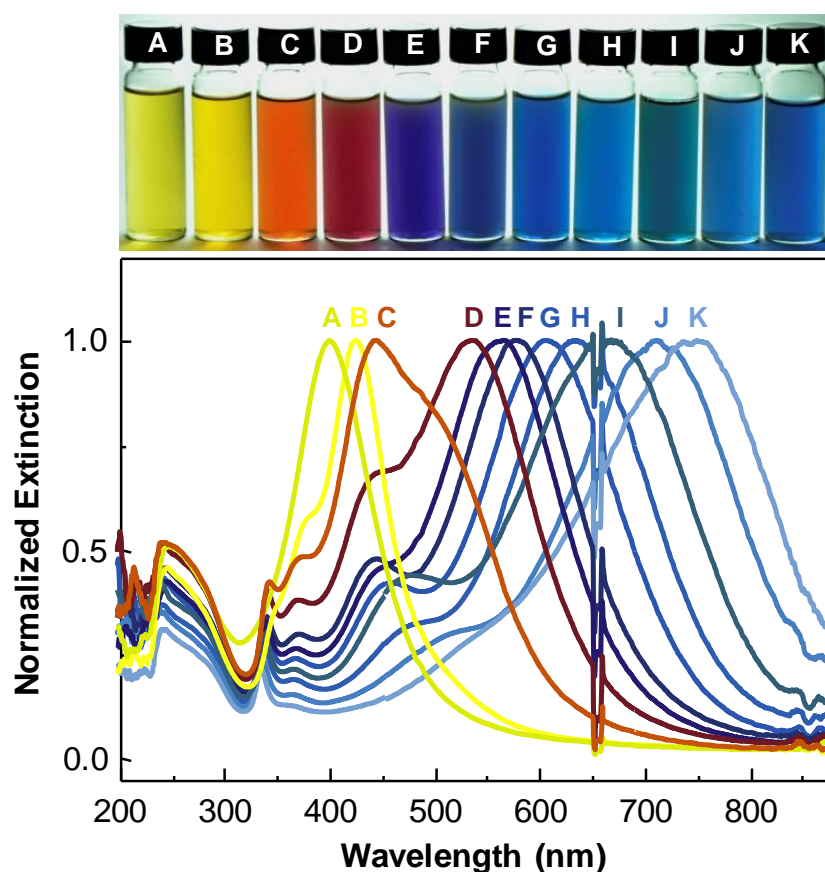
Figure 4.10   Plasmon extinction spectra and digital images of the colloidal AgNPrs with various IPDPR peaks as synthesized by the developed procedure.

Table 4.1   The experimental conditions employed for the AgNPrs synthesis in Figure 4.10. AgNO$_3$ concentration, soluble starch concentration, and total volume of the synthesis were constrained at 0.139 mM, 2% (w/v), and 40 mL, respectively.

Experiment No.	IPDPR Position (nm)	H$_2$O$_2$:AgNO$_3$ Mole Ratio	NaBH$_4$:AgNO$_3$ Mole Ratio
A	401	0	10
B	426	50	2.03
C	447	75	5.6
D	538	100	5.6
E	569	150	5.81
F	580	200	6.08
G	608	250	7.14
H	634	300	8.55
I	670	350	9.27
J	714	400	9.98
K	750	500	14.26

4.2 H$_2$O$_2$-Induced Shape Transformation of AgNSs to AgNPrs

We have demonstrated in the previous section that the shape transformation of AgNSs to AgNPrs can be accomplished without utilizing surface capping agents e.g. citrate or PVP. In addition, our developed system also exhibited the optical controllability of the obtained AgNPrs in the visible to near infrared region. However, high molar ratio of H$_2$O$_2$:AgNO$_3$ (at least 100) and NaBH$_4$:AgNO$_3$ (at least 5.6) had to be employed in order to obtain the high yield of AgNPrs with reliable IPDPR positions. Many interesting points arose for the improvement of the shape transformation system. The most important one should be "Is it possible to trigger the shape transformation and carry out the nanoprisms growth process utilizing only H$_2$O$_2$?"

First of all, it is well known that we can store Ag^+ with H_2O_2 infinitely without observing any change in the solution but only the decomposition of H_2O_2 to oxygen gases and water overtime. However, concentrated (30–90% (w/w)) H_2O_2 could undergo catalytic decomposition on various metals including Ag where metal ion could be released from the metal surface and colloidal metal particles were observed after the decomposition [66–68]. This evidence told us that H_2O_2 can modify the surface of metal through the oxidative etching function, and metallic particles can be formed separately from the original metal surface. The formation of metallic particles from released metal ions also implied the reducing capability of H_2O_2. Reducing function of H_2O_2 was previously addressed in many studies on fabricating of metal nanostructures [57–61]. Therefore, the first modification step was to shift the silver ion source from $AgNO_3$ to some other metallic Ag species that capable of catalyzing decomposition of H_2O_2. The next step to clarify was that can we control the released Ag^+ to be re-reduced back to Ag atom by H_2O_2 and anisotropically resorbed back to available Ag nanoparticles species so that the growth of nanostructure would be possible. Previously, polymer-capped AgNSs were employed as H_2O_2 sensor [81–82]. However, only the colloidal color diminution without a shape transformation was observed. Attenuation of plasmon extinction was mainly due to the oxidative dissolution of AgNSs to Ag^+ by H_2O_2. We anticipate that because of low concentration (less than 0.5 mM) of AgNSs employed in the sensing system in order to obtain the mathematically meaningful LSPR intensity for subsequent calibration test preventing them from the observing shape transformation phenomena.

Therefore, we started our modified shape transformation experiment with the synthesis of starch-stabilized AgNSs for utilizing as silver ion source instead of $AgNO_3$. The initial concentration of AgNSs (in term of total Ag^+ content) was increased to from 0.139 mM to 1.854 mM (approximately 14 times) to test our hypotheses. The average particle diameter was around 6 nm (Figure 4.11 B), satisfying the extremely small particle criteria as described in the preliminary observations. The shape transformation reaction was initiated simply by adding 30% H_2O_2 into the colloidal AgNSs. The volume of the colloidal AgNSs increased from 40 mL to 200 mL in order for investigating a scaling up of the process. Due to the fast

and violent reaction between H_2O_2 and metallic Ag, we employed the high performance disperser as mechanical agitator in order to obtain uniform H_2O_2.
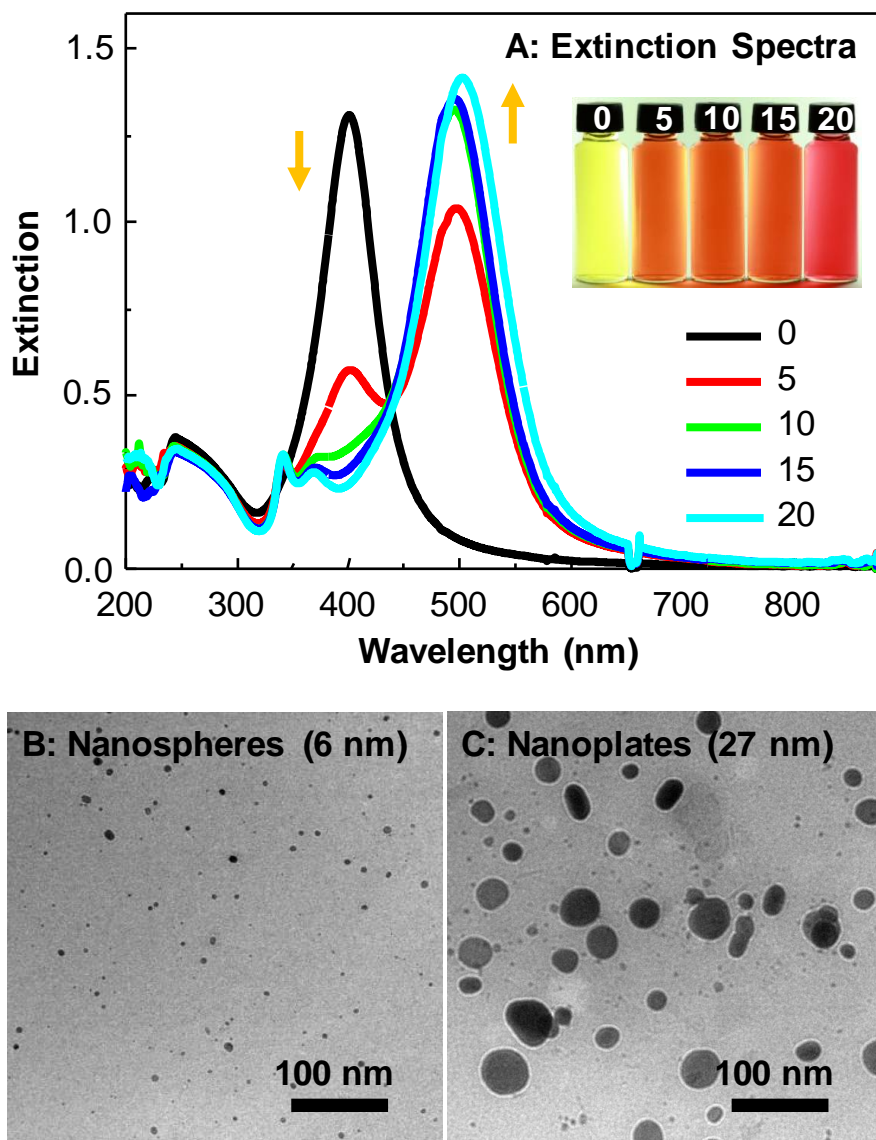
Figure 4.11   Preliminary observations on the shape transformation of AgNSs to AgNPrs utilizing H_2O_2. Initial AgNSs concentration was 1.834 mM. The molar ratio of H_2O_2:AgNSs (R) was varied from 0 (AgNSs) to 20. H_2O_2 injection rate was 10.09 mL/min. The disperser speed was set at 15k rounds per minute (rpm). Plasmon extinction spectra (A), TEM micrographs of silver nanospheres (B) and circular nanoplates (C) are shown. The digital photograph of the colloidal suspensions at various R is shown as inset.

To our surprise, we observed the color change of the colloidal suspension from yellow to pink and red, respectively, immediately after the injection of H_2O_2 into AgNSs colloid. This color change is directly associated with the shape evolution of metallic Ag species. When the molar ratio of H_2O_2:AgNSs increases from 5 to 20, the intensity of DPR peak of AgNSs at 400 nm is attenuated in concomitant with the increment in intensity of emerging peak at 500 nm as observed in the plasmon extinction spectra (Figure 4.11 A). Another less intense peak at 342 nm is also developed. Circular nanoplates with average bisector length of 27 nm were formed as observed in the TEM micrograph (Figure 4.11 C). Therefore, the developed peaks at 500 nm and 342 are IPDPR and OPQPR peaks of formed nanoplates. Interestingly, H_2O_2 can induce the direct transformation of AgNSs to AgNPrs as the isosbestic point centered at 342 is noticed.

When initial AgNSs concentration was increased to 3.71 mM (~ 2 times higher), more interesting phenomena were observed. Figure 4.12 displays the digital photograph of the colloids, the corresponding extinction spectra, and representative TEM micrographs of AgNSs and AgNPrs with different molar ratios of H_2O_2:AgNSs (R) from 1 to 50. Upon an injection of H_2O_2 into the AgNSs colloid, the color of the colloid instantaneously changed from yellow to red, pink, violet, and blue depending on the molar ratio R (Figure 4.12 A). The color and spectral changes (Figures 4.12 A and B) directly associate with the morphological transformation of the silver nanoparticles. Initially, when R = 1, there was no observable change in plasmon extinction spectrum. A tailing at 450–500 nm emerged when R was increased to 2.5 indicating the partial aggregation of oxidatively etched AgNSs (Figure 4.12 D). At this stage, the signature of the in-plane dipole plasmon resonance (IPDPR) and the out-of-plane quadrupole plasmon resonance (OPQPR) of AgNPrs were not observed (Figure 4.13 and Table 4.2). This indicates that AgNSs were not yet transformed to anisotropic nanostructures. The color change from yellow to red was observed when R = 5. AgNPrs with circular cross section were formed as indicated by the corresponding TEM micrograph (Figure 4.12 E). Two new peaks centered at 339 nm and 512 nm are attributed to the OPQPR and IPDPR of the circular AgNPrs, respectively.
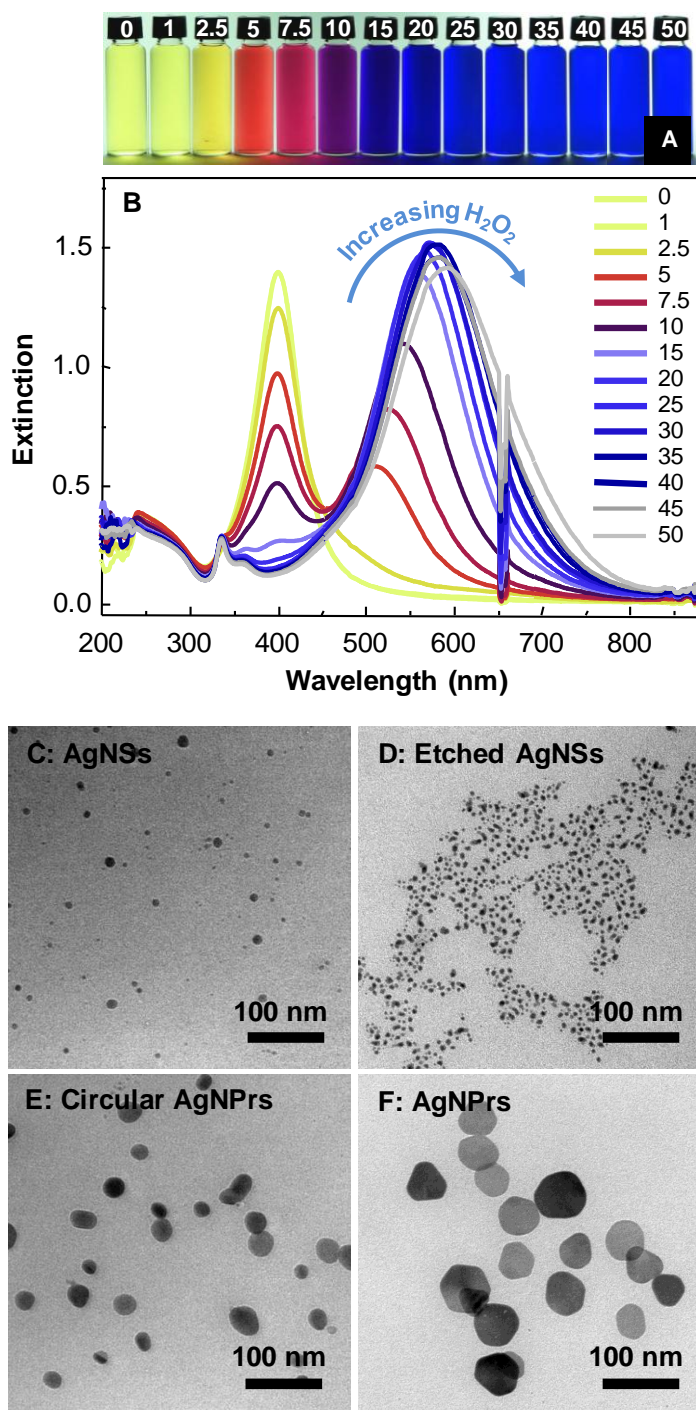
Figure 4.12 Digital photograph of AgNSs colloids (A) and the corresponding plasmon extinction spectra (B) before (R=0) and after addition of H_2O_2 (R = 1–50). TEM micrographs of AgNSs (C; R = 0), initially etched AgNSs (D; R = 2.5), circular AgNPrs (E; R = 5), and AgNPrs (F; R = 1:30) are shown as representatives of structural development upon an addition of H_2O_2.
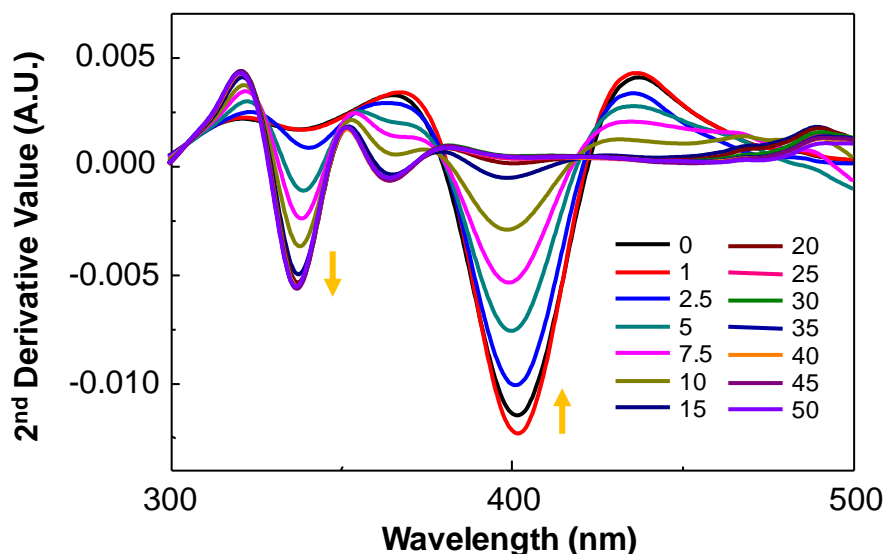
Figure 4.13 2nd Derivative spectra of the plasmon extinction spectra shown in Figure 4.12. The numbers indicate the molar ratio of H_2O_2:AgNSs (R) employed for the shape transformation process. The dipole plasmon resonance (DPR) of AgNSs at ~400 nm decrease while the out-of-plane quadrupole plasmon resonance (QPQPR) near ~340 nm increase as the mole ratio R increase.

The AgNPrs enlarged as R was increased to 30. The morphologies of AgNPrs with R = 30 were circular disk, truncated triangle, and hexagon (Figure 4.12 F). The redshift of IPDPR from 512 (R = 5) to 575 nm (R = 30) indicates that AgNPrs are laterally expanded as evidenced in the increasing of edge length from 27.46 ± 8.38 nm to 47.49 ± 10.01 nm, respectively (Figure 4.14).

A slight blueshift of OPQPR from 339.07 to 337.25 nm indicates an increment of the aspect ratio (bisector length/thickness) of AgNPrs. The change in dipole plasmon resonance (DPR) peak of initial AgNSs was also investigated. The DPR peak of the AgNSs was slightly blueshifted from 401.85 nm to 398.99 nm when R was increased from 1 to 15. Additionally, the reduction of DPR intensity of AgNSs was accompanied by the increment of IPDPR intensity of AgNPrs when R was increased from 1 to 30. These indicate that starting AgNSs are oxidatively etched by H_2O_2. The etched AgNSs and solubilized Ag^+ from the etching process are instantly utilized for the formation of AgNPrs. An increasing extinction and the redshift of IPDPR together

with a disappearance of the DPR at 402 nm indicate that enlargement of AgNPrs dimensions and increment in AgNPrs population are accomplished with the expenses of the AgNSs (Figure 4.15). The direct transformation of AgNSs to AgNPrs is corroborated by chemometric study based on multivariate curve resolution–alternative least squares (MCR–ALS) analysis [89]. The complete disappearance of DPR peak of AgNSs at R of 30 implies that AgNSs are totally consumed in the process. An absence of a hump peak around 420–440 nm suggests that there are no other nonspherical nanoparticles or residual small-diameter nanoparticles in the final colloid [30]. When R is increased from 35 to 50, a slight reduction in IPDPR intensity with a redshift from 581 to 594 nm indicates a formation of larger AgNPrs with an expense of smaller AgNPrs through the Ostwald ripening process [89].

Table 4.2   Peak positions of DPR of AgNSs, IPDPR and OPQPR of AgNPrs of the plasmon resonance spectra shown in Figure 4.12. R indicates the molar ratio of H_2O_2:AgNSs employed for the shape transformation.

R	OPQPR of AgNPrs	IPDPR of AgNPrs	DPR of AgNSs
0	Not Observed	Not Observed	401.85
1	Not Observed	Not Observed	401.85
2.5	340.88	Not Observed	401.14
5	339.07	511.61	400.06
7.5	338.70	523.06	339.35
10	337.98	541.19	398.99
15	337.61	559.72	398.99
20	337.61	570.14	Not Observed
25	337.25	573.55	Not Observed
30	337.25	574.57	Not Observed
35	337.25	581.11	Not Observed
40	337.25	582.72	Not Observed
45	337.25	584.08	Not Observed
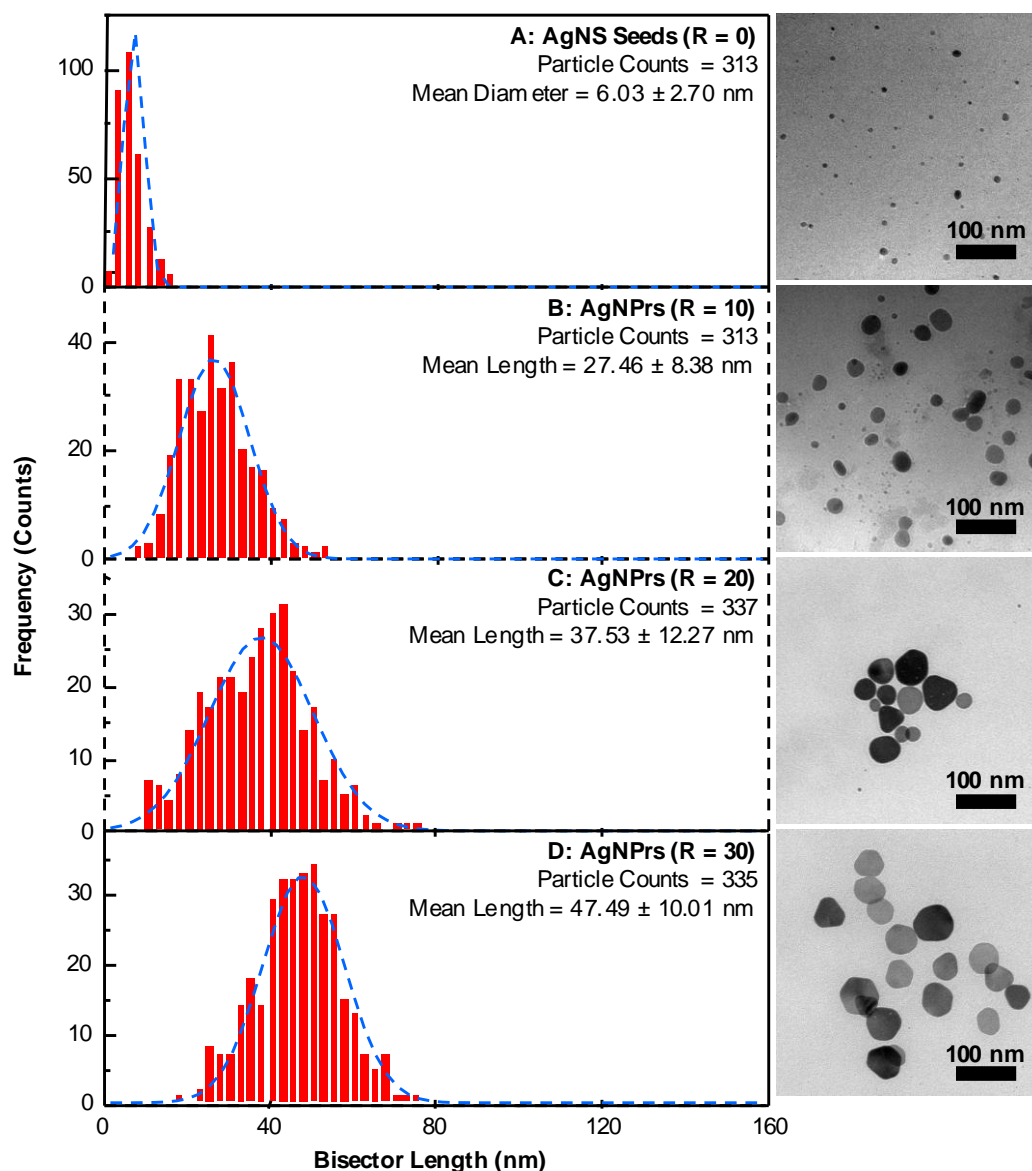
Figure 4.14   Histograms show particle size distribution of the original silver nanospheres (AgNSs) (A) and the corresponding silver nanoprisms (AgNPrs) synthesized by the H_2O_2-triggered shape transformation with the mole ratio of H_2O_2:AgNSs (R) of 10 (B), 20 (C), and 30 (D). Each histogram was calculated from at least 300 particles in non-overlapping TEM images with sufficiently clear and adequate magnifications. Examples of the employed TEM images are shown. The particles show normal size distribution as indicated by the fitted Gaussian curves (dotted lines).
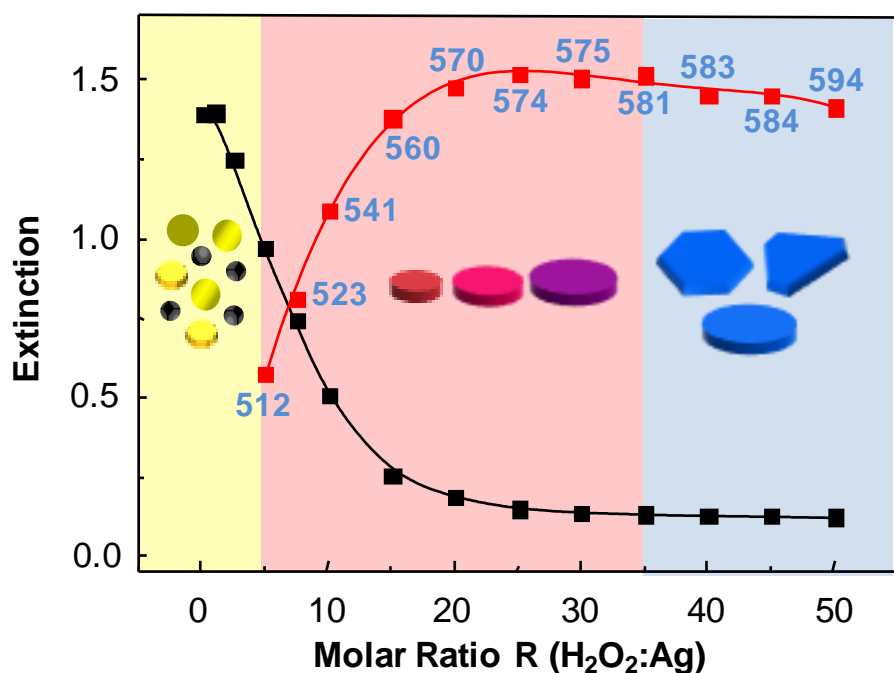
Figure 4.15   DPR Peak intensity of AgNSs (■) and IPDPR of AgNPrs (■) at the corresponding R. Number at each point indicates IPDPR peak position. AgNSs (●), planar twinned seeds (●), re-reduced Ag atom (●), circular AgNPrs (●●●●), and hexagonal and truncated triangular AgNPrs (●▱) are schematically drawn as insets to demonstrate the morphological evolution.

4.3 Role of the Reagents in the Shape Transformation Process and Proposed Morphological Transformation Mechanisms

The observed results in section 4.2 suggested that H_2O_2 can trigger and promote the AgNSs-to-AgNPrs shape transformation without additional reducing agents or capping molecules. In order to gain an insight understanding of the shape transformation mechanism, roles of key chemical reagents and experimental parameters were systematically investigated.

4.3.1 The Role of Soluble Starch

Figure 4.16 shows ATR FT-IR spectra of virgin starch, starch-stabilized AgNSs,

and starch-stabilized AgNPrs. The intense absorption in the region of 1200–900 cm^{-1} is assigned to glycosidic linkage of starch bridge β C^1–O–C^4 (i.e., C–O, C–C stretching at 1163 cm^{-1}, C–O–H bending at 1094 cm^{-1}, and C^1–H bending at 1067 cm^{-1}) and skeleton vibration of α-1,4 glycosidic linkage at 930 cm^{-1} [110]. The absorption at 3000–2800 cm^{-1} and 3600–3100 cm^{-1} are assigned to C–H and O–H stretching, respectively. The perfect superimposition of the spectra in Figure 4.16 suggests that functional groups of starch were not changed during the AgNSs synthesis and AgNSs-to-AgNPrs transformation. Under the employed condition, starch did not show a sign of degradation such as a development of the absorption of carbonyl groups and a change of the absorption of the glycosidic linkage [110–111] (Figure 4.17). To make soluble starch an efficient reducing agent, the starch must undergo (i) acidic hydrolysis and (ii) alkaline treatment in order to induce a formation of degradation intermediates containing alpha-hydroxy ketone or aldehyde functionality. The operation must be performed under a hot alkaline solution (pH 12-14, 80-100 ^{o}C) [110–111]. The sign of starch degradation is evident via the distinct development of the absorption centered at 1591 and 1354 cm^{-1} (as indicated by the pink and blue bands, respectively) assigned to asymmetric and symmetric vibration of the carboxylate (-COO$^-$) group. Insignificant changes of the absorptions at 1200-900 cm^{-1} of the glycosidic linkage (bridge β C^1–O–C^4 stretching) and the absorption at 939 cm^{-1} of the skeleton vibration of α-1,4 glycosidic linkage (C–O–C) suggest that the degradation is partial. The absorption at 1634 cm^{-1} is assigned to the water absorption in the amorphous starch [112].

To investigate the reducing capability of starch, we did add AgNO$_3$ into the colloid of AgNSs (Figure 4.18). No change was observed even after 30 min incubation. This observation indicates that the as-synthesized starch-stabilized AgNSs colloid with a mild alkaline condition (pH 8-9) is absent of residual NaBH$_4$ reducing agent while starch does not reduce the added Ag$^+$. However, when NaBH$_4$ was added, the increased DPR extinction at ~400 nm indicates a formation of additional AgNSs derived from the added AgNO$_3$. The observed phenomena confirm that starch is not a reducing species in the shape transformation process. Starch functions only as a steric stabilizer that efficiently prevents aggregation of AgNSs and AgNPrs. In addition,

starch functions also as an efficient stabilizer facilitating the formation of small AgNSs with an average diameter less than 10 nm (Figure 4.19).
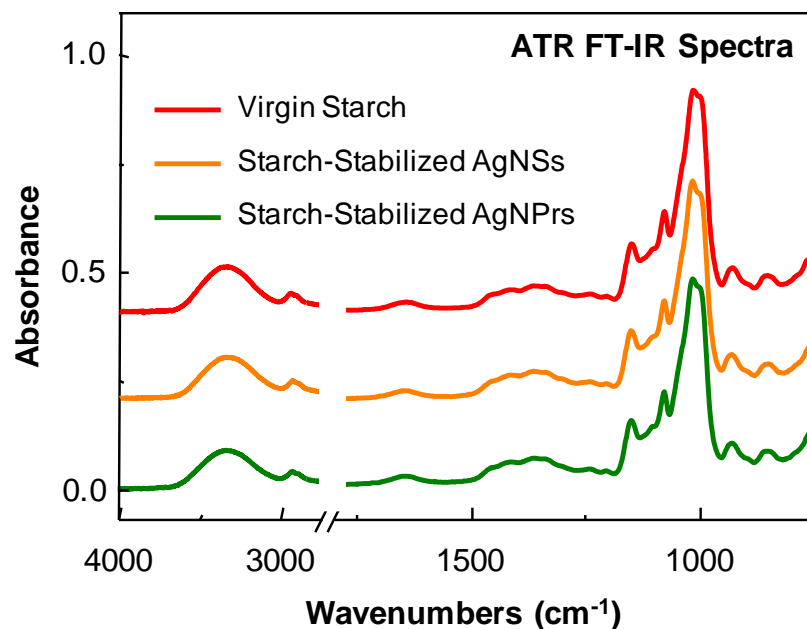
Figure 4.16   ATR FT-IR spectra of virgin starch, starch-stabilized AgNSs, and starch-stabilized AgNPrs.
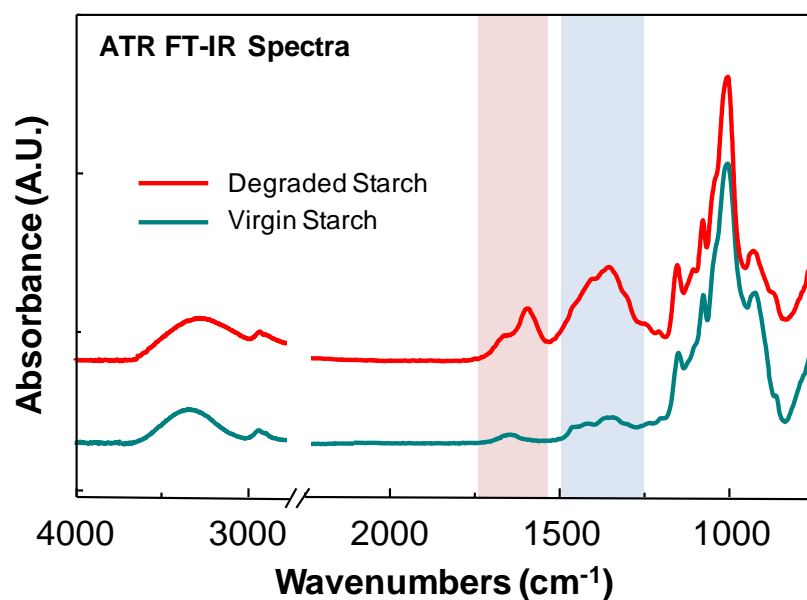
Figure 4.17   Comparison of ATR FT-IR spectra of virgin starch and degraded starch. The partially degraded starch was prepared by subjecting the virgin starch to a consecutive acidic/alkaline treatment.
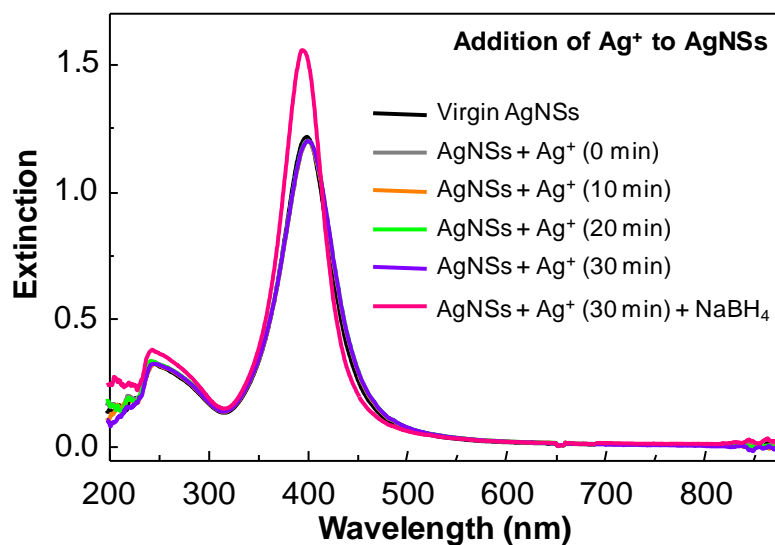
Figure 4.18   Plasmon extinction spectra of 3.52 mM AgNSs incubated with 0.46 mM Ag^+. The colloid incubated for 30 min shows no sign of change. However, after an addition of a trace amount of $NaBH_4$, a sudden increment of the DPR at ~400 nm of AgNSs is observed.
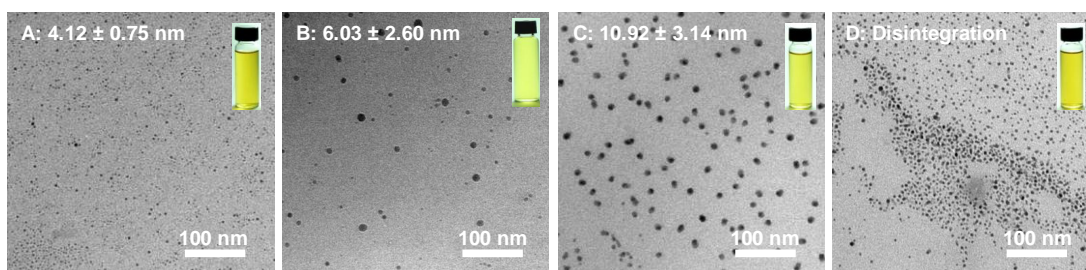
Figure 4.19   TEM micrographs of AgNSs synthesized by reducing $AgNO_3$ solution with aqueous $NaBH_4$ with the presence of 2% (w/v) soluble starch with $[AgNO_3]$ of 0.14 mM (A) and 3.71 mM (B). Larger AgNSs with a broader size distribution were obtained in the absence of starch (C) with $[AgNO_3]$ of 0.14 mM. When a 117 μL of 30% H_2O_2 was injected into a 40 mL colloid of the non-stabilized AgNSs (C), only the disintegration of metallic AgNSs was attained without any shape transformation (D). The shape transformation of starch-stabilized AgNSs can always be triggered by an addition of H_2O_2 as shown in Figure 4.12.

Since the shape transformation was performed in a weak alkaline solution (pH 8-9), the formation of Ag_2O was investigated. In order to examine whether Ag_2O existed in the shape transformation process or not, two type of reaction media i.e. 2% (w/v) soluble starch and DI water with pH 10 were prepared before the injection of Ag^+ having final concentration of 0.14 mM. The results are shown in Figure 4.20. Cloudy solution was observed only when DI water was used as the reaction medium. Although the solution is moderate alkaline of pH 10, starch can prohibit the formation of Ag_2O through the coordinated bonding of Ag^+ with ether oxygen and hydroxyl groups of the starch molecules via ion-dipole interactions [113] as a clear solution was observed after 60 s incubation. These phenomena suggest that Ag_2O does not exist in the shape transformation process as the oxidatively dissolved Ag^+ ions are strongly complexed with starch. The complex is strong enough to inhibit the formation of Ag_2O. As a consequence, Ag^+ is the electron receptor in our system.
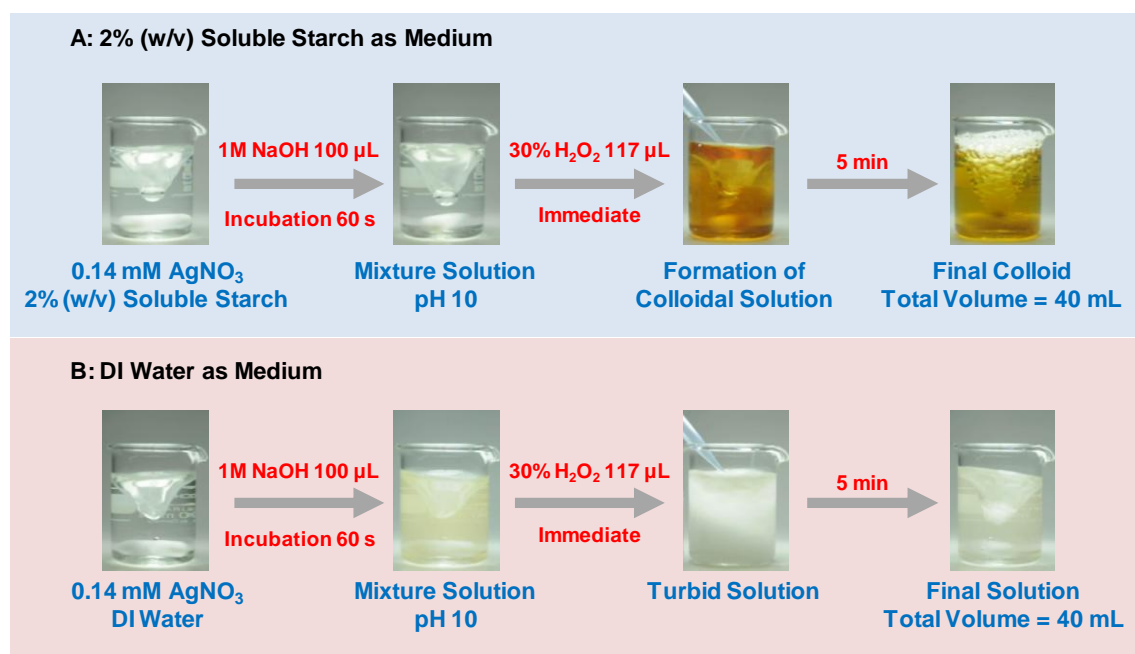
Figure 4.20   Experimental verification on the formation of Ag_2O in 2% (w/v) soluble starch (A) and DI water (B) at pH 10.

When H_2O_2 was added to the solution of soluble starch stabilized Ag^+, the orange-yellow color developed immediately. The plasmon extinction spectrum of that

yellow solution is shown in Figure 4.21. The characteristic DPR centered at 400 nm with the absorption at 220–320 nm of the interband transition suggests the formation of spherical silver nanoparticles. However, in the system without starch stabilizer, no DPR is observed in UV-visible spectra of Ag_2O solution as well as its product after an addition of H_2O_2. A large amount of gas bubbles observed during the reaction was due to the alkaline-catalyzed decomposition of H_2O_2 [71]. These observations also suggest that H_2O_2 is the sole reducing agent in the shape transformation process since the reduction by starch under the employed conditions does not occur.
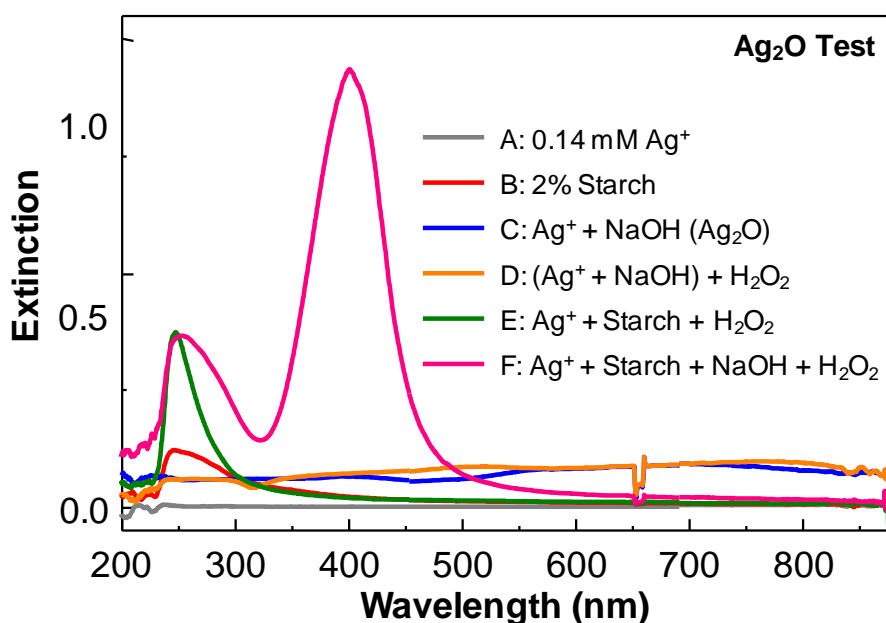
Figure 4.21 UV-visible spectra of Ag^+ (A), 2% (w/v) soluble starch (B), Ag_2O in DI water (C), Ag_2O + H_2O_2 in DI water (D), a mixture of Ag^+ and H_2O_2 in 2% (w/v) soluble starch solution at pH 7 (E), and yellow colloid from the reaction of Ag^+ and H_2O_2 in 2% (w/v) soluble starch at pH 10 (F).

4.3.2 The Role of H_2O_2

The principal reagent involved in the shape transformation experiment is H_2O_2. H_2O_2 was extensively employed as an oxidative etchant [51–54] for a selective dissolution of unstable facets [81] yielding seeds with planar twinned defects or

stacking faults parallel to {111} direction [5, 26, 83–84]. These seeds are necessary for the development to AgNPrs. Oxidative etching also played a role in determining final shape of nanocrystals by entirely destroying the energetically unfavorable seeds with multiply twinned defects [76–80], or sculpturing sharp corners/edges [56]. The reducing capability of H_2O_2 for metal nanostructure fabrications was addressed in several studies [57–61]. It is theoretically possible that H_2O_2 can function as both a facet selective etchant toward metallic Ag species and a reducing agent for ionic Ag species as expressed by the following equations:

H_2O_2 as an oxidizing agent [65–68, 73]:

$$Ag^+ + e^- \rightarrow Ag \ (E^0 = 0.7996 \text{ V}) \tag{4.3}$$

$$H_2O_2 + 2e^- \rightarrow 2HO^- \ (E^0 = 0.867 \text{ V}) \tag{4.4}$$

$$2Ag + H_2O_2 \rightarrow 2Ag^+ + 2HO^- \ (E^0 = 0.068 \text{ V}) \tag{4.5}$$
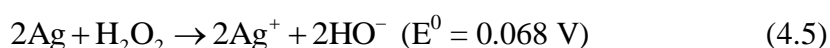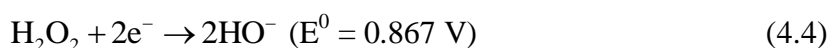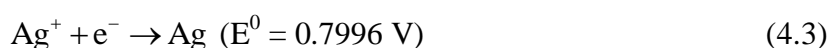
H_2O_2 as a reducing agent [73, 114]:

$$2H_2O + O_2 + 2e^- \rightarrow H_2O_2 + 2HO^- \ (E^0 = -0.146 \text{ V}) \tag{4.6}$$

$$H_2O_2 + 2HO^- + 2Ag^+ \rightarrow 2Ag + 2H_2O + O_2^- \ (E^0 = 0.947 \text{ V}) \tag{4.7}$$
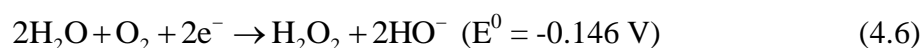
The positive values of the electrochemical cell potential in Eq. 4.5 and Eq. 4.7 suggest that both reactions can occur simultaneously.

To corroborate the idea that H_2O_2 plays the dual functions as the oxidative etchant and reducing agent, a shape transformation with an addition of extra $AgNO_3$ was performed (Figure 4.22). When 117 μL of 30% H_2O_2 was added to the Ag^+-spiked AgNSs, a greater extinction of IPDPR at 500 nm was achieved (i.e., compared to the operation on AgNSs without an additional Ag^+). The greater IPDPR at 500 nm due to a greater concentration of AgNPrs is attributed to the reduction of additional Ag^+ by H_2O_2. The added Ag^+ ions increase the concentration of metal ions necessary for the formation of silver atoms required for the development of AgNPrs. AgNSs

were etched by H_2O_2 as observed by the decrement of the DPR extinction at 400 nm. Interestingly, extents of the AgNSs etching of the two colloids are equivalent since the DPR extinctions at 400 nm are decreased by the same magnitude. This simple experiment clearly demonstrates the oxidation and reduction capabilities of H_2O_2 in the shape transformation process. H_2O_2 oxidatively etches AgNSs while it reduces Ag^+ to Ag atoms. The formation of AgNPrs from the dissolved Ag^+ is evident as the extinction at 400 nm decreases with a concomitant development of the extinction at 500 nm after an addition of H_2O_2.
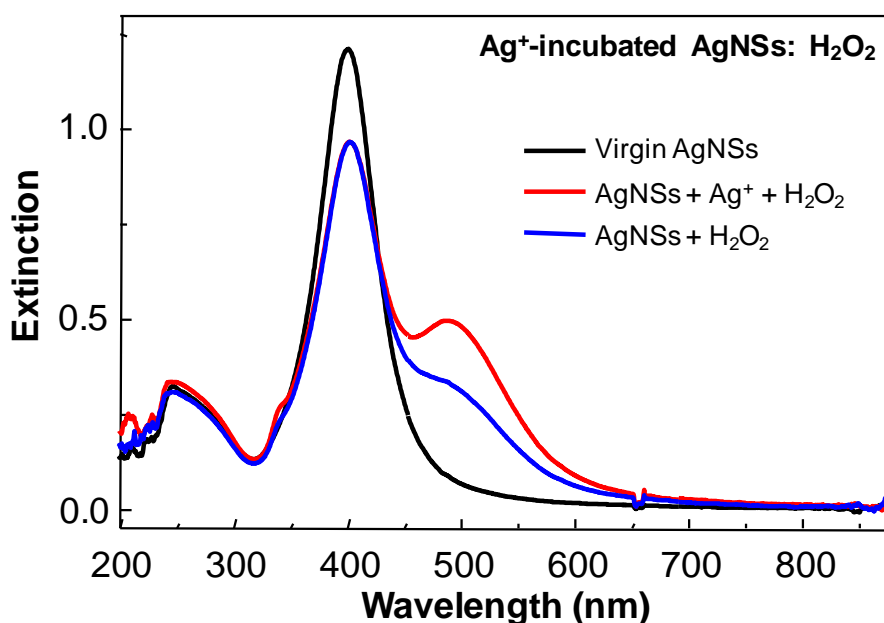
Figure 4.22   Plasmon extinction spectra of AgNSs, AgNSs + H_2O_2, and Ag^+-spiked AgNSs + H_2O_2. The systems with and without added Ag^+ show the same degree of etching of the original AgNSs. A greater number of AgNPrs was generating from the system with added Ag^+. The experimental parameters: AgNSs (3.52 mM, 38 mL); AgNO₃ (9.27 mM, 2 mL) or DI Water (2 mL); H_2O_2 (30% (w/w), 117 μL).

It has been shown by Kawazumi's paper [53] that nanoplates are more tolerant to the oxidative etching of H_2O_2 than nanospheres. In our case, when H_2O_2 was injected to the colloidal mixture (1:1 (v/v)) of AgNSs (DPR = 400 nm) and AgNPrs (IPDPR = 588 nm), H_2O_2 preferentially destroyed AgNSs while promoted the growth of AgNPrs

(Figure 4.23). DPR intensity of AgNSs is reduced indicating the oxidative dissolution of AgNSs. An increment in the IPDPR intensity of AgNPrs suggests an increase AgNPrs population. These observed phenomena are different from those shown in Kawazumi's paper [53] as we employed a relatively low concentration of H_2O_2. As a result, a complete dissolution of both AgNSs and AgNPrs was not observed However, the original AgNPrs were also etched as indicated by the blueshift of IPDPR from 588 nm to 570 nm.
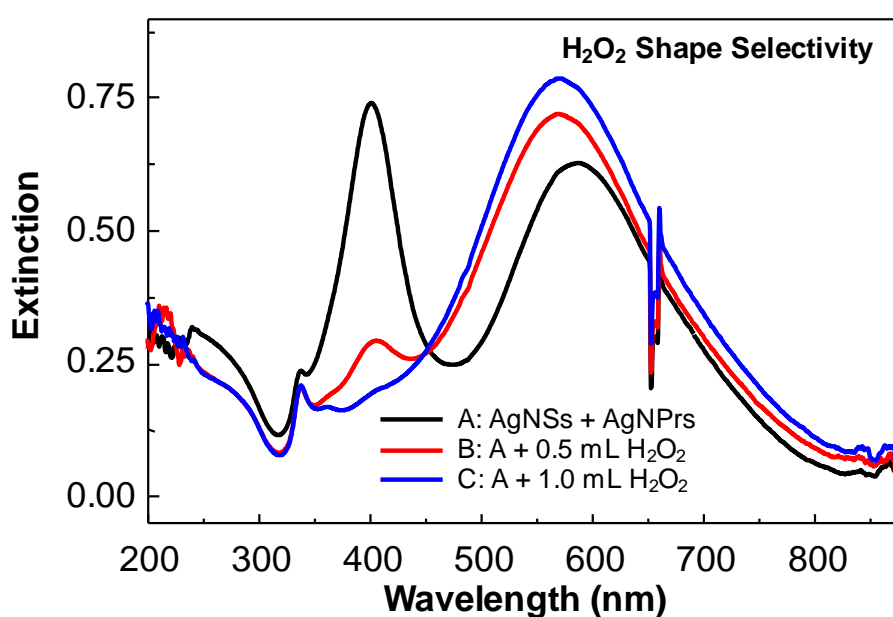
Figure 4.23   Plasmon extinction spectra show a selective etching of H_2O_2 toward AgNSs. AgNSs were completely dissolved when a larger volume of H_2O_2 was employed. An evidence of sculpturing of AgNPrs is noticed by the blueshift of the IPDPR from 588 to 570 nm. The experimental conditions: AgNSs (3.71 mM, 100 mL), AgNPrs (3.71 mM, 100 mL), H_2O_2 (0.5-1 mL).

Due to the facet-selective etching nature of H_2O_2, the expansion of energetically unfavourable facets was suppressed while the enlargement of {111} facet was promoted during the AgNPrs growth [52–53, 81]. Otherwise, we should observe the larger AgNSs generated from an isotropic crystal growth of the initial seeds. The monomeric Ag atoms necessary for AgNPrs growth were regenerated via the H_2O_2

reduction of oxidatively solubilized Ag^+ (Eq. 4.7). Half-cell potential of H_2O_2 (Eq. 4) implies its mild reducing power. The reducing capability of H_2O_2 is strongly dependent on pH (Figure 4.24), and is enhanced under a mild alkaline condition (pH > 8). When the reduction was performed under pH 10, a sharp and narrow DPR peak of AgNSs at 401 nm associated with the formation of small (less than 20 nm) nanoparticles was observed. Larger AgNSs were obtained at pH 9 as indicated by a broad DPR peak at 433 nm. Slow reduction rate at pH 9 lead to the formation of larger spherical nanoparticles due to the non-uniform nulceation.
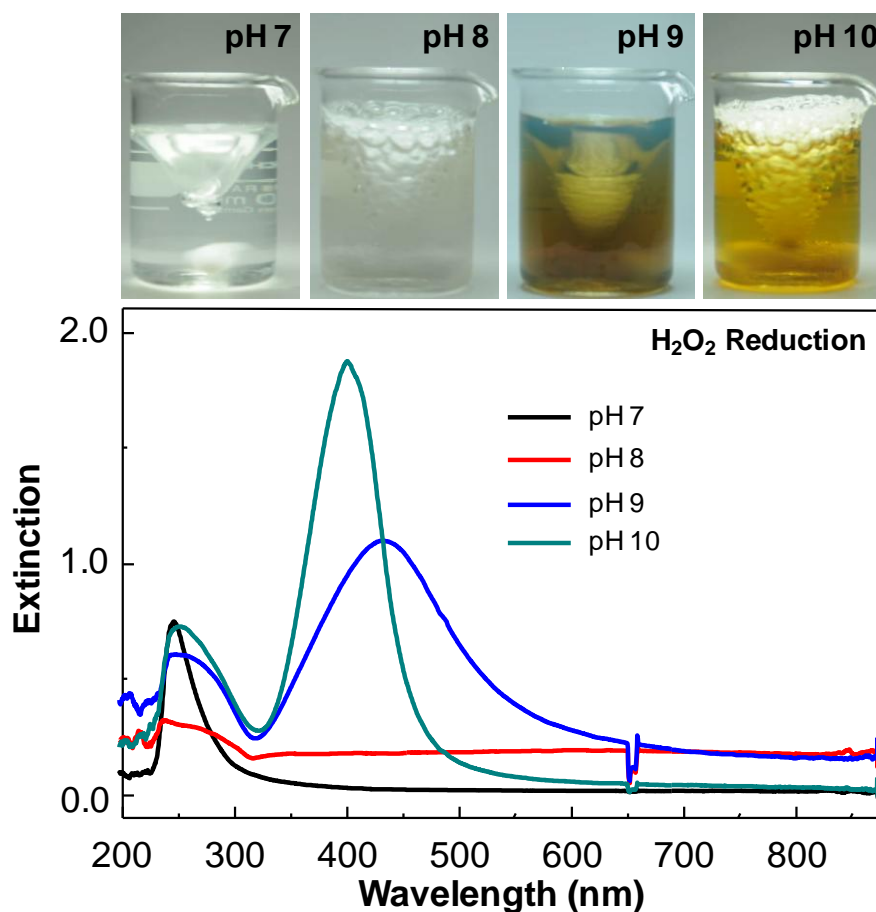
Figure 4.24   UV-visible spectra of solutions when 0.14 mM Ag^+ in 2% (w/v) soluble starch were reduced with H_2O_2 at various pH. The experimental procedure is the same as indicated in Figure 4.20 except for the volume of 1 M NaOH injected to obtain the specified pH. The reduction of Ag^+ did not occur at pH 7.

The oxidation and reduction cell potentials in Eq. 4.5 ($E_{cell}(Ox)$) and Eq. 4.7 ($E_{cell}(Red)$), respectively, are dependent on pH, molar concentration of Ag^+, and molar concentration of H_2O_2 as suggested by the Nernst equations:

$$E_{cell}(Ox) = 0.068 - \frac{RT}{nF} \ln \frac{[Ag^+]^2[OH^-]^2}{[H_2O_2]} \qquad (4.8)$$

$$E_{cell}(Red) = 0.947 - \frac{RT}{nF} \ln \frac{p(O_2)}{[Ag^+]^2[OH^-]^2[H_2O_2]}$$
$$= 0.947 - \frac{RT}{nF} \ln \frac{1}{[Ag^+]^2[OH^-]^2[H_2O_2]} \qquad (4.9)$$

For simplicity, the pressure of oxygen gas evolved during the reaction is approximately set equal to 1 atm. Based on the above expressions, the difference between the oxidation and oxidation cell potentials can be simplified as:

$$E_{cell}(Diff) = E_{cell}(Ox) - E_{cell}(Red) = -0.879 - 4\frac{RT}{nF}\ln[Ag^+][OH^-] \qquad (4.10)$$

The oxidation cell potential is a decreasing function, while the reduction cell potential is an increasing function with respect to pH (Figure 4.25) and [Ag^+] (Figure 4.26). The oxidation and reduction cell potentials possess the positive values in the range of pH from 7–12 suggesting H_2O_2 is capable of both oxidation and reduction. The potential gap between oxidation and reduction reaction is narrowed down when pH of the solution is increased. These suggest that both reactions may competitively occur in alkaline medium. Under the employed condition (pH 8–9), the result of this concerted oxidation/reduction is the shape transformation of AgNSs to AgNPrs. Increasing H_2O_2 concentration enhances both the oxidation potential toward AgNSs and the reduction potential toward Ag^+ (Figure 4.27). Interestingly, the molar concentration of H_2O_2 does not affect the potential gap since constant values of difference potential are observed at various pH (Figure 4.27 D). Therefore, the coordination of the oxidizing and reducing capabilities of H_2O_2 are mainly mediated by the alkalinity of the medium and available Ag^+ concentration. However, this

conclusion is valid only at a relatively low concentration of H_2O_2. At a high concentration of H_2O_2, more complicated reactions of H_2O_2 and Ag metal may occur such as an autocatalytic decomposition of H_2O_2 on the surface of silver metal or total dissolution of metallic Ag species.
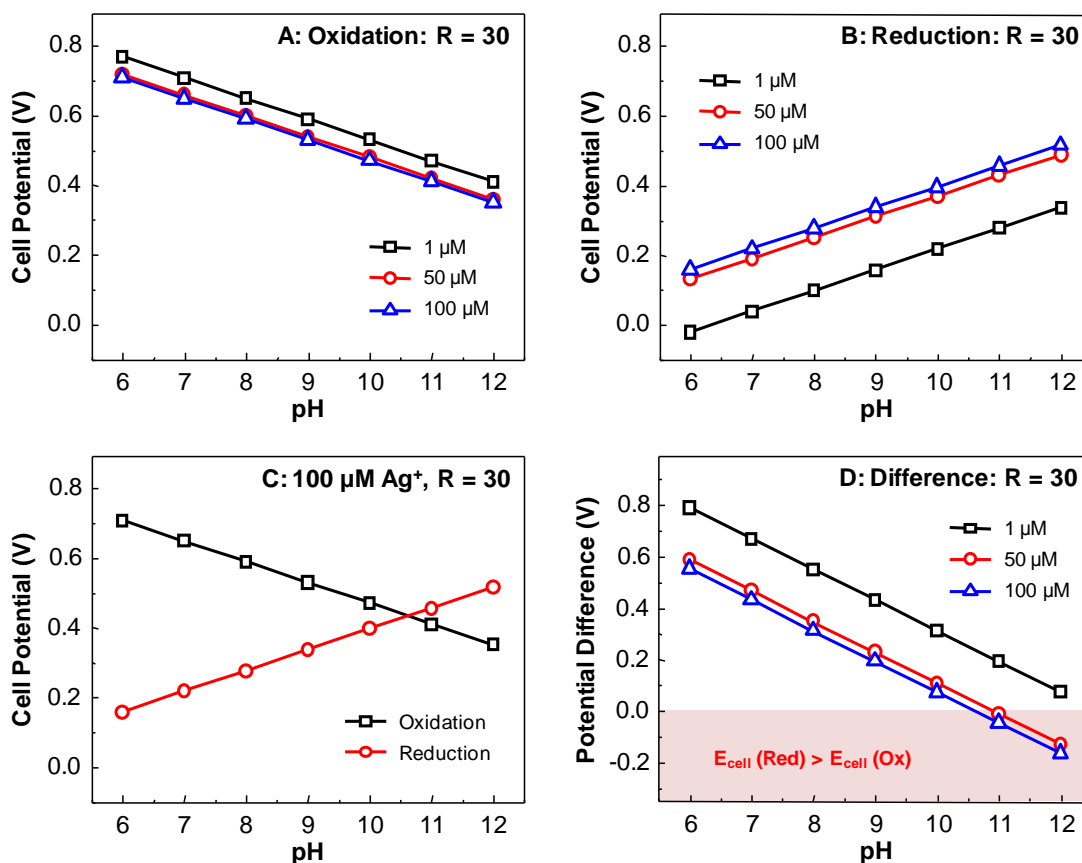
Figure 4.25   Plots of the oxidation cell potential (A), the reduction cell potential (B), comparison of the oxidation and reduction cell potentials (C), and the difference (oxidation – reduction) potential (D) as a function of pH. The cell potentials are calculated by Nernst equation with the concentrations according to those employed in the shape transformation process. The influence of Ag^+ concentrations (i.e., 1, 50, and 100 μM) are compared in (A) and (B) for the oxidation and reduction cell potentials, respectively. The reduction is dominant at high pH and/or high Ag^+ concentration. The molar ratio R of H_2O_2:Ag^+ is 30. The temperature is set at 301.15 K. The pressure of evolved oxygen gas is assumed the ambient pressure.
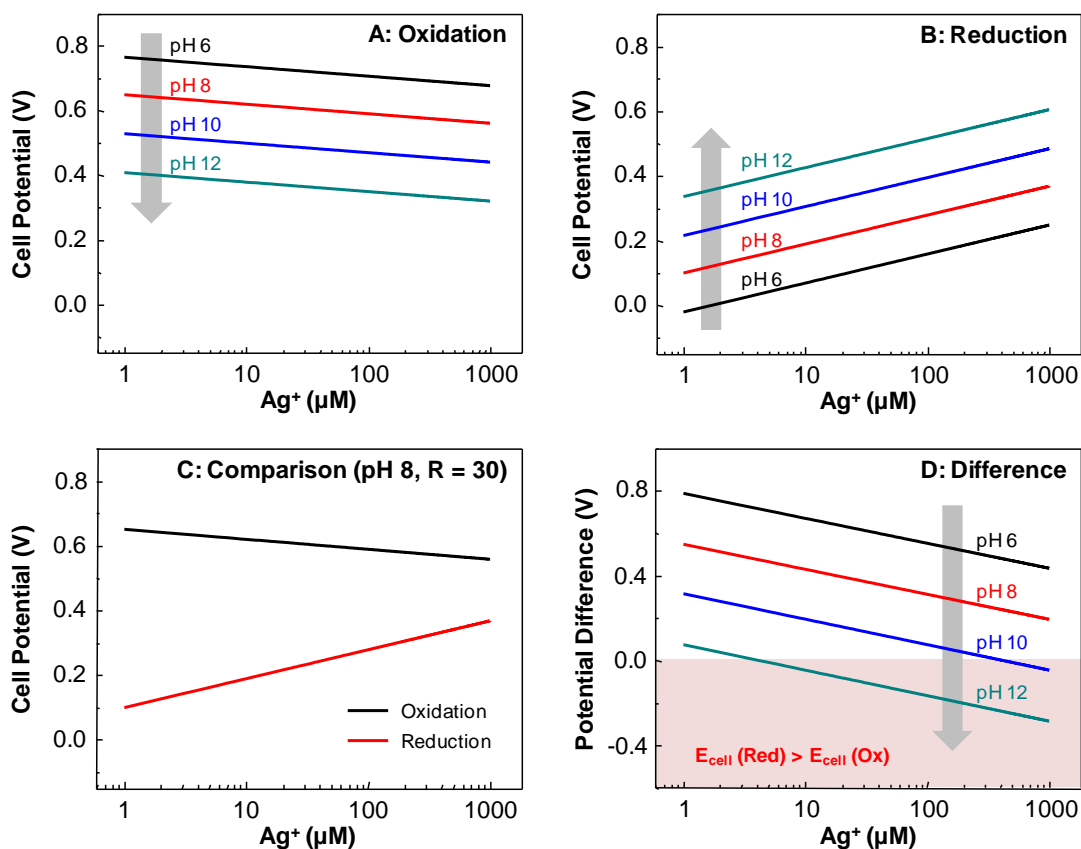
Figure 4.26   Plots of the oxidation cell potential (A), the reduction cell potential (B), comparison of the oxidation and reduction cell potentials (C), and the difference (oxidation – reduction) potential (D) as a function of [Ag^+]. The calculations are performed at pH 6, 8, 10, and 12. The molar ratio R of H_2O_2:Ag^+ is 30. The temperature is set at 301.15 K. The pressure of evolved oxygen gas is assumed the ambient pressure.

A low molar ratio of H_2O_2:AgNSs (R < 100) is deliberately employed to sufficiently etch AgNSs while facilitate the construction of AgNPrs without further destroying the *in situ* generated AgNPrs [81, 90]. Due to the greater instabilities of AgNSs toward H_2O_2 etching, the AgNPrs survived and remained as the sole product (Figures 4.23 and 4.28). An insignificant spectral change after a 3-month storage suggests that AgNPrs are very stable under the synthetic environment. An absent of the absorption at 250-270 nm indicates that H_2O_2 is completely consumed by the shape conversion process (cf. Figure 4.5). H_2O_2 was also consumed by the

autocatalytic decomposition on the surface of metallic Ag (Eq. 4.11) and homogeneous base-catalyzed decomposition pathways (Eq. 4.12) [66, 71].

$$2H_2O_2 \xrightarrow{\text{Ag}} 2H_2O + O_2 \tag{4.11}$$

$$H_2O_2 + HOO^- \rightarrow H_2O + O_2 + HO^- \tag{4.12}$$
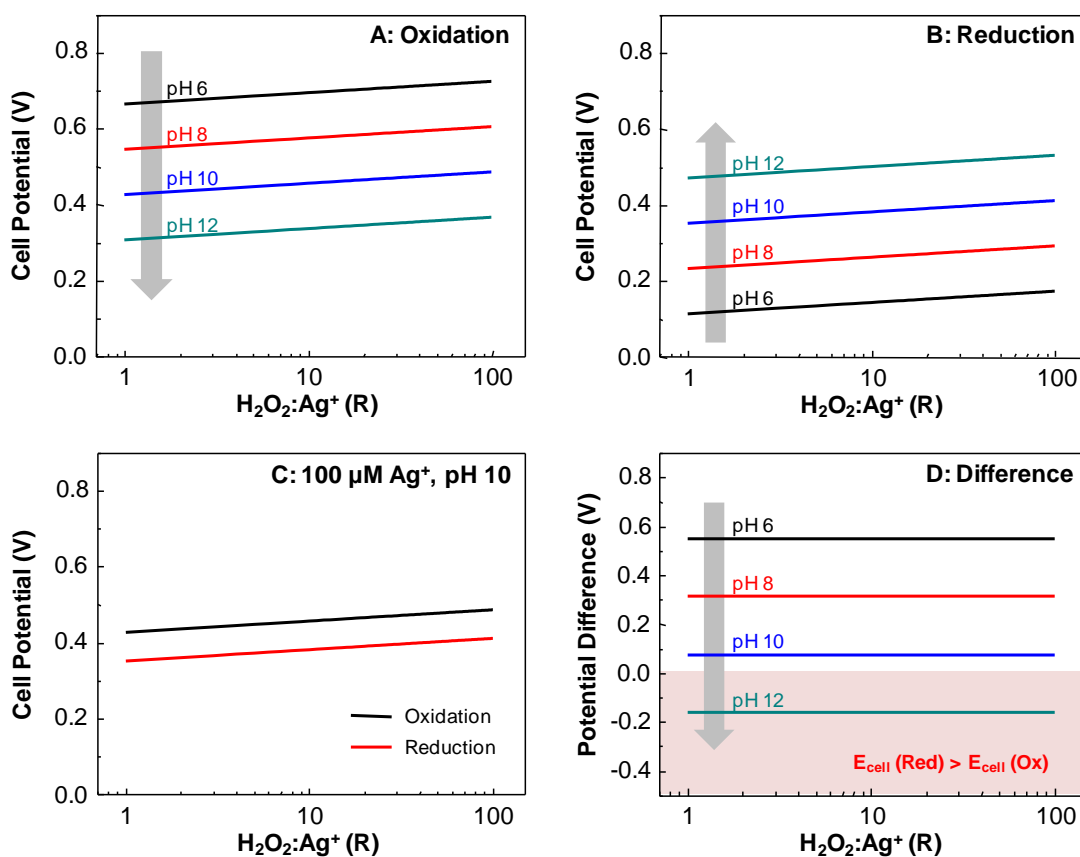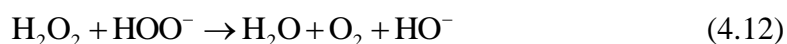
Figure 4.27 Plots of the oxidation cell potential (A), the reduction cell potential (B), comparison of the oxidation and reduction cell potentials (C), and the difference (oxidation – reduction) potential (D) as a function of the molar ratio of H_2O_2:Ag^+ (R). The calculations are performed at pH 6, 8, 10, and 12. The molar concentration of Ag^+ is 100 μM. The temperature is set at 301.15 K. The pressure of evolved oxygen gas is assumed the ambient pressure.
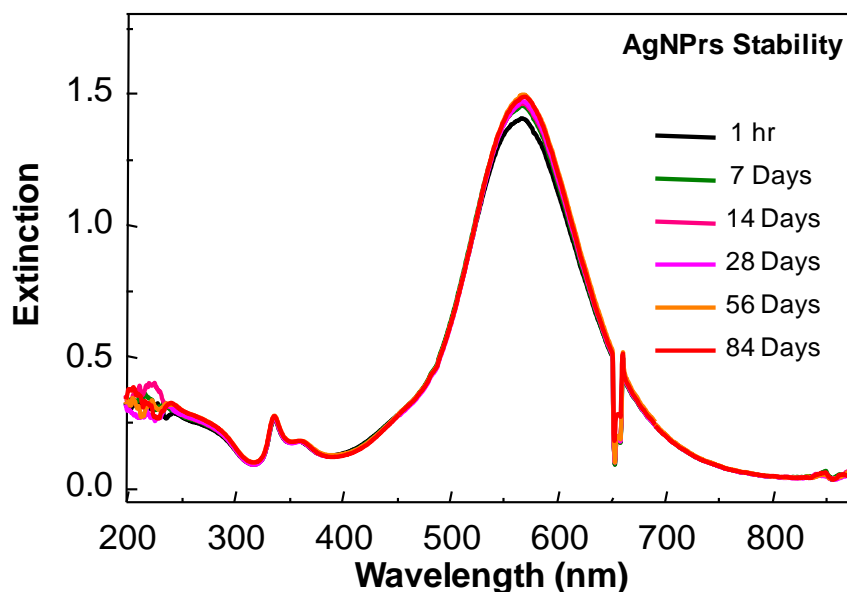
Figure 4.28   Plasmon extinction spectra reveal the stability of AgNPrs under a prolong storage. The AgNPrs colloid was synthesized at the concentration of 3.71 mM. The colloid was stored under the ambient conditions without additional purification. For quantitative comparison, the measured colloids were diluted to 92.7 μM by deionized water before each measurement.

4.3.3 The Role of AgNSs

AgNSs play two important roles in the shape transformation process. For the *seeding role*, they are the starting material for generating planar twinned seeds. The oxidatively modified AgNSs seeds with planar twinned defects act as the new nucleation sites for the homogeneous overgrowth. For the *growth role*, they are the only internal source of Ag^+ ions and the active sites for subsequent atomic addition. AgNSs seeds immediately reacted with H_2O_2 when it was introduced into the colloidal suspension without the latent period compared to previous studies [51–53]. Small sizes of AgNSs (diameter less than 10 nm) are the principal factor for the lability (i.e., lower standard reduction potential [26] and higher instability compared to the larger particles [32], and highly fluctuating crystal structures containing multiplicities of indeterminable defects [75–77]). Only oxidative disintegration of

AgNSs by H_2O_2 without the shape transformation was observed when non-stabilized AgNSs with mean diameter > 10 nm were employed (cf. Figure 4.19 D). The small sizes of starting AgNSs are crucial for nanoprism growth [24, 26, 31, 74]. High concentration of the starting AgNSs increases the collision probability of the basic construction units (i.e., AgNSs seeds with planar twinned defects and regenerated monomeric Ag atoms) and the formation of AgNPrs is promoted. The shape transformation was not observed in previous studies where polymer-capped AgNSs were employed as H_2O_2 sensor due to a much lesser AgNSs concentration ([AgNS] < 0.5 mM) and neutral solution (pH 7.4) condition [81–82].

4.3.4 Proposed Shape Transformation Mechanism

Epitaxial anisotropic atomic addition of regenerated Ag atoms on the etched seeds is involved in planar nanocrystal growth (Figure 4.29). Circular nanodisks are initially formed in the AgNPrs growth solution (cf. Figure 4.12 E). Continuous tip- or edge-addition of monomeric Ag atoms causes the enlargement of circular AgNPrs and subsequent formation of faceted AgNPrs i.e., hexagonal, truncated triangular, and rounded-tip triangular AgNPrs.
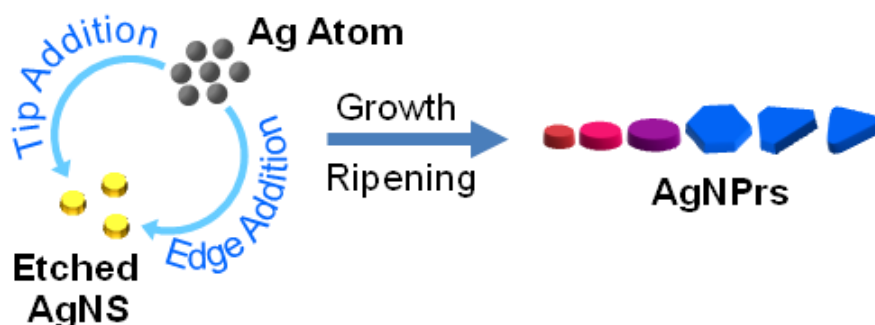
Figure 4.29   Epitaxial growth of AgNPrs from etched AgNSs and regenerated Ag atoms.

In general, the AgNPrs fabrication was facilitated by the facet-specific capping molecules, particularly citrate (TSC), resulting in the enlargement of {111} facet [74–76, 86]. For our system, however, when TSC was incorporated into initial AgNSs

colloid even with the molar ratio of TSC:AgNSs as low as 1, no appreciable morphological transformation was detected after the injection of H_2O_2 (Figure 4.30). When R was increased from 50 to 400, DPR intensity at 400 nm of AgNSs decreased without any development of a new absorption. A color change from yellow to orange-brown with a redshift of the DPR peak position from 402 nm to 427 nm was noticed. The observed redshift is attributed to a formation of larger AgNSs. Moreover, at high R (200–400), there was a peak emerged at 250 nm attributing to the residual H_2O_2 (Figure 4.5). The presence of H_2O_2 together with TSC complexing agent exerts a strong oxidizing environment. AgNSs were only oxidatively solubilized to Ag^+ with a concomitant reduction of pH [68] from 8.6 (R = 0) to 3.8 (R = 400) without a regeneration of metallic Ag species. The etched Ag^+ could subsequently complex with available citrate molecules. Ag^+-citrate complex (Ag-TSC) was utilized as a controlled release agent slowing down the reaction rate and minimizing the self nucleation in the seed mediated growth of high aspect ratio AgNPrs [8]. A mild reducing action of H_2O_2 could not overcome the affinity of Ag^+ toward TSC, and Ag^+ would not be re-reduced to monomeric Ag atoms. However, when $NaBH_4$ was added to the transparent solution with R = 200, the yellow colloid was regenerated (Figure 4.30 B). The DPR peak position at 385 nm of the re-reduced AgNSs was due to the stabilization by citrate ions. These results confirmed that Ag^+ ions were generated from AgNSs during the H_2O_2 etching process. A high mole ratio R of 100 was required for the degradation of AgNSs to be visualized in the presence of TSC. The strong surface capping and passivation of citrate on metallic Ag also diminished the surface availability of AgNSs to be oxidatively etched by H_2O_2. In contrast, without TSC, AgNSs were readily transformed to AgNPrs as indicated by the OPQPR at 345 nm and IPDPR at 580–800 nm (Figure 4.31). TSC totally inhibits the H_2O_2-induced shape transformation. Therefore, the inherent crystal defects (i.e., planar twinned defects and stacking faults parallel to {111} facets [5, 26, 83–84], and re-entrant grove [30, 32, 74]) presented in etched AgNSs seeds are indispensable for the formation and growth of AgNPrs. Because of the limited number of Ag atoms, the complexation between Ag^+ and soluble starch, and the slow reduction rate of H_2O_2 under the mild alkaline condition, we propose that the growth of AgNPrs undergoes the kinetically controlled pathway [30, 44, 46, 76, 86].
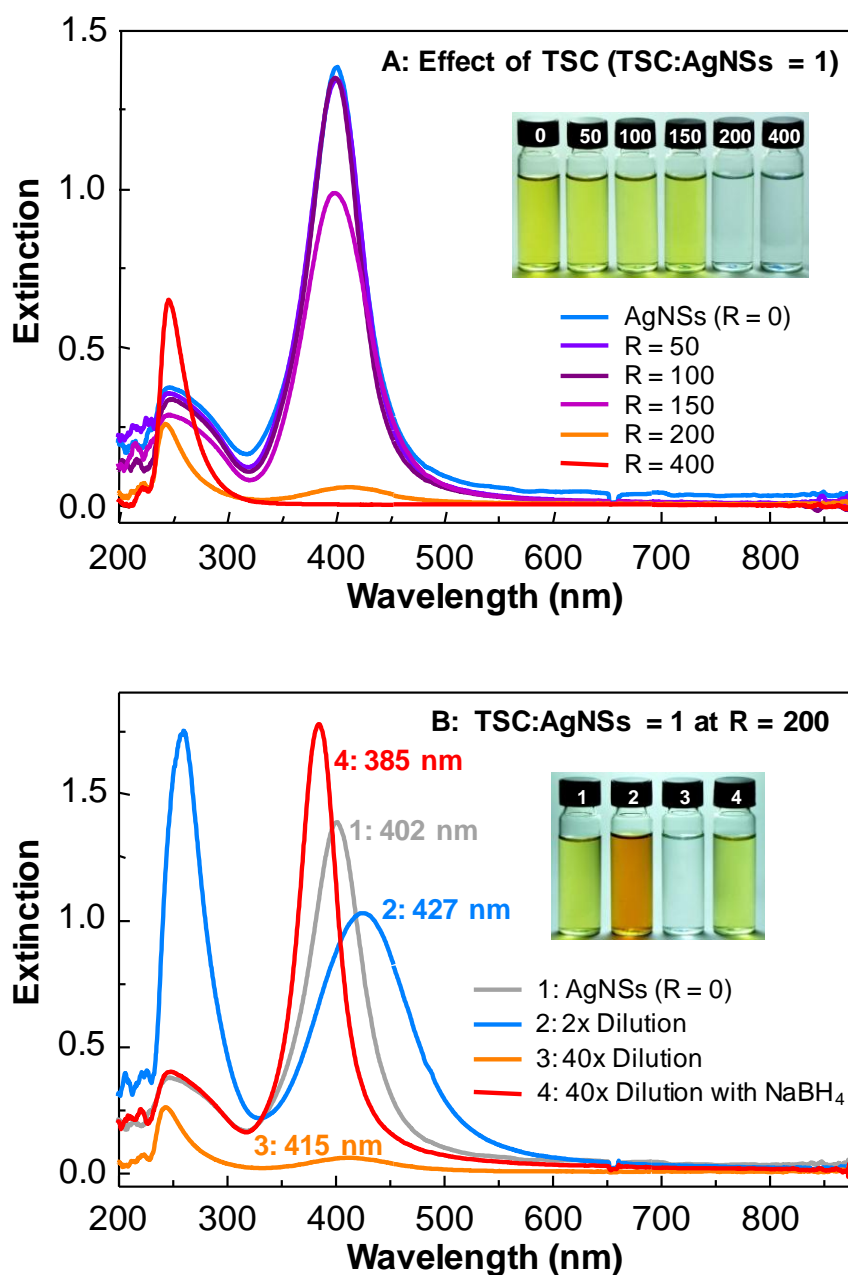
Figure 4.30 The effect of trisodium citrate (TSC) on the AgNPrs development at various molar ratio of H_2O_2:AgNSs (R) (A). Comparison of the extinction spectra of the AgNSs (1), AgNSs+TSC+H_2O_2 at R = 200 with various dilution factors (2 and 3), and the suspension 3 after an addition of NaBH$_4$ (4) is also shown (B). The experimental parameters were the same as indicated in the experimental section except that TSC was added to in AgNSs with the molar ratio of TSC:AgNSs = 1 before the injection of H_2O_2 solution.
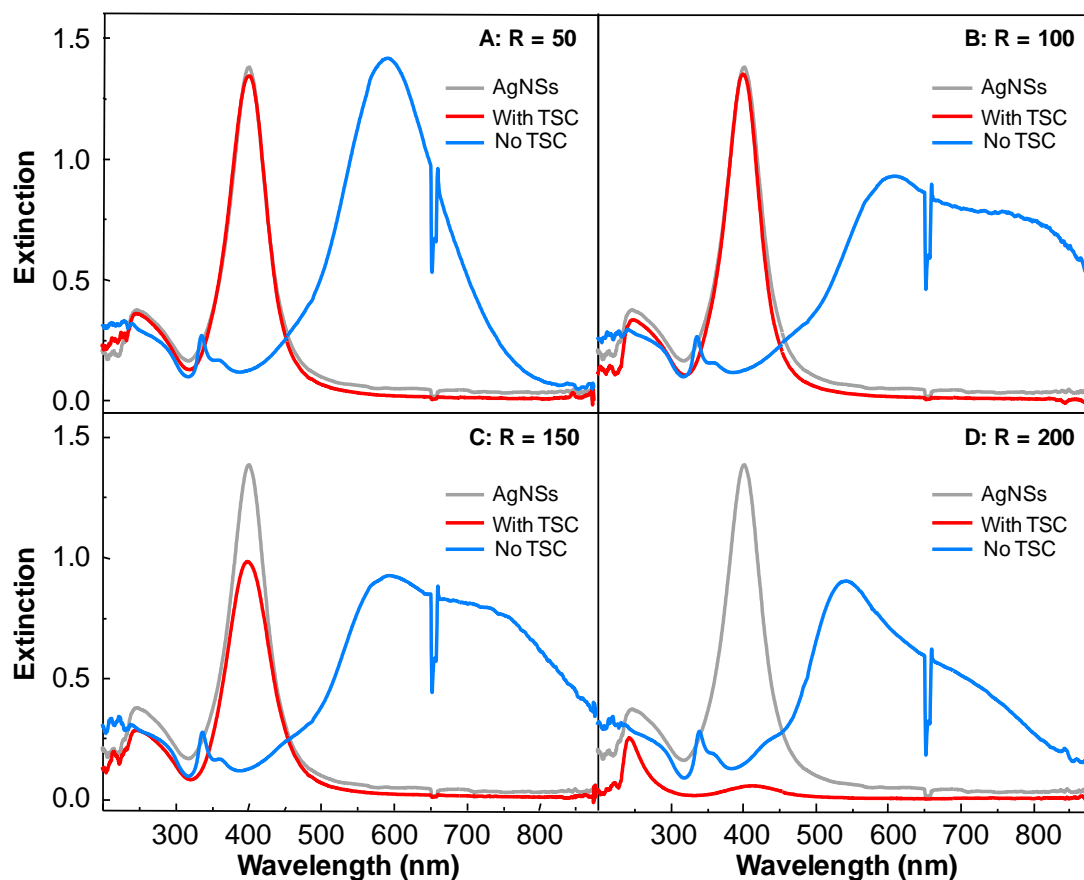
Figure 4.31   The effect of trisodium citrate (TSC) on the AgNPrs development at various molar ratio of H_2O_2:AgNSs (R). Extinction spectra of AgNSs, AgNSs+H_2O_2, and AgNSs+TSC+H_2O_2 are compared in each panel.

4.4 Morphological Evolution of AgNSs-to-AgNPrs induced by H_2O_2

In order to investigate the morphological evolution progress from AgNSs to AgNPrs, extinction spectra of the colloidal suspensions at various molar ratio of H_2O_2:AgNSs from 0–200 were systematically investigated (Figure 4.32). When shape conversion of AgNSs induced by H_2O_2 was performed, a sphere-to-prism conversion was visually observed via a systematic color change from yellow to red, pink, purple, and blue. A larger amount of H_2O_2 induced a greater redshift on the color of colloids. The virgin AgNSs colloid has a single LSPR at 400 nm with a narrow full width at half maximum (FWHM) of 40 nm indicating AgNSs with narrow size distribution.
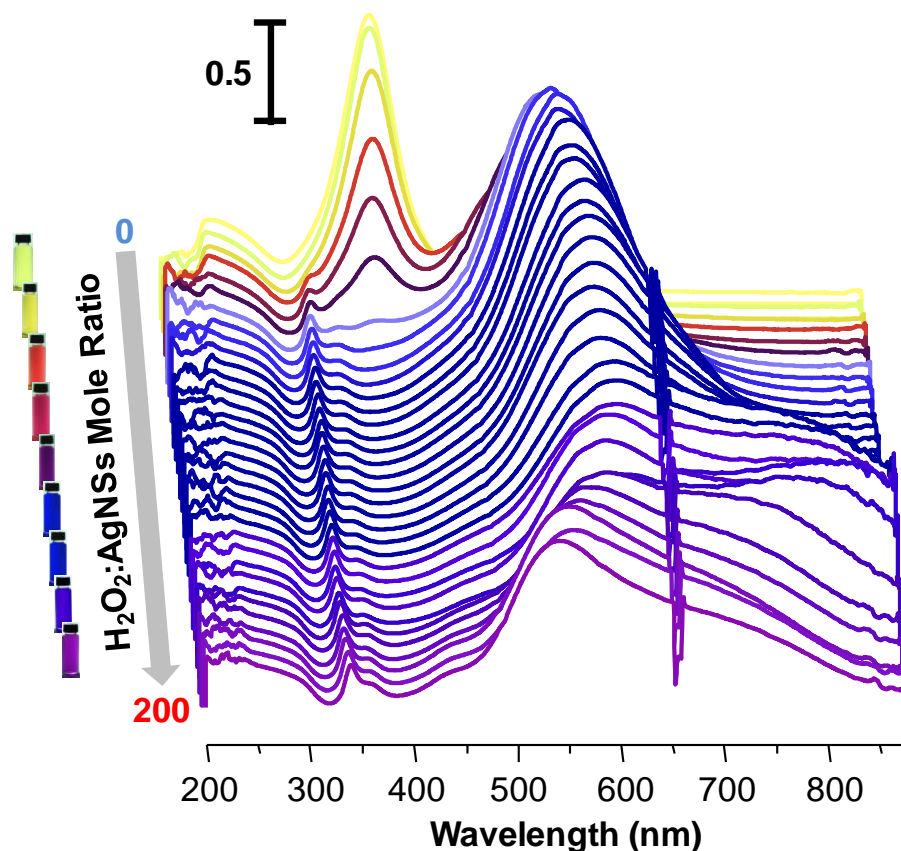
Figure 4.32   Changes in the UV-visible spectra and the color of corresponding colloidal AgNPs through the structural evolution induced by the amount of converting reagent (H_2O_2). The bar indicates extinction intensity of 0.5 (a.u.).

When a small volume of H_2O_2 was added, the color of the colloid immediately changes from yellow to red with a concomitant decrease in LSPR peak at 400 nm. Moreover, two new distinct plasmonic extinction bands simultaneously develop. They demonstrate the destruction of AgNSs and the occurrence of AgNPrs. Extinction at ~340 nm is associated with the transverse (out-of-plane) quadrupole oscillation, which directly relates to the plate aspect ratio, and another one at approximately 500 nm is the IPDPR peak which continuously redshifts up to 600 nm as an increase in H_2O_2 concentration. The redshift implies a particle growth with an increase in lateral size. The direct conversion from sphere to plate was confirmed by an isosbestic point at ~450 nm and a complete disappearance of LSPR at 400 nm (cf. Figure 4.12). At this state, this observation suggests AgNSs were completely consumed and

transformed to only plate structure with no other shapes. At higher ratios of H_2O_2:AgNSs, a broad LSPR band centered at ~800 nm developed with a decrease in band intensity at 600 nm. This observation suggests a further growth of large AgNPrs with an expense of small nanoplates [1, 53, 54]. However, when an excessive amount of H_2O_2 was added, the plasmon band at 800 nm is decreased with a slight blueshift of dipole plasmon extinction at 600 nm. This observation signifies a disintegration of large AgNPrs. The plate disintegration was visually observed via a color change from blue to pale purple.

4.4.1 Chemometric Analysis of the Spectrophotometric Data and Shape Evolution of AgNSs to AgNPrs Induced by H_2O_2

To propose the mechanism of the structural evolution from AgNSs to AgNPrs, it is necessary to accurately determine the intermediates presented during the reaction. To evaluate the numbers of conversion reaction steps possessing distinguished spectral characteristics, the spectra in form of a data matrix is subjected to factor analysis and the error indicator functions as summarized in Table 4.3.

Table 4.3   Results of application Factor Analysis and Error Indicator functions on the UV-visible spectral data matrix.

Factor	EV[a]	Log EV[b]	EVR[c]	RSS[d]	RSD[e]	RPV[f]
1	16856.97	4.23		2573.62	0.207	26.64
2	1421.24	3.15	0.08	1152.38	0.138	26.64
3	925.96	2.97	0.65	226.42	0.061	19.65
4	166.09	2.22	0.17	60.32	0.031	20.10
5	48.19	1.68	0.29	12.12	0.014	13.25
6	0.88	-0.05	0.01	0.32	7.4e-4	44.77

[a] Eigenvalue, [b] Logarithm of Eigenvalue, [c] Ratio of the ith eigenvalue, [d] Residual sum of square, [e] Residual standard deviation, [f] Residual percent variance

In this table, the results from factor analysis functions [115] which are the eigenvalue (EV), the logarithm of eigenvalue (Log EV), ratio of the ith eigenvalue (EVR) to its previous one and error indicator functions [115] which are residual sum of square (RSS), residual standard deviation (RSD), and residual percent variance (RPV) are represented. For EV, Log EV, EVR, RSS and RSD, the chemical rank is determined by finding the break of statistical value or the point will be flatted or level-off, while for RPV, the chemical rank is determined by finding the optimum point that gives the minimum error [115]. A large separation between the fifth and the sixth components is observed from functions EV, Log EV, RSS RSD and RPV, while EVR does not give the obvious answer. However, the majority reported statistical data indicates that the first 5 principal components contain systematic variances and the rest are corresponding to noise. This suggests that the absorbance spectra are represented from 5 major components. Besides, the percentage variance from only the major components is calculated. The first 5 major components could explain 99.9% of overall variances in the absorbance spectra and the remaining variance may attribute to the noise.   After chemical rank analysis, these performed approaches suggest that the most appropriate number of contributed components is 5, which means five different characteristics of metallic nanosilver species are produced through the transformation reaction. In the other words, when AgNPs are evolved, five different characteristic particles with distinct absorbance spectra are produced. These findings are supported by the investigations of the color of the solution. Slight deviation from spherical geometry of nanoparticles can lead to dramatic color changes (Figure 4.32).

After the number of major components in the data was determined, the next step is to estimate the concentration profiles and absorptivity profiles of each species. To obtain an initial estimate of the concentration profile and pure spectra of the detected species as a function of the ratio of H_2O_2:AgNSs, the UV-visible absorbance spectra are subjected to SIMPLe-to-use Interactive Self-modeling Mixture analysis Approach (SIMPLSMA) [36]. The basic principal of SIMPLISMA is based on discovering the pure variables without any provided informative clues. In this case, a pure variable is corresponding to a spectrum contributed from only one component of the mixture. Once, the pure spectra of each component are determined, the evolutional profiles in

the mixture spectra can be calculated. This method was used to obtain the number of significant factors. The result of SIMPLISMA shows a significance systematic variation only for the first five factors. This represents that five different characteristics of nanosilver species are produced that is in good agreement with the results from factor analysis, and error indicator functions. The initial purest spectra (S_0) of each specie obtained from SIMPLISMA is the spectrum at the ratios H_2O_2:AgNSs of 0, 7.5, 25, 60 and 140, respectively. Thus, the multivariate curve resolution alternative least squares analysis (MCR-ALS) is performed on the selected absorbance spectra by considering only 5 major chemical components existing in the evolution system. A significant application of the MCR-ALS is to extract the concentration profiles of the 5 major components (defined as P1-P5). The normalized concentration profiles of the resolved components obtained from MCR-ALS analysis for the five-component system are shown in Figure 4.33.
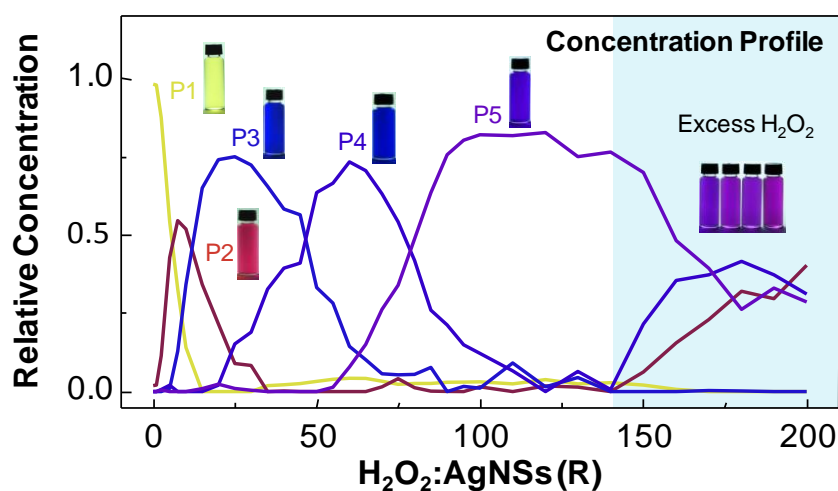
Figure 4.33   Relative concentration profiles of the five significant components (P1-P5) and corresponding color of colloid in the AgNSs-to-AgNPrs structural evolution induced by H_2O_2.

Due to the constraints, the different ratios of P5 components were selected (the mole ratio of 120 was selected by MCR-ALS calculation, while the mole ratio of 140 was selected by SIMPLISMA). However, the extinction spectrum contains the similar plasmonic extinction spectra (Figure 4.34) and the majority of selected ratios are in

good agreement with the output obtained from SIMPLISMA analysis and the corresponding color of the colloids.
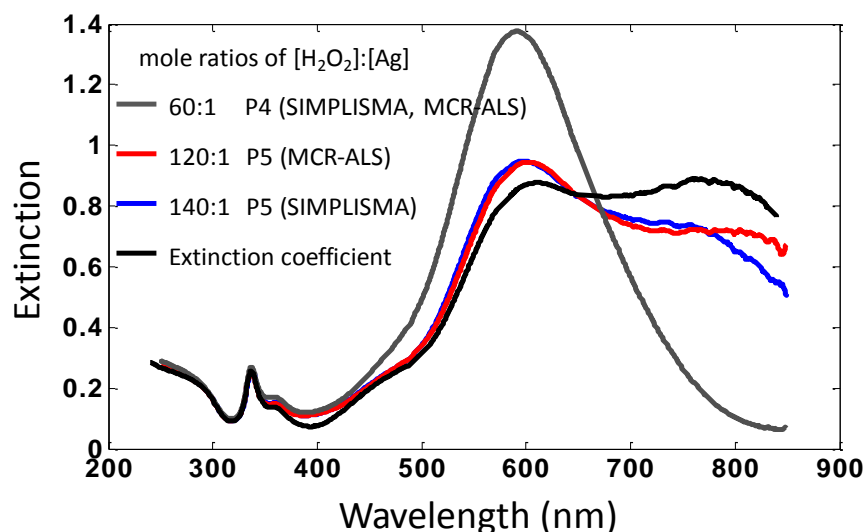
Figure 4.34   The UV-visible spectra of colloids with the molar ratios of H$_2$O$_2$:AgNSs at 140 and 120 for component P5 selected by SIMPLISMA and MCR-ALS calculation, respectively, compared to the calculated extinction spectra of component P5.

The shift of color from bright yellow to blue confirms the successful conversion from spheres to plate. At the beginning, the yellow colloid (P1) changes to red (P2) when the mole ratio is increased to 7.5. From the concentration profiles, the component P2 has short lifetime. The transformation of P2 to P3 corresponds to the development of the blue colloid. The development of P4 from P3 was not obviously detected from the color of the colloid. However, chemometric analysis could clearly differentiate the structural change numerically. The structural conformation of these components according to the numerical differentiation was later confirmed by TEM measurements. The color converted from blue to purple as the development of component P5. This result cannot be directly explained from only the concentration profile, but we will later elaborate the benefit of pure extracted spectrum in the next section. In this work, size and shape of particle were grown by an addition of H$_2$O$_2$. On the contrary, some reports [52, 54] show that excess H$_2$O$_2$ can be used to etch

nanoparticles to obtain the desired structures. Therefore, with an excess H_2O_2 (at the mole ratio of H_2O_2:AgNSs greater than 140), the etching process might outperform the growth process. The component P5 was etched and decomposed into components P2 and P4 and the colors are mixed by those of components P2 (red) and P4 (blue) which represents as purple. The unity nanoparticle conversion (AgNSs is solely converted to AgNPrs) in the synthesis was proven by the addition of a reducing agent (NaBH$_4$) into Ag colloids as shown in Figure 4.35. Two colloids (initial AgNSs colloid and one of AgNPrs colloid) were chosen to demonstrate this situation. If Ag$^+$ ion remains in the colloids, the intensity in extinction spectra (at 400 nm) will increase. In Figure 4.49, only small blueshift with a little decrease in the intensity can be observed after the addition of NaBH$_4$ in both AgNSs and AgNPrs colloids, which can be explained by the aggregation/deaggregation of Ag nanoparticles due to the electrical stabilization of BH^{4-} [88]. Any increase in the intensity cannot be noticed. Furthermore, the colloids with existing Ag ions were simulated by adding small amount of Ag$^+$ (5 ppm) into the original one. Then, the Ag$^+$-spiked colloids were added by NaBH$_4$. The results show an increase in the intensity at ~400 nm in spectra of both cases, which indicates the generation of new Ag nanospheres. From these results, we believe that the unity nanoparticle yield in our procedures is demonstrated at the measurement time.
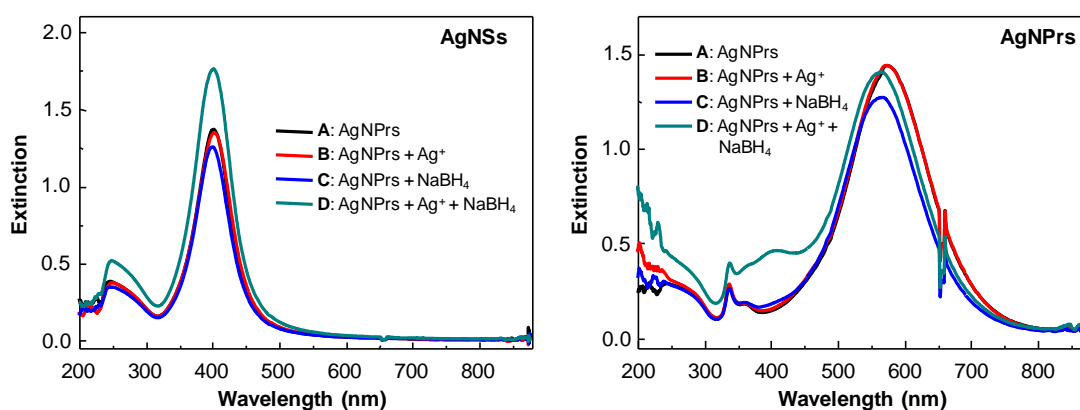
Figure 4.35   Extinction spectra of the AgNSs and AgNPrs after the addition of extra Ag$^+$ and/or a reducing agent (NaBH$_4$).

Another important information obtained from MCR-ALS calculation is the pure spectra of those significant components which contain the unique plasmonic extinction corresponding to the characteristics of the particular shape and size. To get an insight understanding on the shape transformation, the morphologies of the predicted components were revealed using TEM analysis. The TEM images of each component must be accurately compatible with their pure spectra in order to confirm that the detected structures are the major morphologies dispersed in the colloids. The corresponding pure spectra of each component are illustrated in Figure 4.36. The overall morphological evolution from AgNSs to AgNPrs with respect to increasing molar ratios of H_2O_2:AgNSs from 0 to 200 is depicted in Figure 4.37.
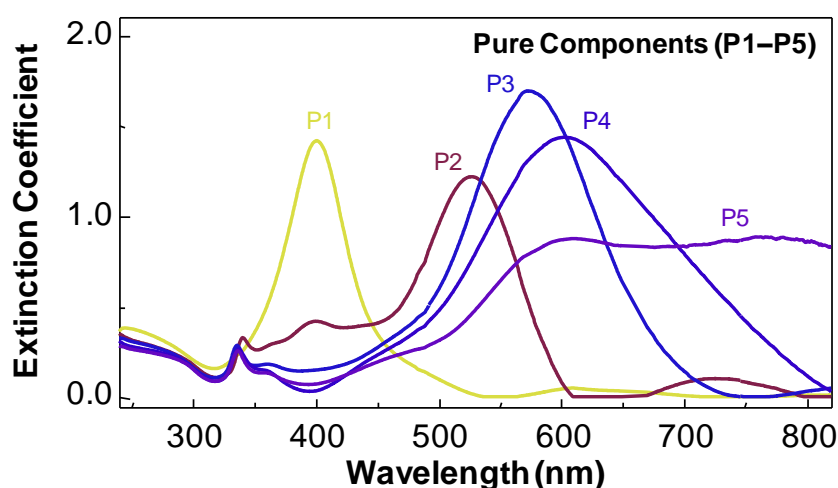
Figure 4.36   Resolved pure spectra of the five distinct chemical components (P1–P5).

Based on the progressive plasmon extinction spectra (Figure 4.32), chemical rank analysis (Table 4.3), relative concentration profile (Figure 4.33), extinction spectra of pure components (Figure 4.36), and morphological analysis of TEM micrographs (Figure 4.37), we can now propose the AgNSs-to-AgNPrs structural evolution. The morphological evolution can be divided into 3 states: AgNSs-to-AgNPrs transformation (P1, P2, and P3), AgNPrs-to-AgNPrs reformation (P3, P4, and P5), and disintegration (P2, P4, and P5).
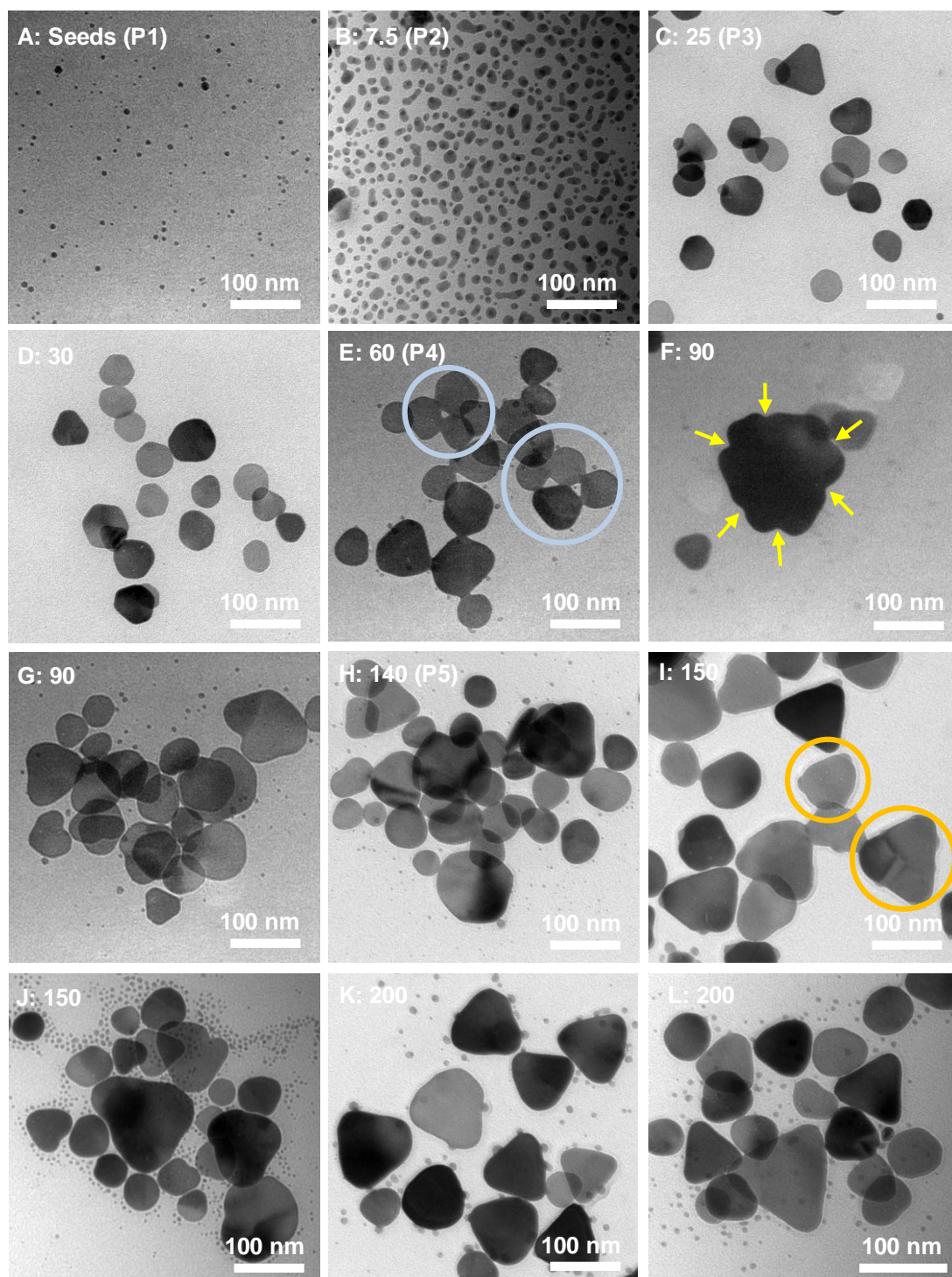
Figure 4.37   TEM micrographs showing the morphological evolution of AgNSs to AgNPrs at various molar ratios of H_2O_2:AgNSs from 0 (seeds) to 200. The pure components corresponding to the Figure 4.50 are also indicated.
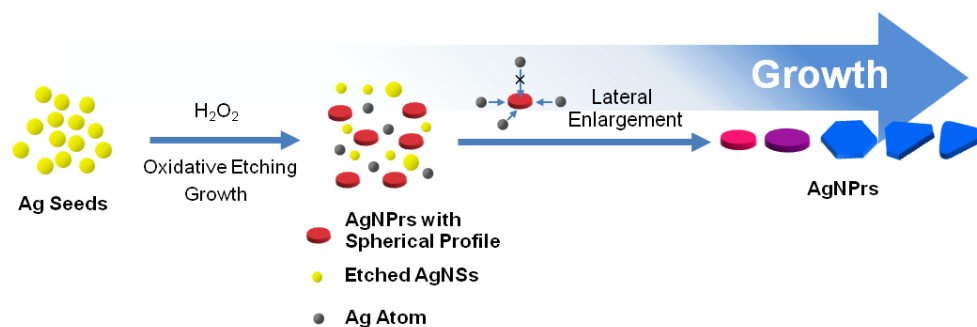
Figure 4.38   Schematic diagram showing the transformation from AgNSs (P1) to AgNPrs (P3).

In the first state (Figure 4.38), after addition of H_2O_2 to AgNSs (P1; H_2O_2:AgNSs = 0), spherical nanoparticles (Figure 4.37 A) are rapidly transformed into nanoprisms with quasi-spherical profile (P2; H_2O_2:AgNSs = 7.5; Figure 4.37 B). Spherical nanoparticles are preferentially etched by H_2O_2, while short-lived circular nanoprisms played a role as new nucleation sites for epitaxial atomic addition of Ag atoms generated from H_2O_2-reduced Ag^+. The lateral enlargement is continued as H_2O_2:AgNSs increases until the spherical nanoparticles and circular nanoprisms are exhausted (Figure 4.33). This results in the formation of AgNPrs pure component P3 (H_2O_2:AgNSs = 25).

In the second phase (Figure 4.39), P4 is gradually developed from P3. AgNPrs undergo the oriented attachment growth pathway [116–119] as evidenced in the TEM micrograph (Figure 4.37 E, blue circles). In addition, AgNPrs with jagged edge are observed when H_2O_2:AgNSs increases to 90 (Figure 4.37 F, yellow arrows). The consumption of P4 for constructing P5 is evidenced in the decrement of plasmon extinction intensity at 600 nm and gradual increment of plasmon extinction intensity at 800 nm. In addition, relative concentration of P4 is gradually decreased when H_2O_2:AgNSs increases from 60 to 140 in concomitant with the development of P5. Oriented attachment growth of AgNPrs continues until the complete development of the pure component P5 (H_2O_2:AgNSs = 140; Figure 4.37 H). However, prism growth may also develop via the Ostwald ripening pathway since small spherical particles are observed in the TEM micrographs (Figures 4.37 G and H).
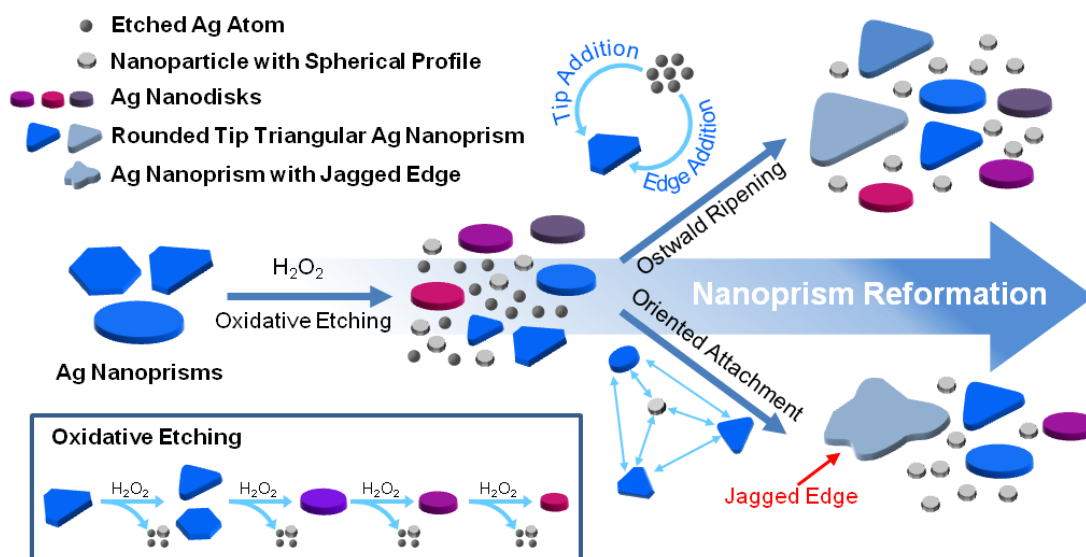
Figure 4.39   Schematic diagram showing AgNPrs (P3)-to-AgNPrs (P4 and P5) reformation through Ostwald ripening and oriented attachment pathways. The oxidative etching pathway (H_2O_2:AgNSs > 140) is also indicated.

In the third state (Figure 4.39, oxidative etching) when H_2O_2:AgNSs is more than 150, the disintegration of AgNPrs begins to dominate. Many small nanoparticles with spherical profiles are observed (Figures 4.37 J–L). These small nanoparticles are associated with the pure component P2 as its relative concentration is increased (Figure 4.33). AgNPrs with similar characteristic of the pure component P4 are observed in the TEM micrographs in corresponding with increasing relative concentration in the concentration profiles. AgNPrs are laterally disintegrated by H_2O_2. The mixture of P2 (red color) and P4 (blue color) is reflected through the vivid violet color of the resulted colloid (H_2O_2:AgNSs > 170).

4.5 Influences of Experimental Parameters and Optical Tunability

Due to the spontaneous, exothermic, and violent natures of the H_2O_2-induced AgNSs-to-AgNPrs transformation reaction, the growth of AgNPrs and their LSPR property are expected to be highly sensitive to the experimental conditions. Three

experimental parameters i.e., initial AgNSs concentration ([AgNSs]), H_2O_2 flow rates $(F(H_2O_2))$, and mixing efficiency (or disperser speed (Ds)) were investigated.
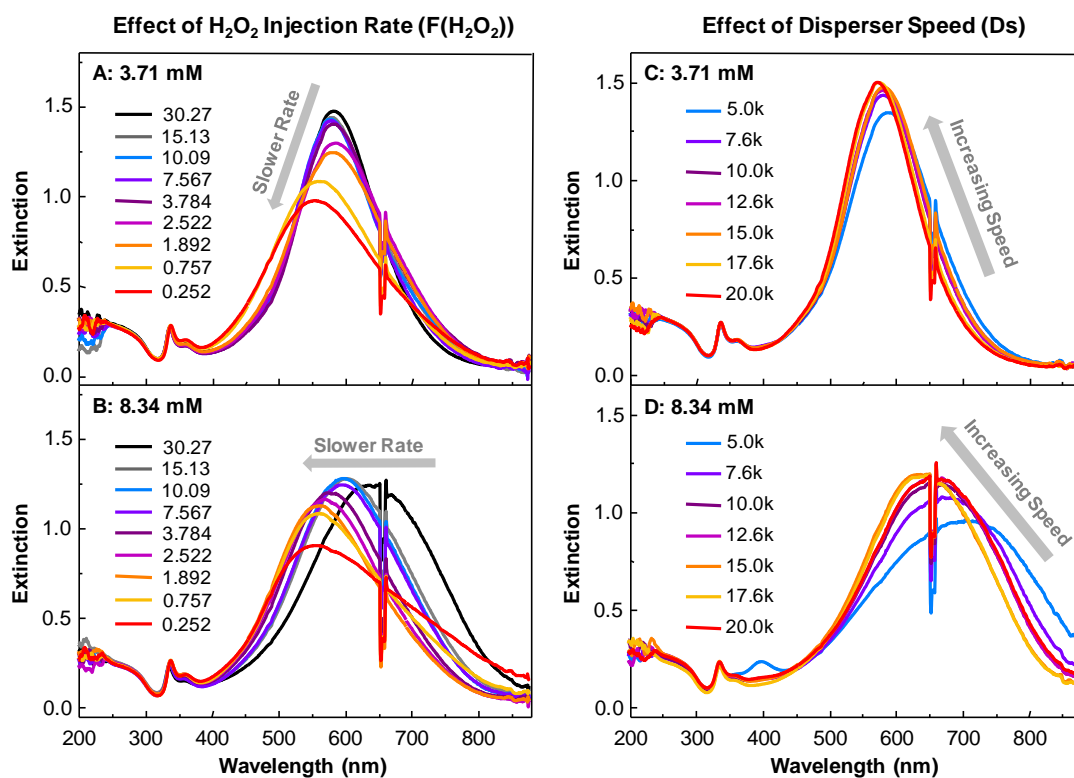
Figure 4.40   Effects of initial AgNSs concentration, H_2O_2 injection rates (mL/min) (A and B) and disperser speed (revolutions/min (rpm)) (C and D) on the formation of AgNPrs. [AgNSs] were 3.71 mM and 8.34 mM. The molar ratio R was 40. The initial volume of AgNSs colloid was 200 mL. In A and B, the disperser speed was set at 15k rpm while the injection rates were varied as indicated. In C and D, the injection rate was set at 30 mL/min while the disperser speed was varied as indicated.

Figure 4.40 shows the influences of [AgNSs], $F(H_2O_2)$, and Ds on the formation of AgNPrs. [AgNSs] is directly proportional to the amount of AgNPrs constructing units (i.e., planar twinned seeds and solubilized Ag^+ ions). AgNPrs with longer IPDPR wavelengths (i.e., AgNPrs with larger lateral dimensions) were obtained when higher [AgNSs] was employed for various $F(H_2O_2)$ and Ds (Figures 4.40 A–D and

Figures 4.41 A and D). [AgNSs] is the primary parameter for controlling dimensions and IPDPR of AgNPrs. Higher [AgNSs] also leads to the formation of AgNPrs with larger size distribution as evidenced in the larger full-width at half-maximum (FWHM) (Figures 4.41 C and F).

$F(H_2O_2)$ determines the available concentration of H_2O_2 for the shape transformation process. AgNPrs with longer IPDPR wavelengths were obtained when higher $F(H_2O_2)$ was employed (Figures 4.40 A and B and Figure 4.41 A). A greater H_2O_2 concentration promotes larger extent of AgNSs solubilization. Therefore, it is possible that fewer nucleation sites are available for AgNPrs growth leading to the formation of larger AgNPrs. At higher [AgNSs] of 8.34 mM, faster H_2O_2 injection rates lead to the formation of AgNPrs with larger size distribution as observed in the increasing FWHM (Figure 4.41 C). $F(H_2O_2)$ did not significantly affect the size distribution at [AgNSs] of 3.71 mM. However, when $F(H_2O_2)$ was less than 5 mL/min, an abrupt decrease in IPDPR intensities with an increase in FWHM were observed for both [AgNSs] (Figures 4.41 B and C).

Disperser speed (Ds) directly affects the local H_2O_2 concentration in the growth environment during the shape transformation process. High performance disperser was employed in order to rapidly achieve a uniform H_2O_2 distribution. It also assists the diffusion of H_2O_2 to the surface of AgNSs. The disperser speed did not significantly affect the lateral dimensions of obtained AgNPrs at [AgNSs] of 3.71 mM since the minor change of IPDPR position was observed when Ds increased from 5k to 20k rpm (Figure 4.40 C and Figure 4.41 D). Local H_2O_2 concentration greatly affects AgNSs consumption and growth at higher [AgNSs] of 8.34 mM. Residual DPR peak of AgNSs was observed when slow Ds was employed suggesting incomplete consumption of AgNSs during AgNPrs growth (Figure 4.40 D). Increasing Ds greatly improves AgNPrs yield and size distribution as observed in the stronger IPDPR intensities and narrower FWHM at both [AgNSs] (Figures 4.41 E and F).
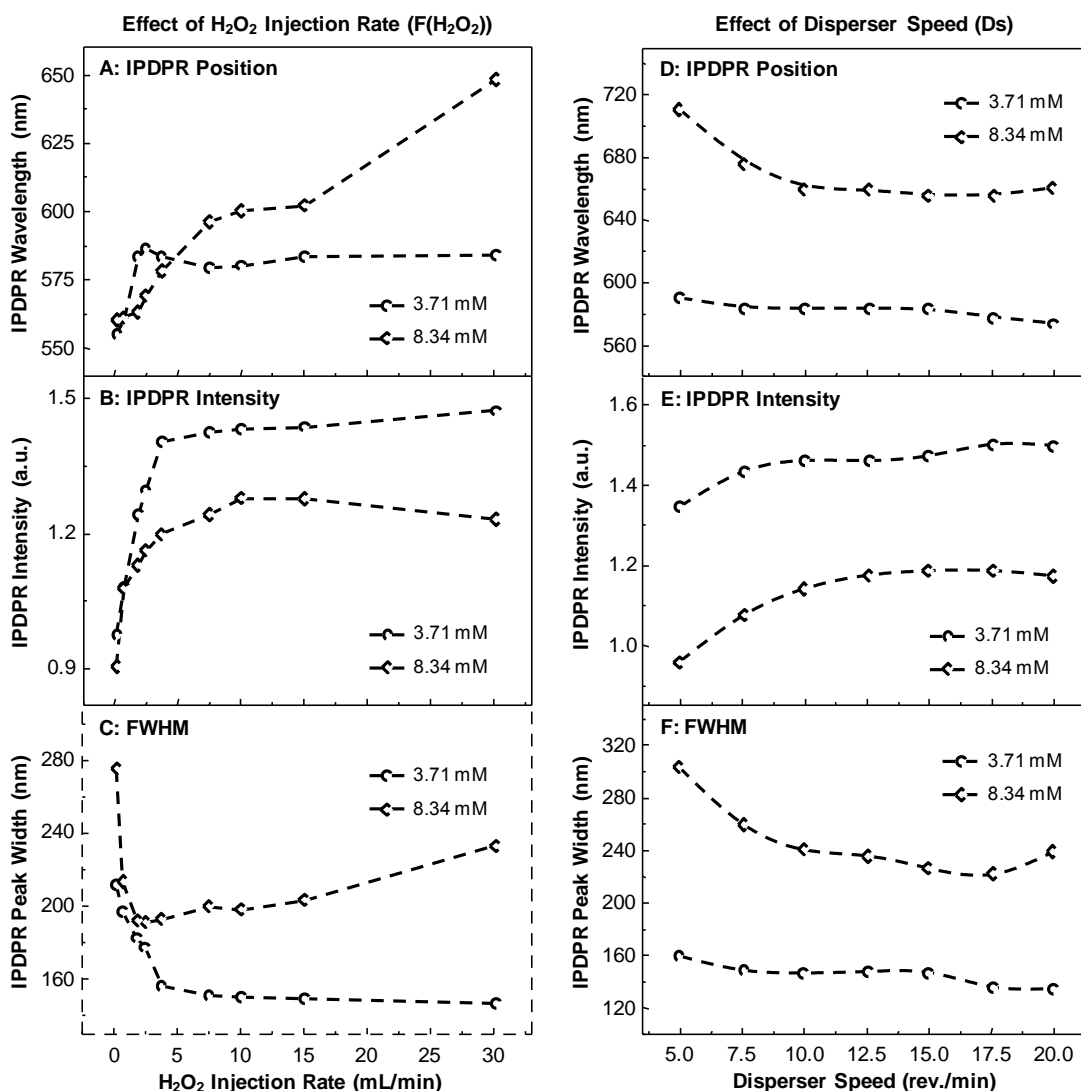
Figure 4.41 The effect of initial AgNSs concentration, H_2O_2 injection rates (F(H_2O_2)) (A–C) and disperser speed (Ds) (D–F) on IPDPR peak characteristics of AgNPrs: peak position (A and D), intensity (B and E), and full width at half maximum (FWHM) (C and F). Initial AgNSs concentrations were 3.71 mM and 8.34 mM. The experimental parameters are the same as indicated in Figure 4.40.

Upon a careful optimization of experimental parameters (i.e., [AgNSs], the mole ratio R, F(H_2O_2), and Ds) LSPR of the synthesized AgNPrs can be selectively tuned across the entire visible to near infrared (NIR) region (i.e., from 461 nm to 830 nm, Figure 4.42 and Table 4.4). The IPDPR of synthesized AgNPrs were redshifted from

461 nm to 830 nm, while the OPQPR were gradually blueshifted from 346 nm to 335 nm due to an increment of the aspect ratio [20, 22].
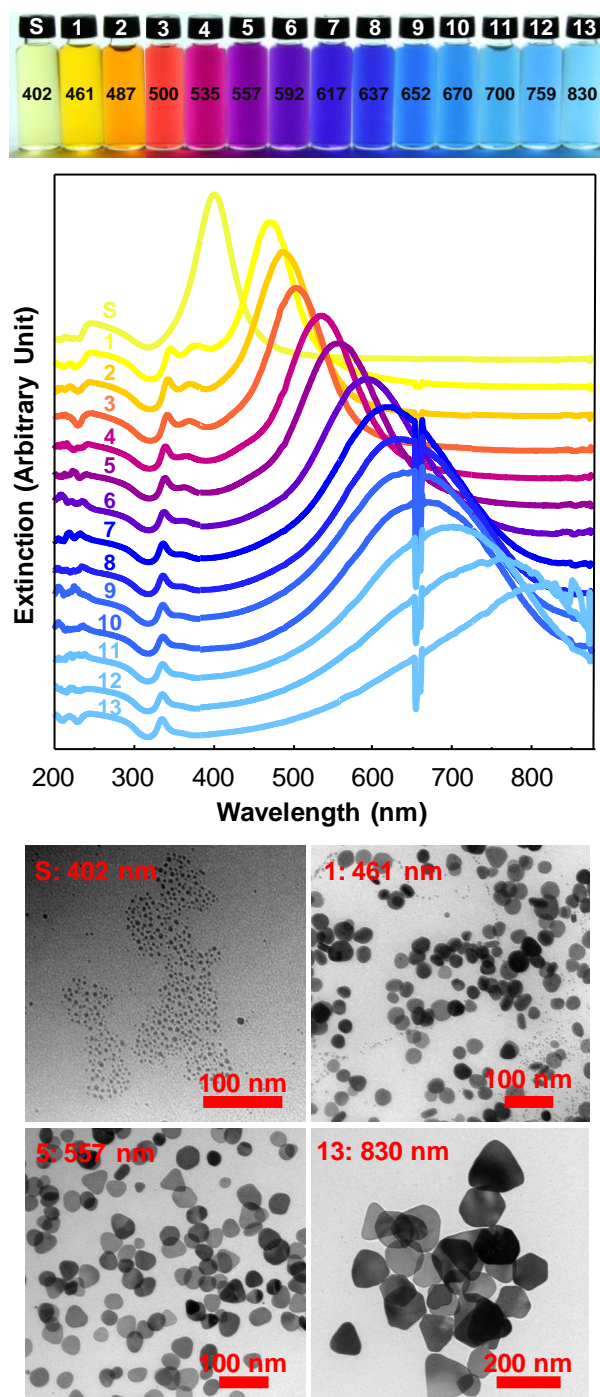
Figure 4.42   The photograph, plasmon extinction spectra, and TEM images of AgNSs (S) and the optically-tunable AgNPrs (1–13). The IPDPR peak positions (nm) of AgNPrs are also indicated.

Table 4.4   The optimal experimental parameters for synthesizing AgNPrs corresponding to the extinction spectra in Figure 4.42. AgNSs colloid of different concentration requires different concentration of H_2O_2 to optimally tune the LSPR wavelength across the visible region with a complete conversion of AgNSs to AgNPrs. A greater mole ratio R is required for a colloid with a greater concentration of AgNSs. A greater redshift of the IPDPR was obtained when colloid with a greater concentration of AgNSs was employed.

Exp No.	AgNSs Concentration	H_2O_2:AgNS (mole ratio)	H_2O_2 Flow Rates (mL/min)	OPQPR Wavelength (nm)	IPDPR Wavelength (nm)
1	100 ppm (0.927 mM)	20	25.22	346	461
2		5		342	487
3	200 ppm (1.854 mM)	20	10.09	341	500
4	300 ppm (2.781 mM)	20	5.045	339	535
5	400 ppm (3.708 mM)	30	13.45	338	557
6	500 ppm (4.635 mM)	30	18.92	337	592
7	600 ppm (5.562 mM)	40	22.70	336	617
8	700 ppm (6.489 mM)	40	35.31	336	637
9	800 ppm (7.416 mM)	40	40.36	336	652
10	900 ppm (8.344 mM)	40	56.75	336	670
11	1000 ppm (9.270 mM)	50	68.79	336	700
12	1100 ppm (10.198 mM)	70	69.36	335	759
13	1200 ppm (11.125 mM)	90	70.66	335	830

Figure 4.43   TEM micrographs of AgNPrs aligned edge-on to the electron beam. The sample numbers is corresponding to the extinction spectra of Figure 4.42. The out-of-plane quadrupole plasmon resonance (OPQPR) wavelengths are indicated.

The AgNPrs exhibited mixed geometries with average bisector lengths in the range of 30 to 120 nm (see TEM micrographs of Figure 4.42) The thickness of AgNPrs were in the range of 13 to 18 nm (Figure 4.43). The enlargement of the lateral length from 25 nm to 120 nm was also observed when the [AgNSs] increased (TEM micrographs of Figure 4.44). Total disappearance of the DPR at 400 nm suggests that AgNSs are 100% transformed to AgNPrs. The complete shape transformation without leaving any residual AgNSs/Ag$^+$ was already confirmed (Figure 4.35).

4.6 Applications of "Blue" AgNPrs in Antiseptic Wound Dressing

One of the interesting applications of AgNPrs is a colorful antibacterial agent. "Blue AgNPrs" (Figure 4.42 **13**) exhibit antibacterial activities against various tested bacteria (Tables 4.5–4.9 and Figure 4.44) with the minimum inhibition concentration of 5 ppm. Their beautiful blue color also reflects the sense of cleanness and safeness when applying in hygienic and antiseptic products.

Table 4.5   Antibacterial activity of "Blue" AgNPrs against *E. coli*.

| Sample | E. coli | | % Reduction |
| | CFU/mL | | |
	0 hr.	24 hr.	
Control (DDW)	2.40×10^6	1.00×10^6	58.333
Ag nano 1 ppm	2.40×10^6	$< 1.0 \times 10^1$	99.999
Ag nano 2.5 ppm	2.40×10^6	$< 1.0 \times 10^1$	99.999
Ag nano 5 ppm	2.40×10^6	$< 1.0 \times 10^1$	99.999
Ag nano 10 ppm	2.40×10^6	$< 1.0 \times 10^1$	99.999
Ag nano 20 ppm	2.40×10^6	$< 1.0 \times 10^1$	99.999

Table 4.6   Antibacterial activity of "Blue" AgNPrs against *S. aureus*.

| Sample | S. aureus | | % Reduction |
| | CFU/mL | | |
	0 hr.	24 hr.	
Control (DDW)	4.31×10^6	2.65×10^6	38.515
Ag nano 1 ppm	4.31×10^6	1.0×10^1	99.999
Ag nano 2.5 ppm	4.31×10^6	$< 1.0 \times 10^1$	99.999
Ag nano 5 ppm	4.31×10^6	$< 1.0 \times 10^1$	99.999
Ag nano 10 ppm	4.31×10^6	$< 1.0 \times 10^1$	99.999
Ag nano 20 ppm	4.31×10^6	$< 1.0 \times 10^1$	99.999

Table 4.7   Antibacterial activity of "Blue" AgNPrs against methicillin-resistant *S. aureus* (MRSA).

| Sample | MRSA | | % Reduction |
| | CFU/mL | | |
	0 hr.	24 hr.	
Control (DDW)	1.02×10^7	8.40×10^6	17.647
AgNPrs 1 ppm	1.02×10^7	4.15×10^2	99.995
AgNPrs 2.5 ppm	1.02×10^7	$< 1.0 \times 10^1$	99.999
AgNPrs 5 ppm	1.02×10^7	$< 1.0 \times 10^1$	99.999
AgNPrs 10 ppm	1.02×10^7	$< 1.0 \times 10^1$	99.999
AgNPrs 20 ppm	1.02×10^7	$< 1.0 \times 10^1$	99.999

Table 4.8   Antibacterial activity of "Blue" AgNPrs against *A. baumannii*.

Sample	A. baumannii		
	CFU/mL		% Reduction
	0 hr.	24 hr.	
Control (DDW)	2.26×10^6	1.54×10^6	31.858
Ag nano 1 ppm	2.26×10^6	$< 1.0 \times 10^1$	99.999
Ag nano 2.5 ppm	2.26×10^6	$< 1.0 \times 10^1$	99.999
Ag nano 5 ppm	2.26×10^6	$< 1.0 \times 10^1$	99.999
Ag nano 10 ppm	2.26×10^6	$< 1.0 \times 10^1$	99.999
Ag nano 20 ppm	2.26×10^6	$< 1.0 \times 10^1$	99.999

Table 4.9   Antibacterial activity of "Blue" AgNPrs against *P. aeruginosa*.

Sample	P. aeruginosa		
	CFU/mL		% Reduction
	0 hr.	24 hr.	
Control (DDW)	1.80×10^7	5.35×10^6	70.278
Ag nano 1 ppm	1.80×10^7	7.10×10^2	99.996
Ag nano 2.5 ppm	1.80×10^7	1.80×10^2	99.999
Ag nano 5 ppm	1.80×10^7	$< 1.0 \times 10^1$	99.999
Ag nano 10 ppm	1.80×10^7	$< 1.0 \times 10^1$	99.999
Ag nano 20 ppm	1.80×10^7	$< 1.0 \times 10^1$	99.999

Due to the high efficiency in antibacterial activities and the possibility of the mass-scale production of "Blue" AgNPrs, the licenses for production and characterization methods have been transferred to Novatec Healthcare, Co., Ltd. Novatec Healthcare is the Thai company dealing with medical devices and pharmaceutical products.
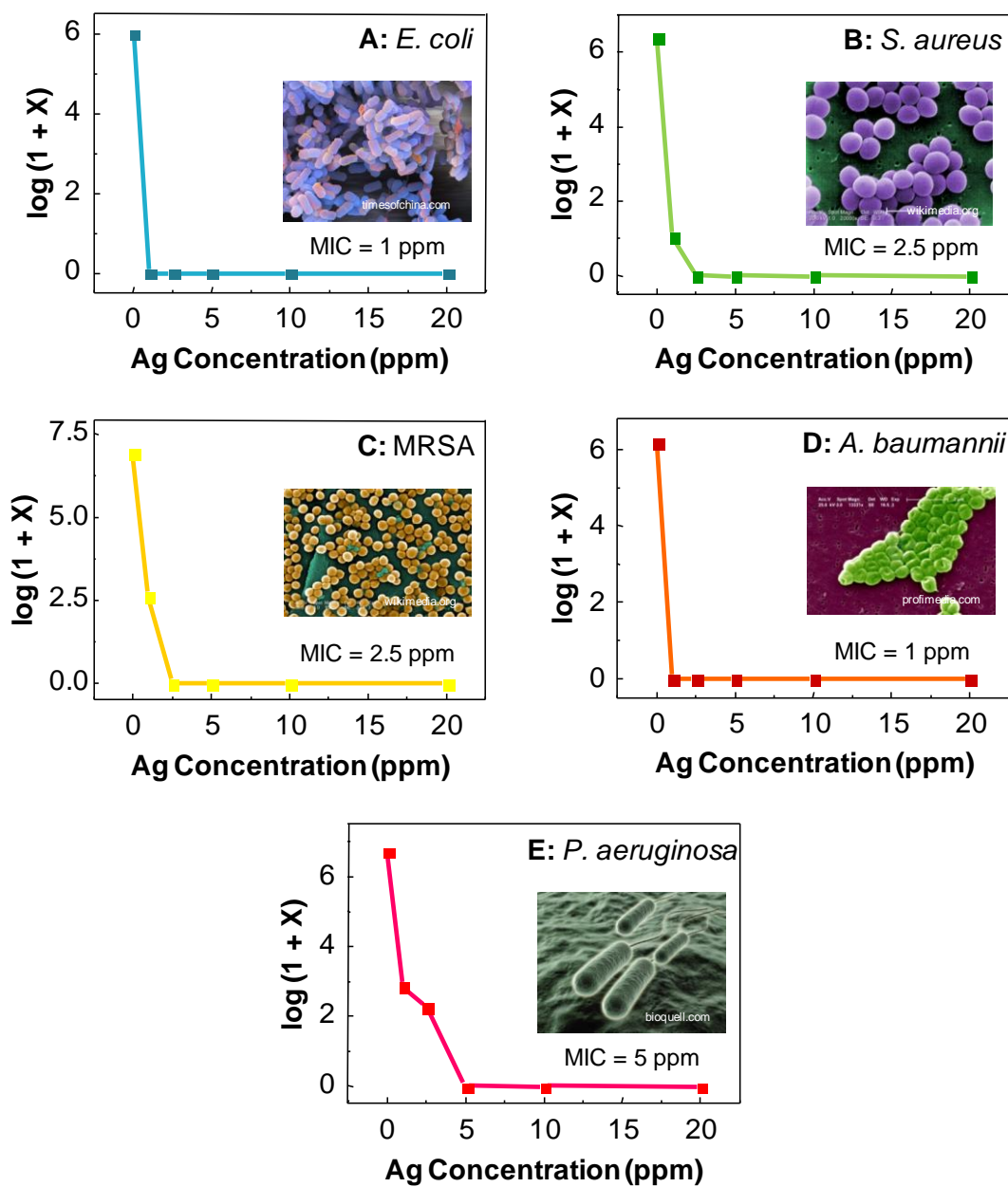
Figure 4.44   Antibacterial activities of "Blue" AgNPrs against *E. coli* (A), *S. aureus* (B), methicillin-resistant *S.aureus* (MRSA) (C), *A. baumannii* (D), and *P. aeruginosa* (E). The symbol "X" represents the bacterial colony forming units (CFU/mL) after the incubation with AgNPrs for 24 hours.

In particular, Novatec Healthcare applies the "Blue" AgNPrs for integrating in the moist wound dressing (Figure 4.45). The wound dressing mainly composes of nanobiocellulose fibers. The nanofibers are produced from bacterium *Acetobacter*

xylinum (Figure 4.46 B). The bacteria are cultivated in the cultured medium mainly composed of *Oryza sativa L.,* one of the Thai rice species (Figure 4.46 A). Entangling nanobiocellulose network is constructed from the primary nanofibers with average diameter of 80–100 nm (Figure 4.47 A). When "Blue" AgNPrs were immobilized in the entangling network, they were uniformly distributed and physically adsorbed onto the nanobiocellulose fibers (Figure 4.47 B).

Figure 4.45 Moist antiseptic wound dressing products (BluRibbon^TM, BluMembrane^TM, and BluTulle^TM) offered by Novatec Healthcare Co., Ltd.
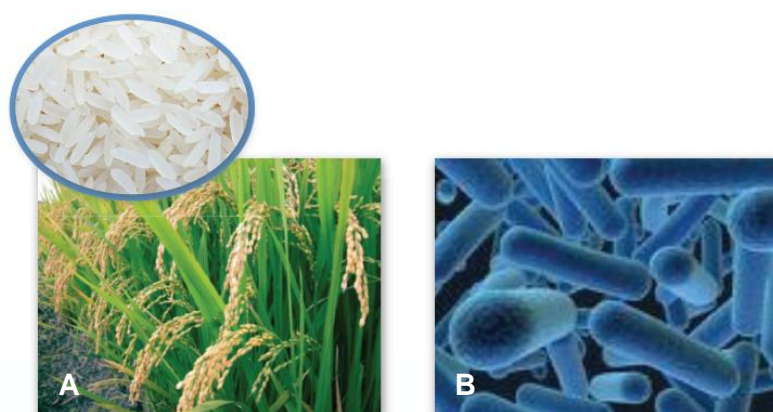
Figure 4.46 *Oryza sativa L.* (A) and bacterium *Acetobacter xylinum* (B).
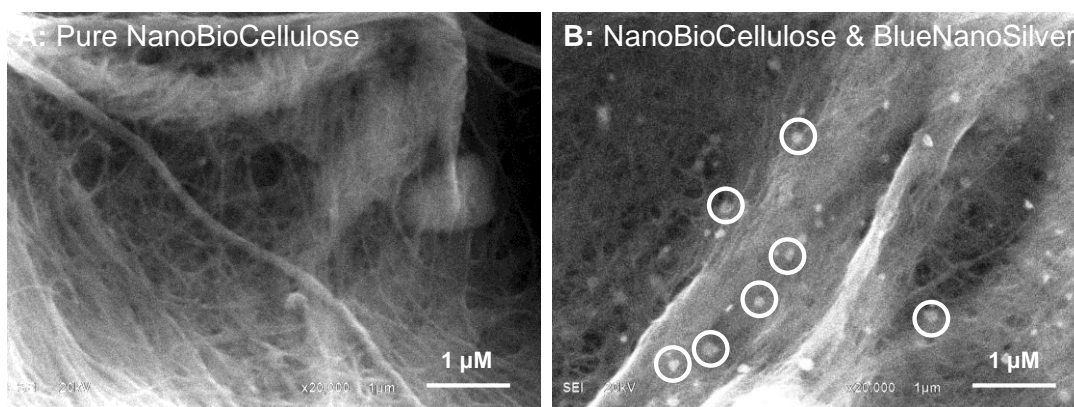
Figure 4.47 SEM micrograph of virgin nanobiocellulose fibers (A) and "Blue" AgNPrs-immobilized nanobiocellulose fibers (B).

Nanobiocellulose wound dressing exhibit superior properties for accelerating wound recovery including: (1) maintain moist wound environment; (2) possess auto-debridement activity; (3) significantly reduce pain and inflammation; (4) easy and painless removal; (5) thin, tough, but gentle to wound bed; (6) nontoxic, nonpyrogenic, and biocompatible; etc.

The extraordinary property of the developed Blue AgNPrs-immobilized wound dressing is the on-demand releasing of nanosilver. In addition, the blue color represents its action indicator. Blue color will be faded-off and turned to yellow automatically due to the disintegration of AgNPrs to Ag^+ during the antibacterial action. This feature greatly assists the decision making of the doctors and nurses for appropriate interval of the new dressing (Figure 4.48).

The BluRibbon^{TM} wound dressing was clinically proved effective for cavity wounds (Figure 4.49), dog bite wounds (Figure 4.50), diabetic callus wounds (Figure 4.51), and other acute and chronic wounds.
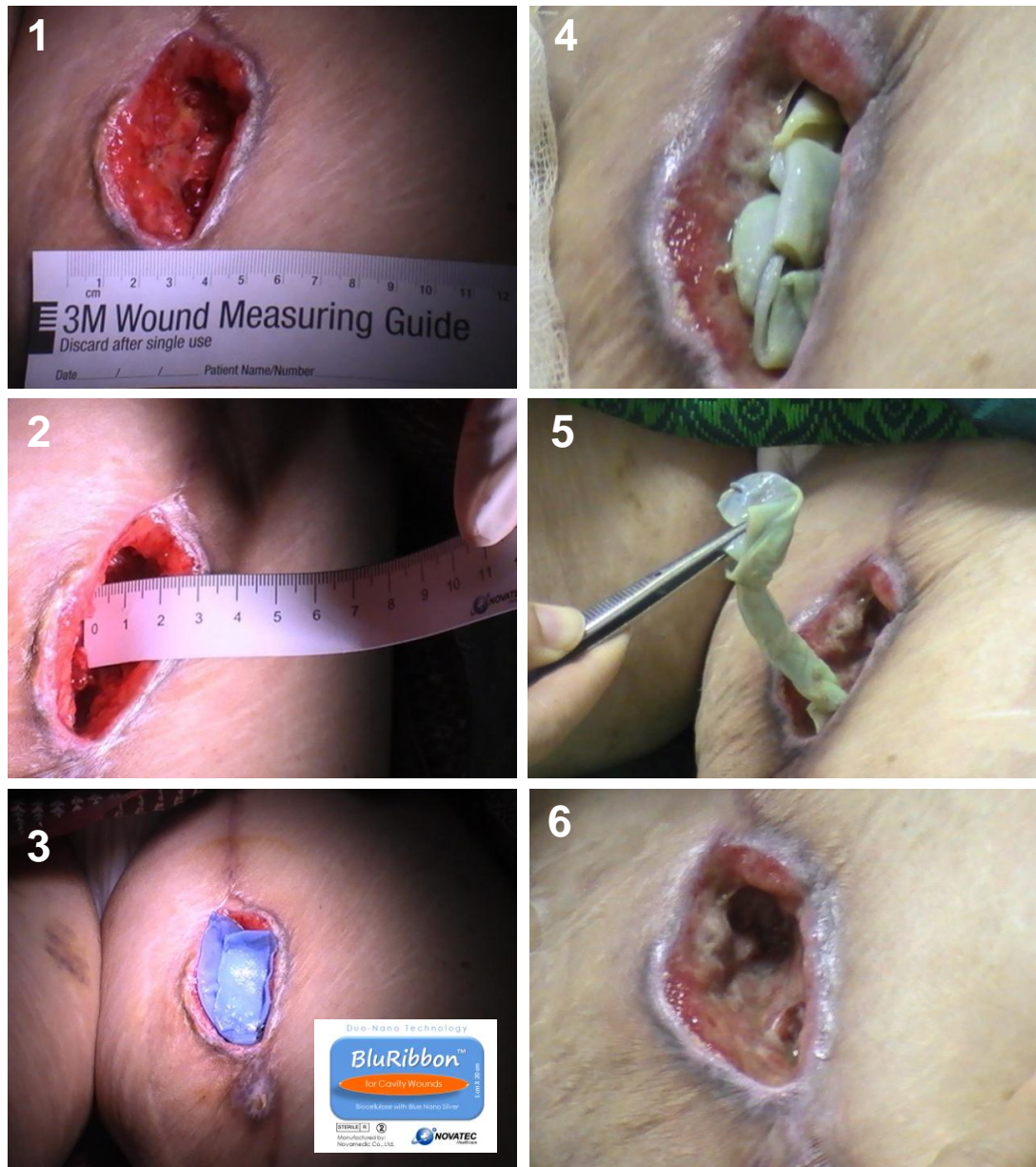
Figure 4.48   Self-indication property of BluRibbon^{TM} on the treatment of cavity wound.
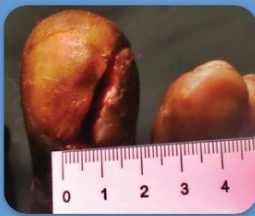
Figure 4.49   Clinical trial for BluRibbon[TM] on the treatment of cavity wound.
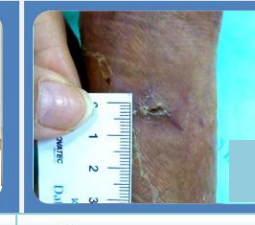
Figure 4.50   Clinical trials for BluRibbon[TM] on the treatment of dog bite wounds.
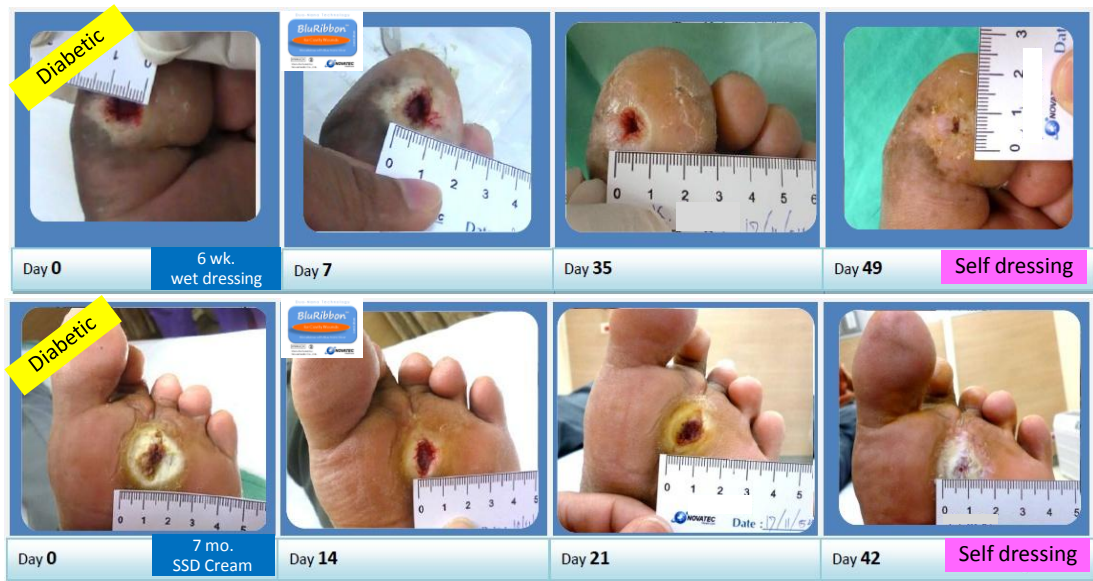
Figure 4.51   Clinical trials for BluRibbon^{TM} on the treatment of diabetic callus wounds.

CHAPTER V

CONCLUSIONS

The utilization of reduction capability of H_2O_2 under its oxidative environment is never been reported, albeit the employment of H_2O_2 in this kind of reaction is not new. This unique feature exists only under a small window of experimental design. We have found and explored this window. Moreover, our process is simpler, faster, the reaction occurs without a latent period. This work is novel with a creative application of H_2O_2 as the reducing agent under its own oxidative environment. In addition, spectrophotometric method combined with the chemometric analysis of plasmon extinction spectra has a potential to reveal the structural evolution process as observed by surface plasmon resonance phenomena. The evolution profiles show that the spherical Ag particles were systematically evolved into plate structures of different sizes. The larger nanoplates were obtained when higher concentration of H_2O_2 was employed. An evidence of nanoplate disintegration was observed when the large amount of H_2O_2 was employed. The predicted structural morphologies of each component given by chemometric calculation were in excellent agreement with those observed by transmission electron microscope (TEM) images.

We have explored some unique features that have not been mentioned before in other AgNPrs synthesis utilizing H_2O_2 including:

(i) The shape transformation process is starting with metallic nanosilver species (AgNSs) instead of solubilized Ag^+. Soluble starch, a steric stabilizer, is utilized as the sole stabilizer for AgNSs without employing any additional surface binding ligand e.g. citrate and PVP.

(ii) The shape transformation process is initiated after H_2O_2 is injected into AgNSs colloid. The total dissolution of nanometallic Ag to Ag^+ by oxidative etching of H_2O_2 and the final injection of strong reducing agent e.g. $NaBH_4$ to initiate the prism growth are not necessary.

(iii) Additional Ag^+ is not required. AgNSs plays the role both as new nucleation site after modification with H_2O_2 and solubilized Ag^+ source (as a consequence from the etching process).

(iv) H_2O_2 plays the role of reducing agent in our system. Additional reducing agent is not required in our system.

(v) Oxidation and reduction capabilities of H_2O_2 are coordinated through the optimization of pH of the reaction medium. H_2O_2 plays both roles under the same experimental condition, but not the same Ag species. H_2O_2 exhibits the oxidizing function when reacted with metallic Ag. It functions as reducing species when reacted with the available Ag^+.

(vi) Capping agents are not required for promoting the anisotropic growth.

(vii) Particle evolution process is proposed based on the experimental evidences and the theoretical calculations.

5.1 Chemical Shape Transformation of AgNSs-to-AgNPrs triggered by H_2O_2

A practical procedure for a morphological transformation of AgNSs to AgNPrs utilizing H_2O_2 is demonstrated. The spontaneous transformation was initiated by feeding H_2O_2 into starch-stabilized AgNSs colloid without additional silver ions, reducing agents, and capping agents. AgNSs function as the planar twinned seed supplier and internal Ag^+ source. The small diameter of AgNSs is one of the crucial factors for the shape transformation to be possible. Starch is employed as the sole steric stabilizer for AgNSs and AgNPrs. It does not function as a reducing agent under our experimental conditions as confirmed by FT-IR spectroscopy. Complexation between starch and Ag^+ prevents the formation of Ag_2O under a mild alkaline condition. H_2O_2 functions as a facet-selective etchant toward metallic Ag species and as reducing species toward Ag^+ (under the same experimental condition). Mild reducing capability of H_2O_2 and limited number of Ag atoms mediated by Ag^+-starch complex exert the kinetically controlled growth for AgNPrs development. The inherent defects presented in the oxidatively etched AgNSs govern the development of planar nanostructure. In our protocol, citrate prohibited the AgNSs-to-AgNPrs transformation.

The transformation reaction is spontaneous and rapid. The reaction progress can be visualized in real time with naked eyes via the color change of the colloidal suspension after the addition of H_2O_2. The initial AgNSs concentration, H_2O_2:AgNSs mole ratio, H_2O_2 injection rate, and mixing efficiency are the key parameters for selective tuning the optical properties, improving the yield and size monodispersity of the AgNPrs. Highly concentrated AgNPrs (0.9–11 mM) with controllable IPDPR from the visible to NIR region can be synthesized. The synthesized AgNPrs are stable under the prolonged storage of at least 3 months. Our findings demonstrate the phenomena on pH-mediated coordination of the oxidative facet selective etching, mild reducing capability, and decomposition reaction of H_2O_2 for manipulating the metallic crystal at the nanoscale. We hope that our observations will stipulate the exploitation of H_2O_2 as a shape-controlling agent in the fabrication of more complex nanostructures.

5.2 Chemometric Analysis of Spectroscopic Data on AgNSs-to-AgNPrs Shape Evolution Induced by Hydrogen Peroxide

The study on the shape evolution of metal nanoparticles (MNPs) is crucial to gain an understanding on controlling the shape and size of metal nanostructures. The evolution process of Ag sphere-to-plate induced by hydrogen peroxide was revealed by chemometric analysis of the UV-visible plasmonic extinction spectra. The number of major components contributed in the evolution systems was accurately determined, as confirmed by TEM measurement. By MCR-ALS analysis, the concentration profile provides the exact experimental conditions to be selected for further structural investigation. Five major components attributed to the different particle shapes and sizes were theoretically predicted. The characteristic of size and shape (sphere and plate) were revealed by the pure spectra which are interpreted according to the results obtained by an image analysis. The shape transformation of AgNSs to AgNPrs induced by H_2O_2 can be divided into 3 states, namely, the AgNSs-to-AgNPrs transformation, AgNPrs-to-AgNPrs reformation, and disintegration. However, to chemometricallly discriminate the different plate morphologies (e.g. circular disc, triangular, truncated triangular, hexagonal, and polygonal), the selective synthetic

experiments are required. The results from the calculated evolution profiles were in good agreement with the observed TEM images. The procedure was powerful and accurate which exhibits all hidden information without a requirement of extensive laboratory measurements. Because of the simplicity, the low operating cost, and the rapid spectrophotometric measurements, the proposed procedure opens up a new insight to the study of metal nanoparticle evolution. Moreover, using this technique in the synthesis of MNPs opens a great opportunity to investigate the kinetics of detailed reactions. Time-dependent extinction spectra of MNPs during the synthesis could also be analysed by MCR-ALS to obtain the concentration profiles against reaction time, and their kinetics and elementary processes could be reliably proposed.

5.3 Application of AgNPrs on Antiseptic Medical Devices

"Blue AgNPrs" exhibit antibacterial activities against various tested bacteria with the minimum inhibition concentration of 5 ppm. In cooperation with Novatec Healthcare Co., Ltd., we have developed the moist wound dressing integrating the Engineered NanoSilver Technology and NanoBioCelluose Technology. The developed wound dressings (BluRibbon^{TM}) have been clinically proved effective for various severe, acute, and chronic wounds. The developed wound dressing exhibits the extraordinary properties on accelerating wound recovery and self-indicating system. The development of the novel wound dressing significantly represents the milestone of Nanomedicine in Thailand.

REFERENCES

[1]   Millstone, J. E.; Hurst, S. J.; Métraux, G. S.; Cutler, J. I.; and Mirkin, C. A. Colloidal Gold and Silver Triangular Nanoprisms. Small 5 (2009): 646–664.

[2]   Pastoriza-Santos, I.; and Liz-Marzán, L. M. Colloidal Silver Nanoplates: State of the Art and Future Challenges. J. Mater. Chem. 18 (2008): 1724–1737.

[3]   Xue, C.; and Mirkin C. A. pH-Switchable Silver Nanoprism Growth Pathways. Angew. Chem., Int. Ed. 46 (2007): 2036–2038.

[4]   Lee, B. H.; Hsu, M. S.; Hsu, Y. C.; Lo, C. W.; and Huang, C. L. A Facile Method To Obtain Highly Stable Silver Nanoplate Colloids with Desired Surface Plasmon Resonance Wavelengths. J. Phys. Chem. C 114 (2010): 6222–6227.

[5]   Aherne, D.; Ledwith, D. M.; Gara, M.; and Kelly, J. M. Optical Properties and Growth Aspects of Silver Nanoprisms Produced by a Highly Reproducible and Rapid Synthesis at Room Temperature. Adv. Funct. Mater. 18 (2008): 2005–2016.

[6]   Kazuma, E.; Matsubara, K.; Kelly, K. L.; Sakai N.; and Tatsuma, T. Bi- and Uniaxially Oriented Growth and Plasmon Resonance Properties of Anisotropic Ag Nanoparticles on Single Crystalline TiO_2 Surfaces. J. Phys. Chem. C 113 (2009): 4758–4762.

[7]   Yamaguchi, K.; Inoue, T.; Fujii, M.; Ogawa, T.; Matsuzaki, Y.; Okamoto, T.; Haraguchi, M.; and Fukui, M. Characteristics of Light Intensity Enhancement of a Silver Nanoprism with Rounded Corners. J. Microsc. 229 (2008): 545–550.

[8]   Zhang, Q.; Hu, Y.; Guo, S.; Goebl, J.; and Yin, Y. Seeded Growth of Uniform Ag Nanoplates with High Aspect Ratio and Widely Tunable Surface Plasmon Bands. Nano Lett. 10 (2010): 5037–5042.

[9]   Haynes, C. L.; Yonzon, C. R.; Zhang, X.; and Van Duyne, R. P. Surface-Enhanced Raman Sensors: Early History and the Development of Sensors for Quantitative Biowarfare Agent and Glucose Detection. <u>J. Raman Spectrosc.</u> 36 (2005): 471–484.

[10]   McFarland, A. D.; Young, M. A.; Dieringer, J. A.; and Van Duyne, R. P. Wavelength-Scanned Surface-Enhanced Raman Excitation Spectroscopy. <u>J. Phys. Chem. B</u> 109 (2005): 11279–11285.

[11]   Haynes, C. L.; McFarland, A. D.; and Van Duyne, R. P. Surface-Enhanced Raman Spectroscopy. <u>Anal. Chem.</u> 2005: 338–346.

[12]   Jana, N. R.; and Pal, T. Anisotropic Metal Nanoparticles for Use as Surface-Enhanced Raman Substrates. <u>Adv. Mater.</u> 19 (2007): 1761–1765.

[13]   Ciou, S. H.; Cao, Y. W.; Huang, H. C.; Su, D. Y.; and Huang, C. L. SERS Enhancement Factors Studies of Silver Nanoprism and Spherical Nanoparticle Colloids in the Presence of Bromide Ions. <u>J. Phys. Chem. C</u> 113 (2009): 9520–9525.

[14]   Cathcart, N.; and Kitaev, V. Monodisperse Hexagonal Silver Nanoprisms: Synthesis *via* Thiolate-Protected Cluster Precursors and Chiral, Ligand-Imprinted Self Assembly. <u>ACS Nano</u> 5 (2011): 7411–7425.

[15]   Gao, C.; Lu, Z.; Liu, Y.; Zhang, Q.; Chi, M.; Cheng, Q.; and Yin, Y. Highly Stable Silver Nanoplates for Surface Plasmon Resonance Biosensing. <u>Angew. Chem., Int. Ed.</u> 51 (2012): 5629–5633.

[16]   Haes, A. J.; and Van Duyne, R. P. A Nanoscale Optical Biosensors: Sensitivity and Selectivity of an Approach Based on the Localized Surface Plasmon Resonance Spectroscopy of Triangular Silver Nanoparticles. <u>J. Am. Chem. Soc.</u> 124 (2002): 10596–10604.

[17]   Haes, A. J.; Haynes, C. L.; McFarland, A. D.; Schatz, G. C.; Van Duyne, R. P.; and Zou, S. Plasmonic Materials for Surface-Enhanced Sensing and Spectroscopy. <u>MRS Bull.</u> 30 (2005): 368–375.

[18]   Zhao, J.; Zhang, X.; Yonzon, C. R.; Haes, A. J.; and Van Duyne, R. P. Localized Surface Plasmon Resonance Biosensors. <u>Nanomedicine</u> 1 (2006): 219–228.

[19]   Sherry, L. J.; Jin, R.; Mirkin, C. A.; Schatz, G. C.; and Van Duyne, R. P.
         Localized Surface Plasmon Resonance Spectroscopy of Single Silver
         Triangular Nanoprisms. <u>Nano Lett.</u> 6 (2006): 2060–2065.

[20]   Kelly, K. L.; Coronado, E.; Zhao, L. L.; and Schatz, G. C. The Optical
         Properties of Metal Nanoparticles: The Influence of Size, Shape, and
         Dielectric Environment. <u>J. Phys. Chem. B</u> 107 (2003): 668–677.

[21]   Hao, E.; and Schatz, G. C. Electromagnetic Fields around Silver
         Nanoparticles and Dimers. <u>J. Chem. Phys.</u> 120 (2004): 357–366.

[22]   Brioude, A.; and Pileni, M. P. Silver Nanodisks: Optical Properties Study
         Using the Discrete Dipole Approximation Method. <u>J. Phys. Chem. B</u>
         109 (2005): 23371–23377.

[23]   Wiley, B. J.; Im, S. H.; Li, Z. Y.; McLellan, J.; Siekkinen, A.; and Xia, Y.
         Maneuvering the Surface Plasmon Resonance of Silver Nanostructures
         through Shape-Controlled Synthesis. <u>J. Phys. Chem. B</u> 110 (2006): 668–
         677.

[24]   Jin, R.; Cao, Y.; Mirkin, C. A.; Kelly, K. L.; Schatz, G. C.; and Zheng, J. G.
         Photoinduced Conversion of Silver Nanospheres to Nanoprisms. <u>Science</u>
         294 (2001): 1901–1903.

[25]   Jin, R.; Cao, Y. C.; Hao, E.; Métraux, G. S.; Schatz, G. C.; and Mirkin, C. A.
         Controlling Anisotropic Nanoparticle Growth Through Plasmon
         Excitation. <u>Nature</u> 425 (2003): 487–490.

[26]   Xue, C.; Métraux, G. S.; Millstone, J. E.; and Mirkin, C. A. Mechanistic
         Study of Photomediated Triangular Silver Nanoprism Growth. <u>J. Am.
         Chem. Soc.</u> 130 (2008): 8337–8344.

[27]   Sun, Y.; and Xia, Y. Triangular Nanoplates of Silver: Synthesis,
         Characterization, and Use as Sacrificial Templates for Generating
         Triangular Nanorings of Gold. <u>Adv. Mater.</u> 15 (2003): 695–699.

[28]   Tang, B.; Xu, S.; An, J.; Zhao, B.; and Xu, W. Photoinduced Shape
         Conversion and Reconstruction of Silver Nanoprisms. <u>J. Phys. Chem. C</u>
         113 (2009): 7025–7030.

[29]   Bastys, V.; Pastoriza-Santos, I.; Rodríguez-González, B.; Vaisnoras, R.; and Liz-Marzán, L. M. Formation of Silver Nanoprisms with Surface Plasmons at Communication Wavelengths. Adv. Funct. Mater. 16 (2006): 766–773.

[30]   Gentry, S. T.; and Levit, S. D. Stochastic Control: Transition from Differentiated to Undifferentiated Kinetic Growth in Ag Nanoprisms. J. Phys. Chem. C 113 (2009): 12007–12015.

[31]   Zou, X.; Ying, E.; Chen, H.; and Dong, S. An Approach for Synthesizing Nanometer- to Micrometer-Sized Silver Nanoplates. Colloids Surf. A Physicochem. Eng. Aspects 303 (2007): 226–234.

[32]   Gentry, S. T.; Kendra, S. F.; and Bezpalko, M. W. Ostwald Ripening in Metallic Nanoparticles: Stochastic Kinetics. J. Phys. Chem. C 115 (2011): 12736–12741.

[33]   Ledwith, D. M.; Whelan, A. M.; and Kelly, J. M. A Rapid, Straight-Forward Method for Controlling the Morphology of Stable Silver Nanoparticles. J. Mater. Chem. 17 (2007): 2459–2464.

[34]   Goebl, J.; Zhang, Q.; He, L.; and Yin, Y. Monitoring the Shape Evolution of Silver Nanoplates: A Marker Study. Angew. Chem., Int. Ed. 51(2012): 522–555.

[35]   Zeng, J.; Xia, X.; Rycenga, M.; Henneghan, P.; Li, Q.; and Xia, Y. Successive Deposition of Silver on Silver Nanoplates: Lateral versus Vertical Growth. Angew. Chem., Int. Ed. 50 (2011): 244–249.

[36]   Tang, B.; An, J.; Zheng, X.; Xu, S.; Li, D.; Zhou, J.; Zhao, B.; and Xu, W. Silver Nanodisks with Tunable Size by Heat Aging. J. Phys. Chem. C 112 (2008): 18361–18367.

[37]   Tsai, C. M.; Hsu, M. S.; Chen, J. C.; and Huang, C. L. Mechanistic Study of Shape Evolution of Silver Nanoprisms in The Presence of KSCN. J. Phys. Chem. C 116 (2012): 461–467.

[38]   Cathcart, N.; Frank, A. J.; and Kitaev, V. Silver Nanoparticles with Planar Twinned Defects: Effect of Halides for Precise Tuning of Plasmon Resonance Maxima from 400 to >900 nm. Chem. Commun. 46 (2009): 7170–7172.

[39]   Zhang, Q.; Ge, J.; Pham, T.; Goebl, J.; Hu, Y.; Lu, Z.; and Yin, Y. Reconstruction of Silver Nanoplates by UV Irradiation: Tailored Optical Properties and Enhanced Stability. Angew. Chem., Int. Ed. 48 (2009): 3516–3519.

[40]   Pastoriza-Santos, I.; and Liz-Marzán, L. M. Synthesis of Silver Nanoprisms in DMF. Nano Lett. 2 (2002): 903–905.

[41]   Pastoriza-Santos, I.; and Liz-Marzán, L. M. N,N-Dimethylformamide as a Reaction Medium for Metal Nanoparticle Synthesis. Adv. Funct. Mater. 19 (2009): 679–688.

[42]   Chen, S.; and Carroll, D. L. Synthesis and Characterization of Truncated Triangular Silver Nanoplates. Nano Lett. 2 (2002): 1003–1007.

[43]   Chen, S.; Fan, Z.; and Carroll, D. L. Silver Nanodisks: Synthesis, Characterization, and Self-Assembly. J. Phys. Chem. B 106 (2002): 10777–10781.

[44]   Washio, I.; Xiong, Y.; Yin, Y.; and Xia, Y. Reduction by the End Groups of Poly(vinyl pyrrolidone): A New and Versatile Route to the Kinetically Controlled Synthesis of Ag Triangular Nanoplates. Adv. Mater. 18 (2006): 1745–1749.

[45]   Sun, Y.; Mayers, B.; and Xia, Y. Transformation of Silver Nanospheres into Nanobelts and Triangular Nanoplates through a Thermal Process. Nano Lett. 3 (2003): 675–679.

[46]   Xiong, Y.; Washio, I.; Chen, J.; Sadilek, M.; and Xia, Y. Trimetric Clusters of Silver in Aqueous $AgNO_3$ Solutions and Their Role as Nuclei in Forming Triangular Nanoplates of Silver. Angew. Chem., Int. Ed. 46 (2007): 4917–4921.

[47]   Xiong, Y.; Siekkinen, A. R.; Wang, J.; Yin, Y.; Kim, M. J.; and Xia, Y. Synthesis of Silver Nanoplates at High Yields by Slowing Down the Polyol Reduction of Silver Nitrate with Polyacrylamide. J. Mater. Chem. 17 (2007): 2600–2602.

[48] Liu, Z.; Zhou, H.; Lim, Y. S.; Song, J. H.; Piao, L.; and Kim, S. H. Synthesis of Silver Nanoplates by Two-Dimensional Oriented Attachment. Langmuir 28 (2012): 9244–9249.

[49] Cao, Z.; Fu, H.; Kang, L.; Huang, L.; Zhai, T.; Ma, Y.; and Yao, J. Rapid Room − Temperature Synthesis of Silver Nanoplates with Tunable In − Plane Surface Plasmon Resonance from Visible to Near-IR. J. Mater. Chem. 18 (2008): 2673–2678.

[50] Sau, T. K.; and Rogach, A. L. Nonspherical Noble Metal Nanoparticles: Colloid-Chemical Synthesis and Morphology Control. Adv. Mater. 22 (2010): 1781–1804.

[51] Métraux, G. S.; and Mirkin, C. A. Rapid Thermal Synthesis of Silver Nanoprisms with Chemically Tailorable Thickness. Adv. Mater. 17 (2005): 8337–8344.

[52] Zhang, Q.; Li, N.; Goebl, J.; Lu, Z.; and Yin, Y. A Systematic study of the Synthesis of Silver Nanoplates: Is Citrate a "Magic" Reagent". J. Am. Chem. Soc. 133 (2011): 18931–18939.

[53] Tsuji, M.; Gomi, S.; Maeda, Y.; Matsunaga, M.; Hikino, S.; Uto, K.; Tsuji, T.; and Kawazumi, H. Rapid Transformation from Spherical Nanoparticles, Nanorods, Cubes, or Bipyramids to Triangular Prisms of Silver with PVP, Citrate, and H_2O_2. Langmuir 28 (2012): 8845–8861.

[54] Li, N.; Zhang, Q.; Quinlivan, S.; Goebl, J.; Gan, Y.; and Yin, Y. H_2O_2-Aided Seed-Mediated Synthesis of Silver Nanoplates with Improved Yield and Efficiency. Chem. Phys. Phys. Chem. 13 (2012): 2526–2530.

[55] Kilin, D. S.; Prezhdo, O. V.; and Xia, Y. Shape-Controlled Synthesis of Silver Nanoparticles: *Ab Initio* Study of Preferential Surface Coordination with Citric Acid. Chem. Phys. Lett. 458 (2008): 113–116.

[56] Cobley, C. M.; Rycenga, M.; Zhou, F.; Li, Z. Y.; and Xia, Y. Controlling Etching as a Route to High Quality Silver Nanospheres for Optical Studies. J. Phys. Chem. C 113 (2009): 16975–16982.

[57] Panda, B. R.; and Chattopadhyay, A. Synthesis of Au Nanoparticles at "all" pH by H_2O_2 Reduction of $HAuCl_4$. J. Nanosci. Nanotechnol. 7 (2007): 1911–1915.

[58]   Sarma, T. K.; Chowdhury, D.; Paul, A.; and Chattopadhyay, A. Synthesis of Au nanoparticle–conductive polyaniline composite using H_2O_2 as oxidising as well as reducing agent. Chem. Commun. 2002: 1048–1049.

[59]   Sarma, T. K.; and Chattopadhyay, A. Starch-Mediated Shape Selective Synthesis of Au Nanoparticles with Tunable Longitudinal Plasmon Resonance. Langmuir, 20 (2004): 3520–3524.

[60]   Liu, X.; Xu, H.; Xia, H.; and Wang, D. Rapid Seeded Growth of Monodisperse, Quasi-Spherical, Citrate-Stabilized Gold Nanoparticles via H_2O_2 Reduction. Langmuir 28 (2012): 13720–13726.

[61]   Wang, L.; Wang, F.; Shang, L.; Zhu, C.; Ren, W.; and Dong, S. AuAg Bimetallic Nanoparticles Film Fabricated Based On H_2O_2-Mediated Silver Reduction and its Application. Talanta 82 (2010): 113–117.

[62]   Gole, A.; and Murphy, C. J. Seed-Mediated Synthesis of Gold Nanorods: Role of the Size and Nature of the Seeds. Chem. Mater. 16 (2004): 3633–3640.

[63]   http://rsb.info.nih.gov/ij (accessed 16/10/2010).

[64]   Bulmer, J. T.; and Shurvell, H. F. Factor Analysis as a Complement to Band Resolution Techniques. II. Pseudo-Isosbestic Point in the Chloroform-*d*-Di-*n*-butyl Ether System. *J. Phys. Chem.*, 77 (1973): 2085–2090.

[65]   Ho, C. M.; King-Woon Yau, S.; Lok, C. N.; So, M. H.; and Che, C. M. Oxidative Dissolution of Silver Nanoparticles by Biologically Relevant Oxidants: A Kinetic and Mechanistic Study. Chem-Asian J. 5 (2010): 285–293.

[66]   Weiss, J. The Catalytic of Hydrogen Peroxide on Different Metals. Trans. Faraday Soc. 31 (1935): 1547–1557.

[67]   Maggs, F. T.; and Sutton, D. Some Aspects of the Catalytic Decomposition of Concentrated Hydrogen Peroxide by Silver. Part 1.-The Solubility and Rate of Solution of Silver. Trans. Faraday Soc. 54 (1958): 1861–1870.

[68]   Maggs, F. T.; and Sutton, D. Some Aspects of the Catalytic Decomposition of Concentrated Hydrogen Peroxide by Silver. Part 2.-Electrical Conductivity and pH of Solutions of Hydrogen Peroxide Containing Silver. Trans. Faraday Soc. 55 (1959): 974–980.

[69]   Holst, G. The Chemistry of Bleaching and Oxidizing Agents. <u>Chem. Rev.</u> 54 (1954): 169–194.

[70]   Shanley, E. S.; and Greenspan, F. P. Highly Concentrated Hydrogen Peroxide. <u>Ind. Eng. Chem.</u> 39 (1947): 1536–1543.

[71]   Duke, F. R.; and Hass, T. W. The Homogeneous Base-Catalyzed Decomposition of Hydrogen Peroxide. <u>J. Phys. Chem.</u> 65 (1961): 304–306.

[72]   Baumgartner, H. J.; Hood, G. C.; Monger, J. M.; Roberts, R. M.; and Sanborn, C. E. Decomposition of Concentrated Hydrogen Peroxide on Silver I. Low Temperature Reaction and Kinetics. <u>J. Catal.</u> 2 (1963): 405–414.

[73]   Lide, D. R. (ed.), <u>CRC Handbook of Chemistry and Physics (CD-ROM Version).</u> 90th ed. Boca Raton, FL: CRC Press/Taylor and Francis, 2010.

[74]   Lofton, C.; and Sigmund, W. Mechanisms Controlling Crystal Habits of Gold and Silver Colloids. <u>Adv. Funct. Mater.</u> 15 (2005): 1197–1208.

[75]   Xia, Y.; Xiong, Y.; Lim, B.; and Skrabalak, S. E. Shape-Controlled Synthesis of Metal Nanocrystals: Simple Chemistry Meets Complex Physics? <u>Angew. Chem., Int. Ed.</u> 48 (2009): 60–103.

[76]   Xiong, Y.; and Xia, Y. Shape-Controlled Synthesis of Metal Nanostructures: The Case of Palladium. <u>Adv. Mater.</u> 19 (2007): 3385–3391.

[77]   Wiley, B.; Herricks, T.; Sun, Y.; and Xia, Y. Polyol Synthesis of Silver Nanoparticles: Use of Chloride and Oxygen to Promote the Formation of Single-Crystal, Truncated Cubes and Tetrahedron. <u>Nano Lett.</u> 4 (2004): 1733–1739.

[78]   Wiley, B. J.; Chen, Y.; McLellan, J. M.; Xiong, Y.; Li, Z. Y.; Ginger, D.; and Xia, Y. Synthesis and Optical Properties of Silver Nanobars and Nanorice. <u>Nano Lett.</u> 7 (2007): 1032–1036.

[79]   Xiong, Y.; Chen, J.; Wiley, B.; Xia, Y.; Aloni, S.; and Yin, Y. Understanding the Role of Oxidative Etching in the Polyol Synthesis of Pd Nanoparticles with Uniform Shape and Size. <u>J. Am. Chem. Soc.</u> 127 (2005): 7332–7333.

[80]   Wiley, B.; Sun, Y.; and Xia, Y. Synthesis of Silver Nanostructures with
        Controlled Shapes and Properties. <u>Acc. Chem. Res.</u> 40 (2007): 1067–
        1076.

[81]   Filippo, E.; Serra, A.; and Manno, D. Poly(vinyl alcohol) Capped Silver
        Nanoparticles as Localized Surface Plasmon Resonance-Based
        Hydrogen Peroxide Sensor. <u>Sensor. Actuat. B-Chem.</u> 138 (2009): 625–
        630.

[82]   Vasileva, P.; Donkova, B.; Karadjova, I.; and Dushkin, C. Synthesis of
        Starch-Stabilized Silver Nanoparticles and Their Application as a
        Surface Plasmon Resonance-Based Sensor of Hydrogen Peroxide.
        <u>Colloids Surf. A Physicochem. Eng. Aspects</u> 382 (2011): 203–210.

[83]   Germain, V.; Li, J.; Ingert, D.; Wang, Z. L.; and Pileni, M. P. Stacking Faults
        in Formation of Silver Nanodisks. <u>J. Phys. Chem. B</u> 107 (2003): 8717–
        8720.

[84]   Rocha, T. C. R.; and Zanchet, D. Structural Defects and Their Role in the
        Growth of Ag Triangular Nanoplates. <u>J. Phys. Chem. C</u> 111 (2007):
        6989–6993.

[85]   Cobley, C. M.; Rycenga, M.; Zhou, F.; Li, Z. Y.; and Xia, Y. Etching and
        Growth: An Intertwined Pathway to Silver Nanocrystals with Exotic
        Shape. <u>Angew. Chem., Int. Ed.</u> 48 (2009): 4824–4827.

[86]   Wiley, B.; Sun, Y.; Mayers, B.; and Xia, Y. Shape-Controlled Synthesis of
        Metal Nanostructures: The Case of Silver. <u>Chem-Eur J.</u> 11 (2005): 454–
        463.

[87]   Henglein, A. Physicochemical Properties of Small Metal Particles in
        Solution: "Microelectrode" Reactions, Chemisorption, Composite Metal
        Particles, and the Atom-to-Metal Transition. <u>J. Phys. Chem.</u> 97 (1993):
        5457–5471.

[88]   Solomon, S. D.; Bahadory, M.; Jeyarajasingam, A. V.; Rutkowsky, S. A.; and
        Boritz, C. Synthesis and Study of Silver Nanoparticles. <u>J. Chem. Educ.</u>
        84 (2007): 322–325.

[89]   Wongravee, K.; Parnklang, T.; Pienpinijtham, P.; Lertvachirapaiboon, C.; Ozaki, Y.; Thammacharoen, C.; and Ekgasit, S. Chemometric Analysis of Spectroscopic Data on Shape Evolution of Silver Nanoparticles induced by Hydrogen Peroxide. Phys. Chem. Chem. Phys. 15 (2013): 4183–4189.

[90]   Wiley, B.; Xiong, Y.; Li, Z. Y.; Yin, Y.; and Xia, Y. Right Bipyramids of Silver: A New Shape Derived from Single Twinned Seeds. Nano Lett. 6 (2006): 765–768.

[91]   Sosa, I. O.; Noguez, C.; and Barrera, R. G. Optical Properties of Metal Nanoparticles with Arbitrary Shape. J. Phys. Chem. B 107 (2003): 6269–6275.

[92]   González, A. L.; Noguez, C.; Ortiz, G. P.; and Rodríguez-Gattorno, G. Optical Absorbance of Colloidal Suspensions of Silver Polyhedral Nanoparticles. J. Phys. Chem. B 109 (2005): 17512–17517.

[93]   Noguez, C. Optical Properties of Isolated and Supported Metal Nanoparticles. Opt. Mater. 27 (2005): 1204–1211.

[94]   Noguez, C. Surface Plasmons on Metal Nanoparticles: The Influence of Shape and Physical Environment. J. Phys. Chem. C 111 (2007): 3806–3819.

[95]   Xu, H.; and Rice, B. W. *In-vivo* Fluorescence Imaging with a Multivariate Curve Resolution Spectral Unmixing Technique. J. Biomed. Opt. 14 (2009): 064011.

[96]   Bazilevskaya, E.; Archibald, D. D.; and Martinez, C. E. Rate constants and mechanisms for the crystallization of Al nano-goethite under environmentally relevant conditions. Geochim. Cosmochim. Acta. 88 (2012): 167–182.

[97]   Esteban, M.; Ariño, C.; Diaz Cruz, J. M.; Diaz-Cruz, M. S.; and Tauler, R. Multivariate Curve Resolution with Alternating Least Squares Optimization: A Soft-Modeling Approach to Metal Complexation Studies by Voltammetric Techniques. Trends Anal. Chem. 19 (2000): 49–61.

[98]   Li, B.; Zhang, J.; Hu, Y.; Liang, Y.; and Ozaki, Y. Exploring Time-
         Dependent Structural Changes during the Cold Crystallization Process
         of Isotactic Polystyrene by Infrared Spectroscopy and Multivariate
         Curve Resolution. Appl. Spectrosc. 60 (2006): 155–161.

[99]   Navea, S.; Tauler, R.; and de Juan, A. Monitoring and Modeling of Protein
         Processes using Mass Spectrometry, Circular Dichroism, and
         Multivariate Curve Resolution Methods. Anal. Chem. 15 (2006): 4768–
         4778.

[100]   Hemmateenejad, B.; and Nezhad, M. R. H. Investigating the Shape Evolution
         Mechanism of CdSe Quantum Dots by Chemometrics Analysis of
         Spectrophotometric Data. J. Phys. Chem. C 112 (2008): 18321–18324.

[101]   Muto, S.; Yoshida, T.; and Tatsumi, K. Diagnostic Nano-Analysis of
         Materials Properties by Multivariate Curve Resolution Applied to
         Spectrum Images by S/TEM-EELS. Materials Transactions 50 (2009):
         964–969.

[102]   Kanet Wongravee. Development of Multivariate Curve Resolution Program
         Based On Self-Modeling Techniques For Chemical Applications.
         Master's Thesis, Department of Chemistry, Faculty of Science,
         Chulalongkorn University, 2005.

[103]   Jaumot, J.; Gargallo, R.; de Juan, A.; and Tauler, R. A user friendly interface
         for MCR-ALS: a new tool for Multivariate Curve Resolution in
         MATLAB. Chemom. Intell. Lab. Syst. 76 (2005): 101–110.

[104]   Van Hyning, D. L.; and Zukoski, C. F. Formation Mechanisms and
         Aggregation Behavior of Borohydride Reduced Silver Particles.
         Langmuir 14 (1998): 7034–7046.

[105]   Zeng, J.; Roberts, S.; and Xia, Y. Nanocrystal-Based Time-Temperature
         Indicators. Chem-Eur J. 16 (2010): 12559–12563.

[106]   Zhang, Q.; Li, W.; Moran, C.; Zeng, J.; Chen, J.; Wen, Long-Ping; and Xia,
         Y. Seed-Mediated Synthesis of Ag Nanocubes with Controllable Edge
         Lengths in the Range of 30–200 nm and Comparison of Their Optical
         Properties. J. Am. Chem. Soc. 132 (2010): 11372–11378.

[107] Rycenga, M.; Cobley, C. M.; Zeng, J.; Li, W.; Moran, C. H.;, Zhang, Q.; Qin, D.; and Xia, Y. Controlling the Synthesis and Assembly of Silver Nanostructures for Plasmonic Applications. Chem. Rev. 111 (2011): 3669–3712.

[108] Pal, T.; Sau, T. K.; and Jana, N. R. Reversible Formation and Dissolution of Silver Nanoparticles in Aqueous Surfactant Media. Langmuir 13 (1997): 1481–1485.

[109] Ekgasit, S.; Pattayakorn, N.; Tongsakul, D.; Thammacharoen, C.; and Kongyou, T. A Novel ATR FT-IR Microspectroscopy Technique for Surface Contamination Analysis without Interference of the Substrate. Anal. Sci. 23 (2007): 863–868.

[110] Tongsakul, D.; Wongravee, K.; Thammacharoen, C.; and Ekgasit, S. Enhancement of the Reduction Efficiency of Soluble Starch for Platinum Nanoparticles Synthesis. Carbohydr. Res. 357 (2012): 90–97.

[111] Pienpinijtham, P.; Thammacharoen, C.; and Ekgasit, S. Green Synthesis of Size Controllable and Uniform Gold Nanospheres Using Alkaline Degradation Intermediates of Soluble Starch as Reducing Agent and Stabilizer. Macromol. Res. 20 (2012): 1281–1288.

[112] Kizil, R.; Irudayaraj, J.; and Seetharaman, K. Characterization of Irradiated Starches by Using FT-Raman and FT-IR Spectroscopy. J. Agric. Food Chem. 50 (2002): 3912–3918.

[113] He, J.; Kunitake, T.; and Nakao, A. Facile *In Situ* Synthesis of Noble Metal Nanoparticles in Porous Cellulose Fibers. Chem. Mater. 15 (2003): 4401–4406.

[114] Zhang, Q.; Cobley, C. M.; Zeng, J.; Wen, L. P.; Chen, J.; and Xia Y. Dissolving Ag from Au–Ag Alloy Nanoboxes with H_2O_2: A Method for Both Tailoring the Optical Properties and Measuring the H_2O_2 Concentration. J. Phys. Chem. C 114 (2010): 6396–6400.

[115] Wasim, M.; and Brereton, R. G. Determination of the Number of Significant Components in Liquid Chromatography Nuclear Magnetic Resonance Spectroscopy. Chemom. Intell. Lab. Syst. 72 (2004): 133–151.

[116] Yin, Y; and Alivisatos, A. P. Colloidal Nanocrystal Synthesis and the Organic-Inorganic Interface. Nature 437 (2005): 664–670.

[117] Zhang, J.; Huang, F.; and Lin, Z. Progress of Nanocrystalline Growth Kinetics Based on Oriented Attachment. Nanoscale 2 (2010): 18–34.

[118] Liang, H.; Zhao, H.; Rossouw, D.; Wang, W.; Xu, H.; Botton, G. A.; and Ma, D. Silver Nanorice Structures: Oriented Attachment-Dominated Growth, High Environmental Sensitivity, and Real-Space Visualization of Multipolar Resonances. Chem. Mater. 24 (2012): 2339–2346.

[119] Liu, Z.; Zhou, H.; Lim, Y. S.; Song, J. H.; Piao, L.; and Kim, S. H. Synthesis of Silver Nanoplates by Two-Dimensional Oriented Attachment. Langmuir 28 (2012): 9244–9249.

[120] Bohren, C. F.; and Huffman, D. R. Absorption and Scattering of Light by Small Particles. New York: John Wiley & Sons, Inc., 1983.

[121] Rakic, A. D.; Djurisic, A. B.; Elazar, J. M.; and Majewski, M. L. Optical Properties of Metallic Films for Vertical-Cavity Optoelectronic Device. Applied Optics 37 (1998): 5271–5283.

[122] Xiong, Y.; Washio, I.; Chen, J.; Sadilek, M.; and Xia, Y. Trimetric Clusters of Silver in Aqueous $AgNO_3$ Solutions and Their Role as Nuclei in Forming Triangular Nanoplates of Silver. Angew. Chem., Int. Ed. 46 (2007): 4917–4921.

VITAE

Date of Birth: April 2, 1983   **Birth Place:**   Chonburi, Thailand

Address: 121/36, Sukhumwit Road, Sriracha, Chonburi 20110, Thailand

Educations:

Ph.D. / Chemistry   2012   Chulalongkorn University/Thailand

B.Sc. (1st Class Hons.) / Chemistry   2004   Chulalongkorn University/Thailand

Research Publications:

1. **Parnklang, T.**; Lertvachirapaiboon, C.; Pienpinijtham, P.; Wongravee, K.; Thammacharoen, C.; and Ekgasit, S. H_2O_2-Triggered Shape Transformation of Silver Nanospheres to Nanoprisms with Controllable Longitudinal LSPR Wavelengths. <u>RSC Adv.</u> 2013, Accepted Manuscript (DOI: 10.1039/C3RA41486H).

2. Wongravee, K.; **Parnklang, T.**; Pienpinijtham, P.; Lertvachirapaiboon, C.; Ozaki, Y.; Thammacharoen, C.; and Ekgasit, S. Chemometric Analysis of Spectroscopic Data on Shape Evolution of Silver Nanoparticles induced by Hydrogen Peroxide. <u>Phys. Chem. Chem. Phys.</u> 15 (2013): 4183–4189.

Scholarships and Awards:

2003–2011   : *Development and Promotion of Science and Technology Talents Project (Royal Government of Thailand Scholarship)* supported by The Institute for the Promotion of Teaching Science and Technology

April 2012   : *Gold Medals* from the invention entitled "Pansements pour plaies "bleu argent"" at The Grand Prix of the 40th International Exhibition of Inventions of Geneva, Switzerland